Timing Jitter In Long-haul WDM Return-To-Zero Systems

vorgelegt von
Diplom-Ingenieur
André Richter
aus Berlin

von der Fakultät IV Elektrotechnik und Informatik
der Technischen Universität Berlin
zur Erlangung des akademischen Grades

Doktor der Ingenieurwissenschaften
- Dr.-Ing. -

genehmigte Dissertation

Promotionsausschuss:

Vorsitzender:	Prof. Dr.-Ing. Noll
1. Gutachter:	Prof. Dr.-Ing. Petermann
2. Gutachter:	Prof. Dr.-Ing. Voges (Universität Dortmund)

Tag der wissenschaftlichen Aussprache: 19. Februar 2002

Berlin 2002
D 83

Table of Contents

Chapter 1

Introduction

1.1 Long-haul fiber-optic transmission

Long distance fiber-optic telecommunication systems carry digital information over terrestrial distances ranging from 3,000 km to 5,000 km and transoceanic distances ranging from 5,500 km to 12,000 km. During the last 10 years these systems have evolved significantly. In 1988, only 2% of long distance traffic was carried by submarine cables. At this time, most traffic was transmitted via satellite connections. However, in 2000, 80% of the traffic was carried over optical fiber links already. The popularity of optical fiber systems is mainly due to the potentially huge bandwidth, and thus channel capacity, which was made available due to the dramatic progress in the development of optical fibers and amplifiers, transmitters and receivers during the past 10 years.

In the late 1980s, electro-optic repeaters and fiber optics were introduced to long-haul transmission systems, replacing the copper cables. This first generation of transoceanic fiber systems carried 280 Mbit/s in a single channel at 1300 nm. With the invention of single-frequency laser diodes at around 1550 nm, and Erbium-doped fiber amplifiers (EDFA), Gigabit-per-second systems could be built in the 1990s. The first transoceanic projects employing these technologies since 1996 were the TAT-12/13 project [148] and the TPC-5 network [14], initially, both operated at 5 Gbit/s.

Today's long-haul transmission systems represent the fourth generation utilizing multiple carrier wavelengths, which had lead to an explosion of channel capacity. At the same time, deregulation of telecommunication mar-

kets and global success of the internet has driven the demand for higher and higher system capacity. In 1998, existing systems were upgraded to carry up to four coarsely spaced wavelengths. Today, new dense wavelength-division multiplexing (DWDM) systems are under construction that will soon deliver up to 1 Tbit/s of data per fiber over transoceanic distances.

Conventionally, non return-to-zero (NRZ) modulation format has been used in long-haul transmission systems [148], [14]. These systems are based on the fact that fiber dispersion and nonlinearities are detrimental effects. NRZ is used advantageously as it provides minimum optical bandwidth, and minimum optical peak power per bit interval for given average power.

However, with increased bitrates it has been shown that RZ modulation formats offer certain advantages over NRZ, as they tend to be more robust against distortions [23]. For instance, RZ modulation is more tolerant to non-optimized dispersion maps than NRZ schemes [113]. This can be explained by the fact that optimum balancing between fiber nonlinearities and dispersion is dependent on the pulse shape. A RZ modulated signal stream consists of a sequence of similar pulse shapes, whereas a NRZ modulated stream does not. The dispersion tolerance of a signal stream can be derived from the superposition of the dispersion tolerance of the individual pulse shapes [113]. In fact, for the majority of cases, the best results of WDM transmission experiments regarding the distance-bitrate product have been achieved using RZ modulation formats in both terrestrial and transoceanic systems (see Table 1-1).

When designing high capacity systems, it becomes increasingly important to carefully model system performance before performing laboratory experiments and field trials, as these experiments are costly and time consuming. The huge design space can only be limited by analytical approximations and computer modeling using powerful simulation tools.

This work focuses on the characteristics of RZ pulse propagation over modern long-haul fiber-optic transmission systems. Major distortions of those systems arise from pulse timing jitter, which are introduced by various sources along the propagation path. It is the subject of this work to numerically investigate the timing jitter in long-haul WDM RZ systems. The following section presents a short overview of each chapter in this thesis.

.

Table 1-1. *Results of recent long-haul experiments.*

	Capacity [Gbit/s]	Distance [km]	Notes	Reference
OFC 1998	320 (64x5)	7,200	CRZ (chirped return-to-zero), LCF (large core fiber)	[19]
ECOC 1998	500 (25x10)	9,288	nonlinearity supporting RZ, HODM (higher order dispersion management)	[123]
OFC 1999	640 (64x10)	7,200	CRZ, LCF, FEC (forward error correction)	[20]
	1,020 (51x20)	1,012	DMS (dispersion-managed soliton), mainly SMF	[63]
ECOC 1999	1,100 (55x20)	3,020	DMS, HODM, C/L-band	[47]
	1,000 (100x10)	6,200	chirped RZ, HODM using LCF, FEC	[149]
OFC 2000	1,800 (180x10)	7,000	CRZ, HODM, FEC	[32]
ECOC 2000	1,120 (56x20)	6,200	CRZ, HODM, FEC	[24]
	2,110 (211x10)	7,221	chirped RZ, HODM using LCF, Raman, C/L-band, FEC	[147]
OFC 2001	2,400 (120x20)	6,200	CRZ, HODM using LCF, enhanced FEC	[25]

1.2 Chapter overview

In Chapter 2, recent trends in long-haul terrestrial and submarine systems design are presented. Drastic changes have been reported over the last decade driven by the dramatic increase of capacity demand. Design considerations of transmitter, optical fiber link and receiver for typical long-haul transmission systems are discussed.

Chapter 3 presents different RZ modulation formats, which are considered to be of great potential for long-haul propagation. The time and frequency dynamics of the most favorite modulation formats, namely dispersion-managed soliton (DMS) and chirped return-to-zero (CRZ), are discussed in detail. Lately, convergence between DMS- and CRZ-based transmission systems has been subject to discussion. Overall results of these discussions are briefly summarized.

Chapter 4 starts with a brief overview of the main distortions that occur in long-haul WDM transmission. This is followed by a detailed discussion pre-

senting the two main sources of pulse timing jitter in long-haul fiber-optic transmission systems. These jitter sources are, noise generated from optical inline amplifiers, and interchannel cross-phase modulation (XPM). Firstly, an overview of common techniques used to estimate ASE-noise induced timing jitter (ANTJ) is presented. A recently reported approach for ANTJ estimation is presented, which is derived for arbitrary pulse shapes. This approach takes into account the impact of pulse chirping on accumulated timing jitter [60]. Secondly, an overview of common approximations to estimate collision-induced timing jitter (CITJ) due to interchannel XPM is given. The limitations of all these techniques are discussed in detail. Then, a new approach for estimating CITJ is presented, which can be applied to RZ pulses of arbitrary shapes, undergoing an arbitrary number of collisions with pulses propagating in an arbitrary number of channels.

In Chapter 5, results from typical WDM system simulations are presented. Timing jitter values estimated from the two semi-analytical techniques discussed in Chapter 4 are used to explore the dependence of ANTJ and CITJ on several system design parameters such as dispersion map, amplifier positioning, channel spacing, and initial pulse positioning.

In Chapter 6, commonly used methods for estimating system performance are presented. The focus is on techniques used for calculating the bit error rate (BER), and their applicability in software modeling of long-haul transmission systems. The translation of pulse timing jitter to BER is outlined, and a simple method of considering its impact is presented. This method is then applied to different WDM system simulations.

Finally, Chapter 7 gives a summary of the work.

Chapter 2

Long-haul WDM transmission systems

2.1 Overview

This chapter provides general information on components and subsystems of a typical long-haul WDM transmission system. The scope of this chapter is not to provide detailed knowledge, but rather to provide information, which characterizes the most important system components, and is of need in the following chapters. This chapter should help to motivate, why system parameter values are set the way they are, and why certain system impairments are not regarded in this work.

Firstly, the externally modulated transmitter, which performs intensity modulation (IM) of the optical carrier wave is briefly introduced. A WDM transmitter consists typically of one externally modulated transmitter per channel, which are connected together via filters and couplers to finally feed the optical WDM signal into the optical fiber.

Secondly, fiber propagation is investigated in more detail. The major fiber propagation effects are presented, which are the linear effects of fiber attenuation and chromatic dispersion, and the nonlinear effects due to the Kerr nonlinearity. Polarization-dependent propagation effects are not considered, as this is outside the scope of this work. Afterwards, the generalized nonlinear Schrödinger equation (GNLS) is introduced, which describes the propagation of optical waves over the nonlinear, dispersive fiber. A numerical

method for solving the GNLS is introduced, and important scale distances are listed.

Thirdly, the Erbium-doped fiber amplifier (EDFAs) is introduced as the major mean for amplification in long-haul WDM transmission systems. EDFAs are employed as booster amplifiers at the WDM transmitter, as inline amplifiers compensating periodically for the fiber attenuation, and as pre-amplifiers in front of the optical receivers to limit the impact of the receiver noise. After providing some information about the amplification process in Erbium-doped fibers, the characteristics of amplifier gain and noise generation are discussed. Finally, design aspects of EDFAs are briefly presented.

This chapter will be finished with a section on optical direct detection (DD) receivers. Their architecture is briefly presented, and major noise contributions are listed.

2.2 Transmitter

For modern WDM transmission systems employing channel bitrates of 10 Gbit/s and higher, external modulation is commonly applied for intensity and phase modulation of the optical carrier. Externally modulated transmitters provide a high wavelength-stability, a small amount of distortions, a high extinction ratio, and a defined frequency chirp characteristic. Frequency chirp denotes the time-dependence of the phase of the optical signal, and can be controlled to counteract for fiber propagation degradations due to chromatic dispersion and self-phase modulation[1] [49].

Externally modulated transmitters are based on the principle that a wavelength-stable laser is operated to emit a continuous wave (CW) into an external modulator device, which is controlled by an electrical voltage carrying the data and pulse shape information. Two types of modulators are commonly used, namely Mach-Zehnder modulators (MZM) and electro-absorption modulators (EAM) [72]. MZMs provide usually a better defined transfer

1. See Chapter 2, p. 9 and Chapter 2, p. 12 for details.

characteristic. They can be designed to have zero frequency chirp, or a chirp, which can be controlled by the electrical drive voltage. EAMs are more easy to integrate, however, provide an intrinsic chirp already, which is proportional to the gradient of the emitted optical power.

Figure 2-1 shows the schematic of the transmitter for the case that a MZM is used for external modulation. The electrical drive signal is created by feeding the output of the bit source into a pulse generator.

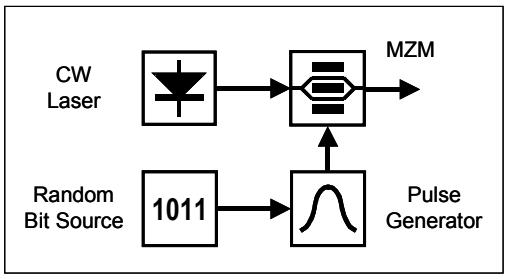

Figure 2-1. *Schematic of externally modulated laser.*

The Mach-Zehnder modulator is based on the interference principle. That is, the electric field of the incident optical signal is split to propagate over two branches, over which the field experiences different amounts of phase change due to the electro-optic effect. Then, the optical signals of the two branches are recombined again, which results in an interference pattern that is directly related to the phase difference between the two branches. The amount of phase change over each branch is controlled by electrical voltages. The transfer function of the MZM can be written as [155]

$$\frac{E_{out}(t)}{E_{in}(t)} = \cos[\Delta\Phi(t)]\exp[-j\alpha\tan(\Delta\Phi_{bias})\Delta\Phi(t)] \qquad (2\text{-}1)$$

where $E_{in,\,out}(t)$ is the electric field at the input and the output of the modulator, respectively.

$\Delta\Phi(t)$ is the phase difference of the electric fields in the two branches of the MZM,

$\Delta\Phi_{bias}$ is the bias point of operation,

α is the so-called α-factor defining the chirping behavior of the MZM. It is given as [96]

$$\alpha = 2I\left[\frac{d}{dt}\varphi(t)/\frac{d}{dt}I(t)\right] \tag{2-2}$$

where $d\varphi/dt$ is the phase change at the output of the MZM,
dI/dt is the intensity change at the output of the MZM,
with $I = |E|^2/c\mu$, c speed of light in a vacuum, μ permeability.

When operating the MZM with $\Delta\Phi_{bias} = \pi/4$, ideal intensity modulation is achieved for $\alpha = 0$.

2.3 Fiber propagation

With the invention of low-loss optical fibers [78], the telecommunications industry discovered the optical fiber as medium for efficient information transfer between locations being several kilometers apart from each other. Today, a multitude of different fiber types are commercially available, which offer different signal propagation characteristics. For details, see [44].

In the following section, the main characteristics of signal propagation in a single-mode optical fiber are presented. Afterwards, an expression for the propagation of the slowly varying amplitude of the electric field in single-mode optical fibers is derived, and a numerical algorithm for solving it is briefly presented.

2.3.1 Attenuation

The first investigated effect is the fiber attenuation, which describes the fact that optical signal power decreases exponentially when propagated in optical fibers. This can be written in logarithmic units as follows

$$P_{dBm}(0) - P_{dBm}(L) = \alpha_{dB/km}L. \tag{2-3}$$

where $\alpha_{dB/km}$ is the fiber attenuation in [dB/km],

L is the fiber distance in [km],

$P_{dBm}(0)$ is the optical power at the input of the fiber in [dBm],

$P_{dBm}(L)$ is the optical power after the fiber distance L in [dBm].

The fiber attenuation is mainly caused by absorption and scattering processes. Absorption arises from impurities and atomic effects in the fiber glass. Scattering is mainly due to intrinsic refractive index variations of fiber glass with distance (Rayleigh scattering) and imperfections of the cylindrical symmetry of the fiber. The usable bandwidth ranges from approximately 800 nm (increased Rayleigh scattering) to approximately 1600 nm (infrared absorption due to vibrational transitions). In this region, attenuation is mainly governed by Rayleigh scattering, which scales with λ^{-4}. It can reach values below 0.2 dB/km at around 1550 nm. For details on contributions to fiber attenuation in optical fibers, see [54], [91].

Sometimes it is useful to work with attenuation values in linear units. The following equation defines the relation between linear and logarithmic expression

$$\alpha = \frac{\ln(10)}{10}\alpha_{dB/km} \approx 0.23026\alpha_{dB/km}. \tag{2-4}$$

2.3.2 Group-velocity dispersion (GVD)

The second considered propagation effect is the group-velocity dispersion (GVD). It arises from the frequency dependence of the modal propagation constant $\beta(\omega)$ of an optical wave traveling in silica fiber. Expanding $\beta(\omega)$ in a Taylor series around an arbitrary frequency ω_0 gives [4]

$$\begin{aligned}\beta(\omega) &= n(\omega)\frac{\omega}{c} \\ &= \beta_0 + \beta_1(\omega-\omega_0) + \frac{1}{2}\beta_2(\omega-\omega_0)^2 + \frac{1}{6}\beta_3(\omega-\omega_0)^3\end{aligned} \tag{2-5}$$

where $n(\omega)$ is the effective refractive index of the optical fiber,

c is the speed of light in a vacuum,

$$\beta_k = \frac{\partial^k}{\partial \omega^k}\beta(\omega)\bigg|_{\omega=\omega_0} \qquad k = 0, 1, 2, 3\,.$$

The coefficients $\beta_k, k = 0, 1, 2, 3$ have the following physical interpretation:

- β_0 accounts for a frequency independent phase offset during propagation.
- β_1 denotes the inverse of the group velocity v_g, which determines the speed of energy propagated through the fiber.
- β_2 describes the frequency dependence of the inverse of v_g. It defines the broadening of a pulse due to the fact that its Fourier components propagate with different group velocities[1]. This effect is known as chromatic dispersion or group velocity dispersion (GVD).
- β_3 is known as the slope of the GVD, or second order GVD. It accounts for the frequency dependence of the GVD and, therefore, for different broadening properties of signals or signal portions propagating at different frequencies. It is important to be considered for frequency regions where β_2 is close to zero, or for wideband transmission problems[2].

It is commonly of more interest to determine the dependence of the inverse of the group velocity on wavelength rather than on frequency. This dependence is described by the dispersion parameter D and its slope with respect to wavelength, S. The following relationships hold

$$\begin{aligned} D &= \frac{d}{d\lambda}\frac{1}{v_g} = -\frac{2\pi c}{\lambda^2}\beta_2 \qquad & S &= \frac{dD}{d\lambda} = \frac{(2\pi c)^2}{\lambda^3}\left(\frac{1}{\lambda}\beta_3 + \frac{1}{\pi c}\beta_2\right) \\ \beta_2 &= \frac{d}{d\omega}\frac{1}{v_g} = -\frac{\lambda^2}{2\pi c}D \qquad & \beta_3 &= \frac{d\beta_2}{d\omega} = \frac{\lambda^3}{(2\pi c)^2}(\lambda S + 2D) \end{aligned} \quad . \tag{2-6}$$

D is typically measured in units ps/nm-km. It determines the broadening ΔT for a pulse of bandwidth $\Delta\lambda$ after propagating over a distance z, or equivalently, the time offset of two pulses after a distance z, which are separated in the spectral domain by $\Delta\lambda$.

1. Equivalently, it defines the different propagation speeds of pulses in frequency separated channels, and hence, is basis for interchannel pulse collisions in WDM transmission systems.
2. Such as wideband dispersion compensation in DWDM systems, or estimation of crosstalk due to stimulated Raman scattering.

$$\Delta T \approx \Delta\lambda \frac{dT}{d\lambda} = \Delta\lambda z \frac{d}{d\lambda}\left\{\frac{1}{v_g}\right\} = \Delta\lambda z D \tag{2-7}$$

GVD consists mainly of two additive parts, namely intrinsic material dispersion (frequency dependence of the refractive index) and waveguide dispersion (frequency dependence of the guiding properties of the fiber). Depending on the manufacturing process and the radial structure of the fiber, fiber types with various dispersion profiles can be designed. For further information see [92].

2.3.3 Kerr effect

The third propagation effect, which is presented here, is the Kerr effect. It denotes the phenomenon that actually the refractive index of optical fibers $n(\omega, t)$ is slightly dependent on the electric field intensity I of the optical signal passing through the fiber.

$$n(\omega, t) = n_0(\omega) + n_2 I(t) \tag{2-8}$$

where n_0 is the linear refractive index,

n_2 is the nonlinear refractive index.

Note that the electric field intensity varies in time with the transmitted pulse stream. It induces intensity dependent modulation of the refractive index, and hence modulation of the phase of the transmitted pulse stream. This effect is called the Kerr effect.

Compared to other nonlinear media, n_2 is very small[1]. However, optical fiber is quite an effective nonlinear medium as field intensities of several milliWatts are focused in the small fiber core of 50 – 75 μm^2 over interaction lengths of tens to hundreds of kilometers. A comparison with bulk media using typical parameters shows that the enhancement factor of nonlinear processes in single mode fibers is 10^7 – 10^9 [5]. Thus, effects from nonlinear interaction between signal pulses might accumulate during transmission and become of system limiting importance.

1. Typically of the order of 10^{-20} [m^2/W].

Kerr nonlinearity accounts for diverse intensity dependent propagation effects. The most important ones are:

- Self-Phase Modulation (SPM)
- Cross-Phase Modulation (XPM)
- Four Wave Mixing (FWM).

The phenomenological aspects of these effects are discussed in the following sections.

2.3.3.1 Self- and cross-phase modulation

When sending pulse streams with intensity $I(t)$ and initial phase ϕ_0 at different carrier frequencies into the fiber, phase modulation of the signal in channel m depends on the local power distribution of all channels as follows

$$\phi_m(t,z) - \phi_{0,m} = \frac{2\pi}{\lambda}\left[n_{0,m}z + n_2 z \cdot I_m(t) + n_2 z \cdot 2\sum_{k \neq m} I_k(t)\right] \tag{2-9}$$

where $\phi_m(t,z)$ is the phase modulation of channel m,

$\phi_{0,m}$ is the initial phase of channel m,

$n_{0,m}$ is the linear refractive index of channel m,

n_2 is the nonlinear refractive index,

k is an index denoting the neighboring channels of channel m.

The first term in the square brackets on the right-hand side of Eq. (2-9) corresponds to the accumulated linear phase shift due to transmission.

The second term corresponds to the accumulated nonlinear phase shift due to self-phase modulation (SPM) in channel m. The SPM-induced phase shift is proportional to the local electric field intensity. It induces frequency chirp and spectral broadening, so pulses behave differently in the presence of GVD. As shown in Chapter 3, p. 32, linear chirp from GVD and nonlinear chirp from SPM combine and can be used advantageously for pulse propagation.

The third term describes phase modulation induced by intensity fluctuations in neighboring channels k. This effect is called cross-phase modulation (XPM). XPM introduces additional nonlinear pulse chirp, which interacts

with the local dispersion as well. Note that it occurs only over distances, where pulses overlap. So, XPM effects reduce in general with increased dispersion as pulses at different frequencies propagate faster through each other[1]. More details on the impact of XPM in WDM transmission is outlined in Chapter 4, p. 59.

2.3.3.2 Four-wave mixing

When propagating waves at different carrier frequencies over the fiber, parametric interactions might induce the generation of intermodulation products at new frequencies. This nonlinear effect is called four-wave mixing (FWM). It occurs, for instance, when two photons at frequencies ω_1 and ω_2 are absorbed to produce two other photons at frequencies ω_3 and ω_4 such that

$$\omega_1 + \omega_2 = \omega_3 + \omega_4 . \tag{2-10}$$

It could also be understood as mixing of three waves producing a fourth one

$$\begin{aligned} E_{klm} &= E_k E_l E_m^* \\ &= |E_k||E_l||E_m| \exp\{j(\omega_k + \omega_l - \omega_m)t\} \exp\{-j[\beta(\omega_k) + \beta(\omega_l) - \beta(\omega_m)]z\} \end{aligned} \tag{2-11}$$

where $E_i = E(\omega_i) = |E_i| \exp\{j[\omega_i t - \beta(\omega_i)z]\}$ is the electric field of the wave propagating at ω_i,

$\beta(\omega_i)$ is the modal propagation constant at ω_i,

$\omega_{klm} = \omega_k + \omega_l - \omega_m$ is the carrier frequency of the wave E_{klm}.

The energy of the wave E_{klm} is given as superposition of mixing products of any three waves for which $\omega_{klm} = \omega_k + \omega_l - \omega_m$ holds[2]. Note that the propagation constant is frequency dependent. So, efficient interactions only occur if contributions to E_{klm} given at different times add up over distance. This so-called phase matching condition can be written as

$$\Delta\beta \to 0 \qquad \text{with } \Delta\beta(\omega) = \beta(\omega_k) + \beta(\omega_l) - \beta(\omega_m) - \beta(\omega_{klm}) \tag{2-12}$$

1. The distance over which pulses propagating in different channels overlap is the so-called collision length. See also Eq. (2-24).
2. Additionally to FWM between three waves at different frequencies, degenerate FWM occurs when two of the waves coincide at the same frequency ($\omega_k = \omega_l$).

where $\Delta\beta$ describes the phase mismatch between the intermodulating electric fields. With Eq. (2-5) substituted into Eq. (2-12), $\Delta\beta$ is given with respect to fiber dispersion as

$$\begin{aligned}\Delta\beta(\omega) &= (\omega_k - \omega_m)(\omega_l - \omega_m)\left\{-\beta_2 + \beta_3\left(\frac{\omega_l + \omega_k}{2} - \omega\right)\right\} \\ &= 2\pi c\left(\frac{\omega_k - \omega_m}{\omega_0}\right)\left(\frac{\omega_l - \omega_m}{\omega_0}\right)\left\{D + \left(\frac{\omega_l + \omega_k}{2\omega_0} - \frac{\omega}{\omega_0}\right)\left(\frac{2\pi c}{\omega_0}S + 2D\right)\right\}\end{aligned} \tag{2-13}$$

where ω_0 is the reference frequency of D and S.[1]

The power of the newly created wave is proportional to the power of the three interacting waves[2]

$$\left|E_{klm}(z)\right|^2 \sim \eta\left(\left|E_k(z)\right|\left|E_l(z)\right|\left|E_m(z)\right|\right)^2 \tag{2-14}$$

where η is the so-called FWM efficiency taking into account the phase mismatch $\Delta\beta$. It is given by [84]

$$\eta = \frac{\alpha^2}{\alpha^2 + \Delta\beta}\left\{1 + \frac{4\exp(-\alpha z)\sin(\Delta\beta z/2)^2}{[1 - \exp(-\alpha z)]^2}\right\} \tag{2-15}$$

where α is the fiber attenuation, z is the propagation distance.

Figure 2-2 shows the FWM efficiency η versus channel spacing for different dispersion values after one span of 50 km length. Only the degenerate case $\omega_k = \omega_l$ is considered[3].

1. The second relation in Eq. (2-13) has been derived using Eq. (2-6).
2. Assuming no pump depletion due to FWM, which is satisfied, if power transfer between waves is small.
3. The reference frequency is set to $\omega_0 = \omega_l$.

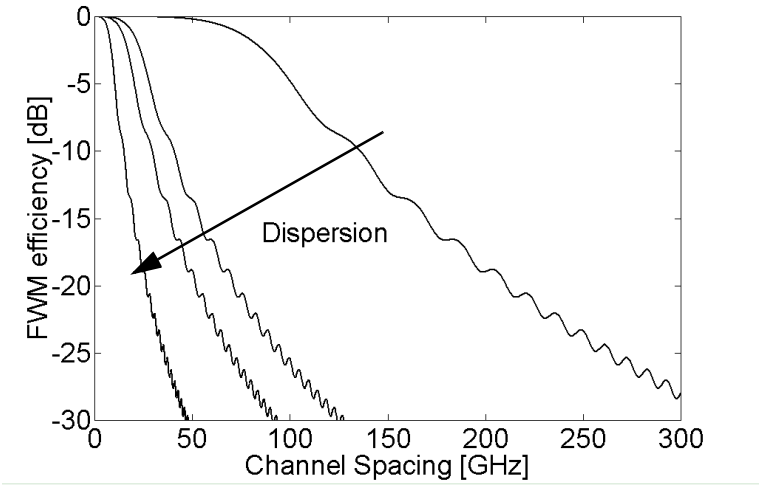

Figure 2-2. *FWM efficiency* η *versus channel spacing for different dispersion values after propagation over one span of 50 km (S = 0.1 ps/nm^2-km,* α *= 0.25 dB/km); from left to right: D = 17.0, 4.4, 2.3, 0.1 ps/nm-km.*

Increasing local dispersion results in an increased walk-off of Fourier components and thus, phase mismatch after shorter propagation distances, which results in steeper decrease of FWM efficiency with channel spacing. Figure 2-2 shows that for $|D| \geq$ 2.3 ps/nm-km, FWM efficiency is decreased below -25 dB for 100 GHz channel spacing and still below -20 dB for 75 GHz channel spacing.

2.3.4 Propagation over nonlinear and dispersive fiber

2.3.4.1 Generalized nonlinear Schrödinger equation

In this section, the propagation equation for the slowly varying amplitude of the electric field in optical single-mode fibers is presented. Details of the derivation can be found in [103], [6].

Starting from Maxwell's equations, the optical field evolution in a dielectric medium can be described by the wave equation as follows

$$\Delta\vec{E} - \frac{1}{c^2}\frac{\partial^2}{\partial t^2}\vec{E} - \mu_0\frac{\partial^2}{\partial t^2}\vec{P} = 0 \qquad (2\text{-}16)$$

where $\vec{E}$ is the electric field vector,

$\vec{P} = \vec{P}_L + \vec{P}_{NL}$ is the electric polarization vector,

c is the speed of light in a vacuum, μ_0 is the vacuum permeability.

For silica-based optical fibers, $\vec{P}$ can be described via $\vec{E}$ as follows

$$\vec{P} \approx \frac{\mu_0}{c^2}\{\chi^{(1)}\vec{E} + \chi^{(3)}\vec{E}^3\} \tag{2-17}$$

where $\chi^{(1)}$ is the first order susceptibility, defining the linear evolution behavior,

$\chi^{(3)}$ is the third order susceptibility, responsible for the nonlinear propagation characteristics. It is related to the ratio of nonlinear and linear refractive index via $n_2/n_0 = \frac{3}{8}\mathrm{Re}\{\chi^{(3)}\}$.

Assuming that the fundamental mode of the electric field is linearly polarized in the x or y direction[1], its value can be approximately described using the method of separation of variables by

$$E(x, y, z, t) = Re\{F(x, y)A(z, t)\exp[j(\omega_0 t - \beta_0 z)]\} \tag{2-18}$$

where $F(x, y)$ is the transversal field distribution,

$A(z, t)$ is the complex field envelope[2] describing electric field evolution in the propagation direction z and time t, with $|A|^2$ corresponding to the optical power.

For single-mode fiber, $F(x, y)$ represents the fundamental fiber mode HE_{11}, approximately given by a Gaussian distribution over the fiber radius. $A(z, t)$ is determined as a solution of the generalized nonlinear Schrödinger equation (GNLS), which is given by

$$j\left[\frac{\partial}{\partial z}A + \beta_1\frac{\partial}{\partial t}A\right] + \frac{1}{2}\beta_2\frac{\partial^2}{\partial t^2}A - j\frac{1}{6}\beta_3\frac{\partial^3}{\partial t^3}A + j\frac{\alpha}{2}A = \gamma|A|^2 A \tag{2-19}$$

1. With z being the propagation direction.
2. Also known as slowly varying amplitude.

where α is the fiber attenuation in linear units,

$\beta_i, i = 1, 2, 3$ are defined in Eq. (2-5),

$\gamma = (n_2\omega_0)/(cA_{eff})$ is the nonlinear coefficient,

with n_2 nonlinear refractive index, ω_0 reference frequency,

c speed of light in a vacuum, A_{eff} effective core area of the fiber given by $A_{eff} = \dfrac{\left(\int_{-\infty}^{\infty}\int_{-\infty}^{\infty}|F(x,y)|^2 dxdy\right)^2}{\int_{-\infty}^{\infty}\int_{-\infty}^{\infty}|F(x,y)|^4 dxdy} \approx \pi\rho_m^2$.

The approximate term for A_{eff} is derived assuming a Gaussian distribution of $F(x,y)$,

$$F(x,y) = \exp\left[-\frac{(x^2+y^2)}{\rho_m^2}\right] \tag{2-20}$$

where ρ_m is the effective mode radius.

Eq. (2-19) describes the evolution of the slowly varying field amplitude over a nonlinear, dispersive fiber. It describes the most important propagation effects for pulses of widths larger than 5 ps. It can, however, be extended to include higher order GVD and other nonlinear effects[1], which might be of importance for ultra-short pulse propagation or wide bandwidth applications. Polarization dependent propagation effects are not considered here, as they will not be regarded throughout this work.

2.3.4.2 Split-step Fourier method

The generalized nonlinear Schrödinger equation (GNLS), as given in Eq. (2-19), can not be solved analytically for the general case of arbitrarily shaped pulses launched into the fiber. However, powerful numerical procedures have been developed over the years to solve it. Among them, the split-step Fourier method has proven to be the most robust technique [83]. It is based on the principle that linear and nonlinear propagation effects can be considered separately from each other over short fiber distances Δz.

1. Such as stimulated Raman scattering and pulse self-steepening.

$$A(z+\Delta z) = \{A(z)\exp(\Delta z\hat{N})\}\exp(\Delta z\hat{D}) \tag{2-21}$$

where $\hat{D} = j\frac{1}{2}\beta_2\frac{\partial^2}{\partial t^2} + \frac{1}{6}\beta_3\frac{\partial^3}{\partial t^3} - \frac{\alpha}{2}$ is the linear operator, accounting for fiber dispersion and attenuation.

$\hat{N} = -j\gamma|A|^2$ is the nonlinear operator accounting for the Kerr nonlinearity.

If Δz, the so-called split-step size, becomes too large the condition for separable calculation of $\hat{D}$ and $\hat{N}$ breaks, and the algorithm delivers wrong results. So careful determination of the optimum split-step size is of importance in order to use minimal computational effort for a given accuracy. Typically, Δz is adaptively adjusted, for instance, according to

$$\Delta z = \min\{\Delta\phi_{NL}L_{NL}, \Delta z_{max}\} \tag{2-22}$$

where $\Delta\phi_{NL}$ is the maximum acceptable phase shift due to the nonlinear operator[1],

$L_{NL} = 1/\gamma|A|^2$ is the nonlinear scale length[2],

Δz_{max} is a maximum split-step size, which is set to limit spurious FWM tones [22].

The linear operator $\hat{D}$ is most efficiently solved in the spectral domain, while the nonlinear operator $\hat{N}$ is more favorably solved in the time domain. Assuming a discrete signal description in the time and frequency domain, the Fast Fourier Transform (FFT) is used for converting between both [129]. As the speed of the FFT is proportional to $N\log_2 N$, where N is the number of signal samples in the time or frequency domain, careful determination of the simulation bandwidth and the time window is important for minimizing computational effort given specific accuracy constraints[3].

1. Typically in the range of 0.05 – 0.2rad.
2. See also Eq. (2-26).
3. See also Chapter 4, p. 61 for a numerical effort estimation.

2.3.4.3 Characteristic scale distances

Certain characteristics of pulse evolution over optical fiber are governed by several scale lengths, which are described in the following:

- The effective length L_{eff} is defined as the equivalent fiber interaction length with respect to constant power [29]. Thus, it is derived from the exponential power decay in optical fiber as follows

$$L_{eff} = \int_0^z \exp(-\alpha z_1) dz_1 = \frac{1 - \exp(-\alpha z)}{\alpha}. \tag{2-23}$$

  It is important when, for instance, rescaling the pulse evolution to account for attenuation and periodic amplification.

- The walk-off length L_w is defined as the distance it takes for one pulse traveling at frequency ω_1 to overtake another pulse traveling at frequency ω_2

$$L_w = \frac{T_0}{|\beta_1(\omega_2) - \beta_1(\omega_1)|} \approx \frac{T_0}{|D\Delta\lambda_{12}|} \tag{2-24}$$

  where $\beta_1 = v_g^{-1}$, and T_0 is the pulse duration (half-width 1/e-intensity)[1].

  It is also called the collision length L_c, as it accounts for the distance where two pulses at different frequencies collide during propagation. Thus, it is of importance when determining XPM effects.

- The dispersion length L_D defines the distance over which a chirp-free Gaussian pulse broadens by a factor of $\sqrt{2}$ due to GVD

$$L_D = \frac{T_0^2}{|\beta_2|}. \tag{2-25}$$

  It denotes the distance where dispersive effects become important.

- The nonlinear length L_{NL} defines the distance over which the phase change due to the Kerr nonlinearity becomes one rad

$$L_{NL} = \frac{1}{\gamma |A|^2}. \tag{2-26}$$

1. Measured as the width from the pulse center to the point where the intensity level dropped to 1/e of the maximum intensity level.

It denotes the distance where nonlinear effects become important.

The ratio between L_D and L_{NL} describes the dominating behavior for pulse evolution over optical fiber. Of special interest is the region $L_D \sim L_{NL}$, where cancellation of nonlinear and dispersive effects can be observed for certain parameter settings (see Chapter 3, p. 32).

Note also that solutions of the GNLS, as given in Eq. (2-19), remain invariant from certain scale transformations. When dividing, for instance, both sides of Eq. (2-19) by an arbitrary scaling factor p, a set of new parameters can be defined, for which the solution of Eq. (2-19) remains invariant. These new parameters are related to the old ones by [106]

$$\tilde{t} = p \cdot t \qquad \tilde{z} = p \cdot z \qquad \tilde{\beta}_2 = p \cdot \beta_2 \qquad \tilde{\gamma} = \frac{1}{p} \cdot \gamma \qquad \tilde{\alpha} = \frac{1}{p} \cdot \alpha . \qquad (2\text{-}27)$$

So when, for instance, the bitrate is increased from 10 Gbit/s to 40 Gbit/s, and thus, the pulse width is reduced to one fourth, p is calculated to 0.25. With the decreased pulse width, sensitive scale lengths for dispersion and nonlinearity reduce also to one fourth. This implies that dispersion map lengths as well as average and local dispersion values need to be adjusted, and nonlinear propagation effects become four times more important than for 10 Gbit/s. The latter could eventually be compensated by reducing the pulse power. This however, would also reduce the signal-to-noise ratio[1], and thus, give rise to other distortions.

2.4 Erbium-doped fiber amplifier (EDFA)

With the invention of Erbium-doped fiber amplifiers (EDFA) in the late 1980s [109], the development of fiber-optic communication systems accelerated rapidly. Electro-optic repeaters could be replaced by the more robust, flexible and cost-efficient EDFAs, allowing all-optic links over transoceanic distances in the mid 1990s.

1. See Chapter 2, p. 24, and Chapter 6, p. 100 for details.

Apart from the optical fiber itself, the EDFA is the most important component of long-haul transmission in determining system performance. Depending on the application, different design criteria are of importance. The main amplifier characteristics are large gain, low noise figure, gain flatness, and large output power. In the following, the main concepts of EDFAs are presented. A detailed discussion on the design of EDFAs is given in [35], [15].

2.4.1 Erbium ions in glass hosts

When doping silica fiber with Er^{3+} ions (or with ions of other rare-earth elements), the fiber can be operated as an active laser medium when pumped. Figure 2-3 shows the energy diagram of Erbium ions in glass hosts.

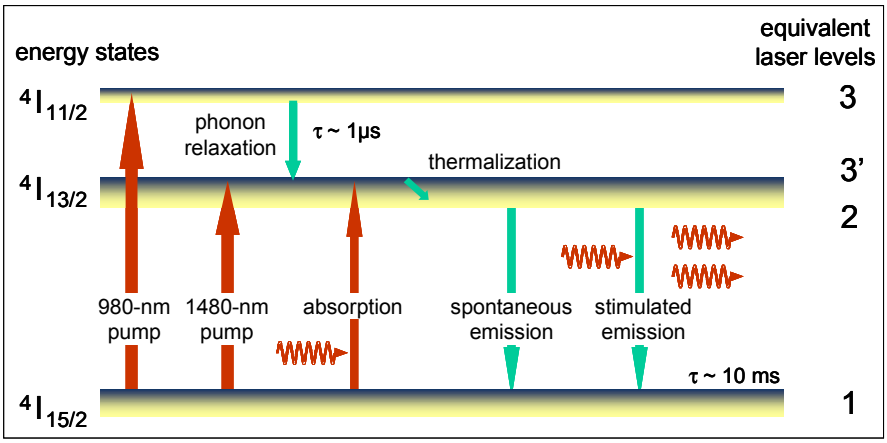

Figure 2-3. *Energy diagram of Er^{3+}-ions in glass hosts.*

For 980 nm pumping, carriers are absorbed from ground level to the third laser level. Because of phonon relaxation within one microsecond, they transit down to the second level almost immediately[1], where they distribute due to thermalization processes. For 1480 nm pumping, carriers are absorbed from the ground level directly to the second laser level, where they again distribute due to thermalization processes. Thus, it is a reasonable assumption to model gain and noise behavior in EDFAs using only a two-level laser medium.

1. Compared to the lifetime at the second stage ($\tau \sim 10$ ms).

From the upper level, carriers can transit down to the ground level via spontaneous emission, or via stimulated emission for the case where signal energy is co-launched in the wavelength range 1530 nm to 1600 nm. Stimulated emission provides signal gain; spontaneous emission is detected as noise.

2.4.2 Amplifier gain

The gain in EDFAs is strongly dependent on the carrier inversion, i.e, the amount of carrier population in the upper state compared to the total number of carriers. It is determined by the pumping scheme, and co-dopants such as germanium and alumina. The wavelength dependence of local gain can be written as [36]

$$g(\lambda) = [N_2\sigma_e(\lambda) - N_1\sigma_a(\lambda)]\Gamma(\lambda) \tag{2-28}$$

where N_2, N_1 denote the carrier populations of the upper and lower states, respectively,

$\sigma_a(\lambda)$, $\sigma_e(\lambda)$ denote the absorption and emission cross-sections, respectively,

$\Gamma(\lambda)$ is the overlap factor, i.e., the area of overlap between Erbium ions and the optical signal mode in the fiber.

Note that the population inversion shows a strong local dependence, so gain may differ over the length of the doped fiber. Figure 2-4 shows the wavelength dependence of the gain for the two pump wavelength regions and the signal bandwidth around 1550 nm.

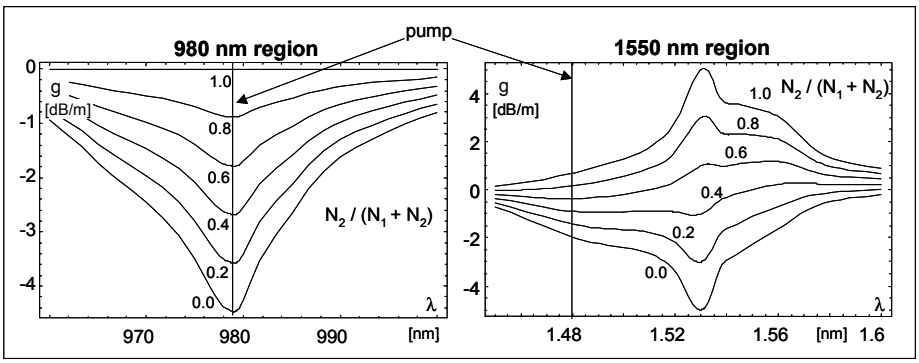

Figure 2-4. *Exemplary gain/loss profile for various values of population inversion.*

The left diagram shows the gain as a function of population inversion at 980 nm (pump) and neighborhood. Perfect inversion is possible as the emission cross-section is zero at 980 nm. This results in small noise generation for 980 nm pumped EDFA configurations. The right diagram in Figure 2-4 shows gain as a function of population inversion at 1480 nm (pump) and around 1550 nm (signal band). For the depicted inversion profile, the transparency point (g = 0 dB/m) for 1480 nm pumping is at about 75% population inversion. So, perfect inversion is not possible, which results in increased noise generation. The figure depicts the strong wavelength dependence of the gain, which results from the wavelength dependence of population inversion. For large inversion levels, a high gain peak is observed at 1530 nm; for lower inversion levels, the gain decreases at 1530 nm, but increases at 1550 nm, eventually delivering a flat gain over several nanometers.

Ignoring noise for the moment, the average signal power dependence on doped fiber length is given by

$$\frac{dP}{dz} = g(\lambda, P)P\,. \tag{2-29}$$

For small signal power values, the total amplifier gain is usually independent of the incoming power. If the power launched into the doped fiber is increased over a certain level, stimulated recombination starts to affect carrier population inversion. Every photon created by stimulated emission transfers one ion from the upper state to the lower state. This results in gain reduction until absorption of pump power and stimulated plus spontaneous

recombinations are balancing each other. This effect is known as gain saturation.

The saturation characteristic of EDFAs is very complex, as it is locally dependent. Assuming a homogenous power distribution along the EDFA, the gain is given by [80]

$$\left.\frac{P}{P_{sat}}\right|_{input} = 0.7213\frac{G_0 - 2}{G - 1} \cdot \ln\left(\frac{G_0}{G}\right) \tag{2-30}$$

where G is the gain of the amplifier, given by $G = P(L_{Amp})/P(0)$ with L_{Amp} the length of doped fiber,

G_0 is the small-signal or linear gain of the amplifier,

$P_{sat}|_{input}$ is the saturation power, defined as input power for which $G/G_0 = 0.5$.

For long-haul applications, inline amplifiers are typically operated in saturation to avoid gain fluctuations due to incoming power fluctuations.

2.4.3 Amplified spontaneous emission (ASE) noise

Spontaneous transitions of photons from the upper state to the ground state add up along the doped fiber and stimulate other transitions, which results in self-amplification. This effect is called amplified spontaneous emission (ASE). ASE-noise evolution propagates bidirectionally along the fiber. So it builds up in the forward *and* backward directions. The amount of ASE-noise created at each end of the doped fiber depends on the local population inversion.

The ASE-noise can be approximated by a white, Gaussian random process. The power spectral density (PSD) of the ASE-noise in the x-polarization at the amplifier output can be written as

$$S_{ASE,x} = \frac{P_{ASE,x}}{\Delta f} = n_{sp}(G - 1)hf \tag{2-31}$$

where $n_{sp} = \frac{N_2\sigma_e(\lambda)}{N_2\sigma_e(\lambda) - N_1\sigma_a(\lambda)}$ is the spontaneous emission factor[1],

G is total amplifier gain, hf is the photon energy,

$P_{ASE,x}$ is the ASE-noise power measured over a bandwidth Δf.

As the ASE-noise power is proportional to the gain and n_{sp}, it can be limited when operating the EDFA at high population inversion.

The noise performance of amplifiers is usually characterized by the noise figure NF. It is defined as degradation of the electrical signal-to-noise ratio (SNR) due to the amplifier, measured with an ideal photodetector[2] [34].

$$\begin{aligned} NF &= \frac{SNR_{in}}{SNR_{out}} \\ &\approx 2n_{sp}\frac{(G-1)}{G} + \frac{1}{G} \end{aligned} \tag{2-32}$$

The approximation relation in Eq. (2-32) is derived for low noise amplifiers, neglecting ASE-ASE beat noise [93]. The NF is typically given in dB. For amplifiers with large gain, the minimum NF is 3 dB, as $n_{sp} \geq 1.0$. With Eq. (2-31) and Eq. (2-32), the noise power spectral density can be written as function of NF and gain; both values are measurable from the outside of the amplifier

$$S_{ASE,x} = \frac{P_{ASE,x}}{\Delta f} = \frac{1}{2}(NF \cdot G - 1)hf. \tag{2-33}$$

2.4.4 Design aspects

Figure 2-5 shows a typical architecture for a two-stage EDFA. The first stage operates as a low-noise pre-amplifier, preferably pumped at 980 nm to ensure small NF[3]. The second stage operates as a power amplifier, preferably pumped at 1480 nm as this concept provides higher power conversion efficiency. Generally, the doped fiber can be pumped from either side. The isolator between both stages prevents saturation of the first stage due to

1. Also called population inversion factor, with $n_{sp} \geq 1.0$, typically 1.4 – 2.0.
2. No thermal noise, no dark current, 100% quantum efficiency.
3. According to the chain rule, the NF of an amplifier cascade is mainly determined by the NF of the first amplifier in the chain [31].

backward propagating ASE-noise from the second stage. Also, the filters are used to suppress ASE-noise outside the signal bandwidth and perform gain equalization.

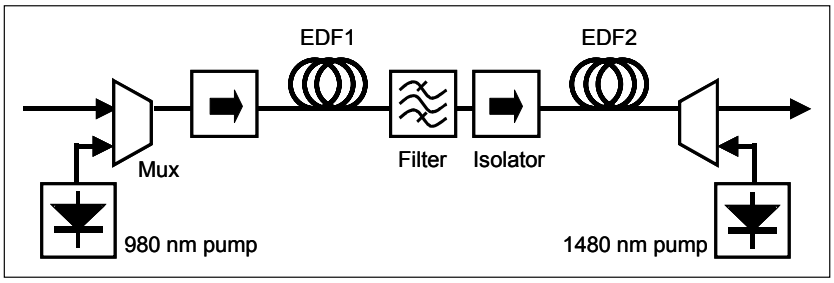

Figure 2-5. *Two-stage EDFA design.*

EDFA designs as depicted in Figure 2-5 have a NF of 4 – 6 dB and can provide flat gain over a bandwidth of about 30 nm. More sophisticated designs achieving gain flatness over 70 nm can be developed using more than two amplifier stages or other co-dopings [158]. For transoceanic fiber links, the requirements for gain flatness and low NF are very high as up to 200 EDFAs are cascaded over such links. Also, robustness is of great importance, as each failure may cause severe repair costs. Thus, redundant pump configurations are usually used for inline EDFAs in submarine links.

2.5 Receiver

As considered in this work, the receiver performs the optical-electrical signal conversion, eventually some signal enhancement features, and finally the decision about the transmitted bit stream.

2.5.1 Architecture

Figure 2-6 shows the schematic of an intensity-modulation direct detection (IM-DD) receiver. The received electric field of the optical signal is first

pre-amplified by an EDFA with low noise figure[1] in order to reduce noise limiting effects of the following electrical components. It is followed by an optical filter, which rejects noise outside the signal bandwidth. In case of WDM transmission, the filter serves as demultiplexer as well, rejecting the signal power of the neighboring WDM channels. Then, the optical power is detected by a photodiode. It is translated into an electrical current resembling the same time-characteristics as the incident optical power. The photodiode is assumed to inhabit an electrical load resistor and an electrical amplifier. It is typically followed by an electrical filter, which performs pulse shaping and further noise reduction. Finally, the signal is passed to the decision circuitry consisting of a clock recovery and a decision gate.

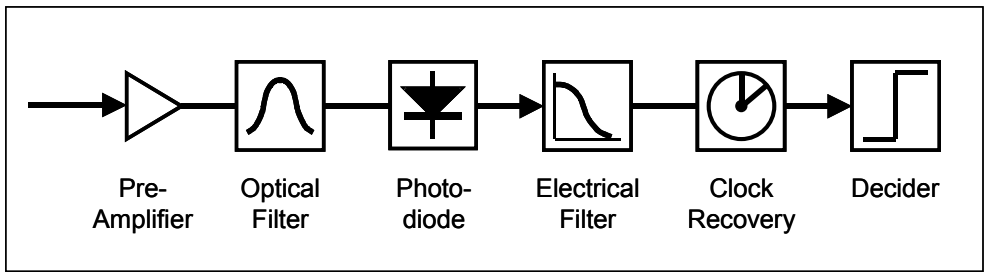

Figure 2-6. *Schematic IM-DD receiver.*

Typically two types of photodiodes are used for detection, namely PIN and Avalanche photodiodes. Details on both can be found in [55]. Throughout this work, the IM-DD receiver is assumed to be based on a PIN photodiode. The received current after the PIN photodiode can be written as

$$i(t) = \frac{\eta q}{hf} \cdot \left| E_s(t) \right|^2 + N(t) \tag{2-34}$$

where η is the quantum efficiency of the photodiode,

q is the electron charge, hf is the photon energy,

$\left| E_s(t) \right|$ is the electric field amplitude of the optical signal wave,

$N(t)$ is an additive noise term summarizing sources of noise.

1. See Chapter 2, p. 24 for details on design issues.

Ignoring the noise term $N(t)$ first, note that the electrical power is proportionally related to the square of the optical signal power. The proportion constant is the so-called responsivity of the photodiode, defined as

$$R = \frac{\eta q}{hf} \qquad 0 \le R \le 1\,. \tag{2-35}$$

2.5.2 Noise contributions

In the following section, the noise term $N(t)$ in Eq. (2-34) is investigated in more detail. Details to receiver noise can be found in [7].

Shot noise

Shot noise arises from the fact that electric current is not continuous, but consists of discrete electrons, generated randomly by the photodiode in response to the incident optical power. Shot noise is actually described by a Poisson process [39], but is well approximated in practice by a Gaussian probability density function (PDF). Its variance is given by

$$\sigma_{sh}^2 = 2q(RP_o + I_d)\cdot \Delta f_{el} \tag{2-36}$$

where P_o is the incident optical power,

I_d is the dark current of the photodiode,

Δf_{el} is the effective noise bandwidth of the receiver considering the limited bandwidth of photodiode and the electrical filter.

Thermal noise

Thermal noise arises from random motions of electrons for non-zero temperatures [56]. The induced random current fluctuations can be well approximated by a Gaussian PDF with variance

$$\sigma_{th}^2 = (4k_B T/R_l)NF\cdot \Delta f_{el} \tag{2-37}$$

where k_B is the Boltzmann's constant, T is the absolute temperature,

R_l is the electrical load resistor of the photodiode,

NF is the noise figure of the electrical amplifier in the photodiode.

ASE-noise beating

Additionally to electrical receiver noise sources, optical noise that falls in the same frequency band as the optical signal passes the optical filter and is detected by the photodiode. There are mainly two beating terms of interest, namely beating of ASE-noise with itself and with the electric field of the optical signal. In a first approximation, these beating terms can also be assumed to follow a Gaussian distribution. More details are given in Chapter 6, p. 108. The variance of the signal-ASE beat noise is given by [86]

$$\sigma^2_{signal,ASE} = 2R^2 P_S \int_0^\infty [S_{ASE}(f-f_s) + S_{ASE}(f+f_s)] H_T^2(f)\,df \tag{2-38}$$

where P_S is the detected electrical signal power level without considering ASE-noise,

S_{ASE} is the power spectral density of the ASE-noise,

H_T is the transfer function of the electrical filter.

The variance of the ASE-ASE beat noise can be written as

$$\sigma^2_{ASE,ASE} = 4R^2 \int_0^\infty [S_{ASE}(f) \otimes S_{ASE}(f)] H_T^2(f)\,df \tag{2-39}$$

where $\otimes$ denotes convolution.

Chapter 3

Characteristics of RZ pulse propagation

3.1 Overview

The first long-haul transmission systems employing RZ modulation schemes were demonstrated for classical soliton systems in 1988 using Raman amplification over 4,000 km [115], and in 1990 using EDFAs over 10,000 km [116]. The experimental proof was given: RZ modulation can be utilized for long-haul transmission. However, further development of system concepts and components needed to be achieved before the first massive WDM (7x10 Gbit/s) transmission experiment over transoceanic distances could be performed [120] in 1996. Again, solitons were used, which were at that time the most promising RZ modulation scheme to cover long-haul distances.

However, the first commercial long-haul system utilizing a RZ modulation scheme was built in 1998, using chirped RZ (CRZ) pulses. Contrary to classical soliton systems, which are based on balancing linear and nonlinear effects, the CRZ modulation scheme allows propagation in a quasi-linear regime. It turned out that dense WDM systems using classical solitons were difficult to design. This was mainly due to nonlinear channel interactions raised by the fact that the local dispersion values need to stay small. In the mid 1990s, the first dispersion-managed soliton (DMS) systems were experimentally demonstrated. The results showed that the soliton concept could be applied for dispersion-managed fiber links, which in effect triggered inten-

sive research on how to design dense WDM systems using the newly found DMS format.

This chapter presents, firstly, the evolution of dispersion-managed solitons from classical soliton theory. DMS characteristics are analyzed. Then, the CRZ modulation format is discussed. Finally, an outlook on the latest trends of RZ modulation formats is presented.

3.2 Dispersion-managed soliton (DMS)

3.2.1 Evolution from classical soliton theory

3.2.1.1 Lossless fiber

Considering the general pulse evolution equation presented in Chapter 2, p. 15, linear propagation effects and fiber attenuation are balancing the intensity dependence of the refractive index[1]. Ignoring fiber loss ($\alpha = 0$), and introducing normalized units, the GNLS in Eq. (2-19) can be written as

$$j\frac{\partial}{\partial Z}q = \frac{L_D}{L_{NL}}|q|^2 q - \frac{1}{2}\mathrm{sgn}(\beta_2)\frac{\partial^2}{\partial T^2}q \tag{3-1}$$

where q is the normalized field amplitude given by $q = A/\sqrt{P_0}$, with P_0 peak power at fiber input,

Z is the normalized transmission distance given by $Z = z/L_D$,

L_D is the dispersion length, and L_{NL} is nonlinear length[2],

T is the normalized, retarded time given by $T = (t - \beta_1 z)/\sqrt{L_D|\beta_2|}$

$\mathrm{sgn}(x)$ is the signum function.

Using the inverse scattering method [69], Eq. (3-1) can be solved analytically for a launched pulse shape, which satisfies Eq. (3-1) at any distance point.

1. Introduced as Kerr nonlinearity, see Chapter 2, p. 11.
2. See Chapter 2, p. 19 for definitions.

Among others, so-called soliton solutions exist in the anomalous dispersion regime ($\beta_2 < 0$), which satisfy the criteria

$$N_s = \sqrt{\frac{L_D}{L_{NL}}} = 1, 2, \ldots . \tag{3-2}$$

Solitons in optical fiber transmissions where first predicted theoretically in 1973 [64] and observed experimentally in 1980 [114]. Since then, they have been widely used to investigate and explain fundamental pulse propagation characteristics. Of special interest is the fundamental soliton solution, as its pulse shape is not altered during propagation. It is given for the case $L_D = L_{NL}$ to

$$q(Z, T) = \operatorname{sech}(T)\exp(jZ/2) . \tag{3-3}$$

Only the phase of the fundamental soliton is undergoing a circular change with period $z = \pi L_D$. Other, higher order soliton solutions of interest for fiber-optic communications are those of the same initial pulse shape as the fundamental one

$$q(0, T) = N_s \operatorname{sech}(T) \qquad N_s = 2, 3, \ldots . \tag{3-4}$$

Note that these solutions change their shape periodically during propagation, recovering their original shape after soliton periods of length

$$L_S = (\pi/2)L_D . \tag{3-5}$$

At the fiber input, the peak power and width of the soliton are related by Eq. (3-2). Using definitions for dispersion and nonlinear lengths, as introduced in Chapter 2, p. 19, one gets

$$P_0 = N_s^2 \frac{|\beta_2|}{\gamma T_0^2} \approx N_s^2 3.107 \frac{|\beta_2|}{\gamma T_F^2} \qquad N_s = 1, 2, \ldots \tag{3-6}$$

where T_0 is the pulse duration (half-width 1/e-intensity)[1]

T_F is the FWHM pulse duration[2].

1. Measured as the width from the pulse center to the point where the intensity level dropped to 1/e of the maximum intensity level.
2. Measured as the width between the two points left and right of the pulse center where the intensity level dropped to 1/2 of the maximum intensity level (FWHM: full-width half maximum).

Figure 3-1 shows the pulse shape evolution of the fundamental soliton in comparison with a Gaussian pulse. For both pulses, the peak power is 7.53 mW and the FWHM duration is 20 ps. It is nice to see how the fundamental soliton retains its shape, while the Gaussian pulse shape is changing rapidly as it tries to balance linear (pulse-spreading) and nonlinear (pulse-compressing) forces.

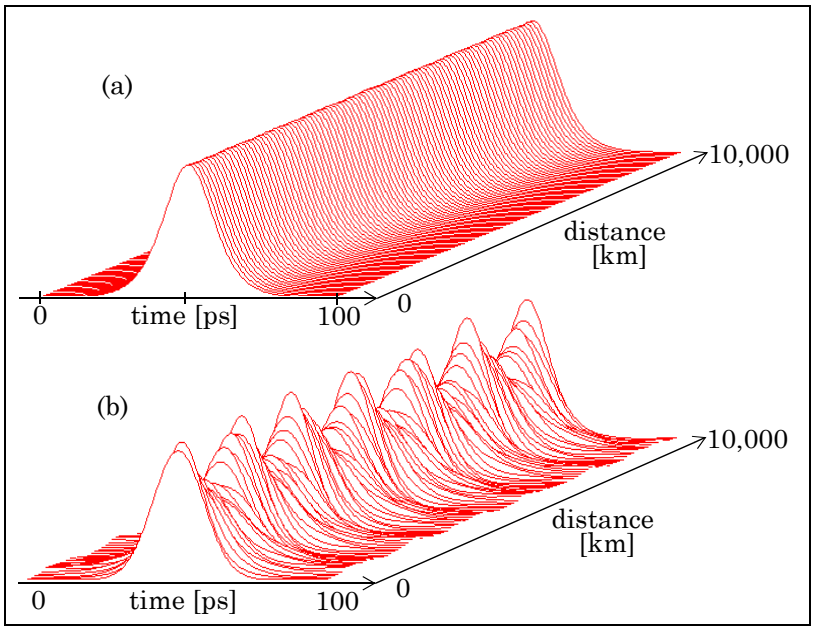

Figure 3-1. *Evolution of sech (a) and Gaussian (b) shaped pulses of equal FWHM duration, (no fiber attenuation).*

Soliton interactions

Solitons are derived from Eq. (3-1) as a stable solution for single pulse propagation. Thus, interactions with pulses in neighboring bit intervals might lead to perturbations, which could destroy the soliton characteristics if their impact becomes too large. Considering two solitons of equal amplitude and phase, they will periodically collapse at distance intervals of [52]

$$L_{Collapse} = \frac{\pi}{2} L_D \exp(\Delta T_0) \tag{3-7}$$

where L_D is the dispersion length,

$\Delta T_0 = T_b/(2T_0)$ is the initial pulse separation, with T_b bit duration, and T_0 pulse duration (half-width 1/e-intensity),

For transmission distances shorter than $L_{Collapse}$, no collapsing occurs. This constraint would limit initial pulse separation to $\Delta T_0 \geq 10$ assuming trans-oceanic transmission over up to 15,000 km. However, it can be reduced to about $\Delta T_0 \geq 4$ for the case where the two collapsing solitons are not of equal amplitude and phase (which is the case in most realistic scenarios) due to, for example, random initial chirp from the transmitter, second order GVD, and random amplifier noise [71], [85]. More information on intrachannel interactions is given in Chapter 4, p. 47.

3.2.1.2 Periodically amplified fiber link

A remarkable property of solitons is their robustness against small perturbations. Therefore, it is generally not of great importance to launch an exactly sech-shaped pulse with a correct power-width ratio. *Small* deviations will be repaired by re-shaping, yielding a pulse with slightly different pulse width, and energy shedding during propagation [68]. In the very late 1980s, the first soliton experiments with EDFAs were performed [115], [125]. They showed that solitons can propagate stably in lossy fiber with periodically spaced amplifiers as long as the amplifier spacing is small enough.

Considering the normalized GNLS as given in Eq. (3-1) for the anomalous dispersion regime and $L_D = L_{NL}$, fiber loss and amplification can be incorporated as follows

$$-j\frac{\partial}{\partial Z}q + \frac{1}{2}\frac{\partial^2}{\partial T^2}q + |q|^2 q = j\left(\frac{\alpha}{2}L_D - GL_D\right)q \tag{3-8}$$

where $\frac{\alpha}{2}L_D$ is the fiber loss, over one dispersion length L_D,

$G(Z)$ is the amplifier gain as function of distance.

The term on the right-hand side of Eq. (3-8) represents a perturbation to the classical soliton propagation. The application of perturbation theory [70] showed that as long as its influence is small, the soliton will still develop.

However, this requirement limits lumped amplifier spacings to about 20 – 30 km or the usage of distributed amplification[1].

Average soliton regime

In the early 1990s, it was discovered that solitons exist even for propagation scenarios where $\Gamma \gg 1$. The pulse evolution does not follow the classical soliton regime as pulses periodically changed their time and frequency shape. However, the same stable pulse shape could be observed in average over several amplifier spans. As the pulse evolution is governed by the average soliton energy, these pulses are called guiding center or average solitons.

In this propagation regime, restrictions to amplifier spacing L_A can be relaxed. Stable pulse propagation occurs as long as $L_A < L_D$ [65]. However, the initial peak power needs to be increased with respect to Eq. (3-6) to accommodate for the fiber loss. The so-called pre-emphasis [97] assures that average pulse energy over one amplifier span equals the energy of the fundamental soliton. This is, assuming that there will be no changes of pulse width during propagation over one span, this means that

$$\tilde{P}_0 = \frac{L_A}{L_{eff}} P_0 \tag{3-9}$$

where L_{eff} is the effective fiber length, as defined in Eq. (2-23),

L_A is the amplifier spacing.

When the pulse power is not enhanced, the average soliton is not able to focus itself. The resonance effect between the average soliton length L_S and amplifier span length L_A is also of interest. With Eq. (3-5), resonances occur at [67]

$$L_A = 4\pi k L_D \qquad k = 1, 2, 3, \ldots . \tag{3-10}$$

An average soliton emitted under such conditions, will emit dispersive waves that adjust amplitude and width until it eventually matches another soliton solution, for which Eq. (3-10) does not hold.

1. The usage of Raman amplification was considered in the very early investigations of solitons and has become of great interest during the past two years again.

3.2.1.3 Dispersion-managed, lossy fiber link

Very soon after the average soliton was found for periodically amplified systems, it was discovered that periodic dispersion compensation has a similar effect on pulse dynamics [66]. In 1995, it has been shown that the so-called dispersion-managed soliton (DMS) can be propagated over long-haul distances [146]. Inside each dispersion map, the characteristics of DMS evolution is governed by local dispersion values. Thus, the DMS changes its width inside each dispersion map in a periodic fashion; it 'breathes' with the local dispersion. Average dispersion and fiber nonlinearity support the pulse behavior on average over several dispersion maps[1]. Stable propagation of DMSs is possible, as long as the dispersion map length is small compared to L_{NL} [137].

The advantage of DMS systems compared to classical soliton systems is the possibility to utilize larger local dispersion values, which results in increased robustness against disturbing fiber nonlinear effects (such as FWM, XPM) and timing jitter due to ASE-noise[2]. With the invention of DMSs, the door was open to WDM applications featuring competing channel spacings. It allowed the usage of soliton propagation characteristics to be applied for high-capacity long-haul system applications.

3.2.2 Pulse dynamics of DMS

Design of initial pulse power and width is critical for successful propagation of DMS. One important parameter determining the DMS behavior is the dispersion map strength S, given as [139]

$$S = \frac{\lambda^2}{2\pi c}\frac{(D_1 - D_{ave})L_1 - (D_2 - D_{ave})L_2}{T_0^2} \tag{3-11}$$

1. See also Figure 3-2, p. 40.
2. See Chapter 4, p. 46 for details.

where D_1, D_2 are the dispersion coefficients, and L_1, L_2 are the lengths of the anomalous and normal dispersion spans, respectively,

$D_{ave} = \frac{D_1 L_1 + D_2 L_2}{L_1 + L_2}$ is the average dispersion of the dispersion map.

S determines for instance the ratio of minimum and maximum pulse width over a single dispersion map [38]

$$\frac{T_{F,max}}{T_{F,min}} = \sqrt{1 + \frac{S^2}{2}}. \tag{3-12}$$

Utilizing the advantages of DMS propagation in the anomalous dispersion regime on the one hand, and avoiding interactions with neighboring pulses on the other hand, the dispersion map strength should be in the range of $4 \le S \le 10$ [21].

Also, the energy scaling with respect to classical soliton propagation can be derived as function of S. Several approaches have been published, for proper energy scaling [138], [159], [162], [163]. Using so-called second order moment analysis, the ratio between DMS energy E_{DMS} and energy of the classical soliton E_S can be determined for a two-section dispersion map as [16]

$$\frac{E_{DMS}}{E_S} \approx 1.18 \left[\frac{1 + 1.92 S^2}{\left(1 + \sqrt{1 + \frac{\varepsilon}{1-\varepsilon} 1.92 S^2}\right)^2} \right] \quad \text{with } \varepsilon = \frac{D_{ave}}{D_1}. \tag{3-13}$$

The increase of power for DMS systems compared to classical soliton systems using pulses of comparable duration results in an increased optical signal-to-noise ratio (OSNR)[1] without the need to increase the average dispersion. This is advantageously as it allows higher robustness against ASE-noise induced timing jitter and amplitude fluctuations[2].

Dispersion-managed solitons are not sech-shaped anymore; they tend to be more Gaussian-shaped. In general, it is difficult to determine the proper pulse shape, width and power for a DMS, as these parameters depend strongly on the applied dispersion map and amplifier positioning. There are

1. See Chapter 6, p. 100 for definition.
2. See Chapter 4, p. 46 for further explanations.

three main rules for launching the proper DMS into a system, and thus avoid energy shedding throughout the propagation [150]. Firstly, pulses should be launched with the proper frequency chirping at the correct points into the dispersion map. Secondly, the energy of the launched pulse should match the energy of the true DMS solution for the particular dispersion map. Thirdly, the pulse shape should be close to the true DMS solution to reduce oscillations of pulse width and power. A method for finding optimal dispersion maps including chirp-free points is presented in [160].

Using the so-called variational approach [10], pulse dynamics based on the Gaussian ansatz can be derived, that is, assuming that the DMS shape is Gaussian with variable amplitude, width, chirp and phase [58]. In [152], the so-called path-average mapping method is applied to derive an analytical expression for the transfer function[1] of a single section of a periodically cascaded DMS system. It is based on the assumption that nonlinear effects are small over one span length, such that the quasi-linear evolution of main pulse parameters can be assumed. This method is of advantage when the dispersion span length is much larger than the amplifier spacing and a low power signal is propagated. In the path-average model, the complex envelope of DMS can be described using an orthogonal set of chirped Gauss-Hermite functions [150].

However, it is not important that the launched pulse reflects exactly the true GNLS solution of the considered dispersion-managed fiber link. When selecting the shape of the launch pulse, it should have steeply falling tails. The extinction ratio should be at least 15 dB for 10 Gbit/s, and 20 dB for 20 Gbit/s.[2] It is not essential that the DMS is launched with the correct pulse width [62].

Figure 3-2 shows typical DMS pulse evolution over a symmetric dispersion map, e.g., anomalous and normal dispersion fiber spans are of equal lengths[3]. Here the DMS is found to be approximately of Gaussian shape with 16.74 ps FWHM duration and 2.8 mW peak power at the middle of the normal dispersion fiber, where it is launched. Note that no chirp is added.

1. Typically a nonlinear, integral operator.
2. Measured 50 ps away of the pulse center.
3. Details of the dispersion map are listed in Table 4-1, p. 57.

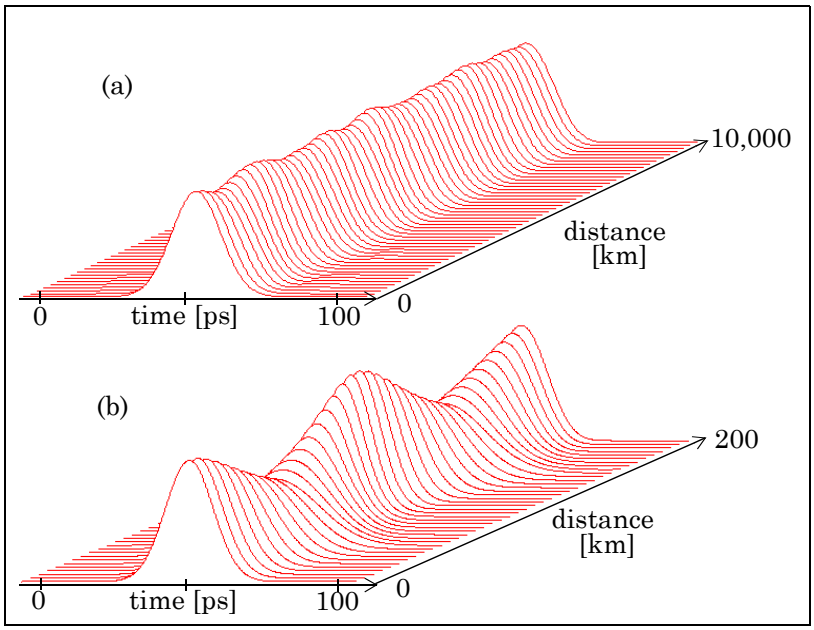

Figure 3-2. *Evolution of dispersion-managed soliton. (a) over 10,000 km with snap shots after each dispersion map (200 km), (b) over one dispersion map of 200 km, (no fiber attenuation). Details of the dispersion map are listed in Table 4-1, p. 57.*

The upper graph in Figure 3-2 shows stable evolution over 10,000 km, where snap shots are taken after each dispersion map. Slight modifications of pulse peak power and width are recognizable over the distance, which results from the fact that the launched Gaussian pulse is not the true solution of the propagation equation. The lower graph shows pulse dynamics inside the map, where pulse 'breathing' is recognizable. The DMS pulse width is smallest in the middle of the spans, and widest at the edges between anomalous and normal dispersion fiber spans, where chirp is broadening the spectrum as well.

3.3 Chirped return-to-zero (CRZ)

The first successful RZ propagation over long-haul distances employing no soliton technique was first proposed in [19] using the so-called chirped return-to-zero (CRZ) modulation format. CRZ pulses are typically following a raised-cosine shape with a superimposed sinusoidal phase modulation [51].

$$q(t) = A\cos\left[\frac{\pi}{2}\sin\left(\frac{\pi t}{T_b}\right)\right]\cdot\exp\left[jm_p\pi\cos\left(\frac{2\pi t}{T_b}\right)\right] \qquad -\frac{T_b}{2} < t < \frac{T_b}{2} \qquad (3\text{-}14)$$

where A is the maximum amplitude, T_b is the bit duration,

m_p is the modulation depth of phase modulation.

The FWHM width is approximately 33% of the bit duration. For comparison, the FWHM width of a typical DMS pulse is approximately 15 – 20% of the bit duration.

The main difference of CRZ and DMS systems lies in the applied dispersion maps. While dispersion maps of DMS systems have originally been designed such that pulses do not spread outside the bit duration, CRZ systems used from their first implementation dispersion maps where pulses accumulate large values of dispersion before they are compensated again. Strong pulse to pulse interactions are the result. However, the initial pulse peak power and width are selected such that these interactions are of linear nature and could easily be reversed by proper dispersion compensation. While DMS dispersion maps have a length of 100 – 200 km with 2 – 4 amplifiers in between, CRZ systems employ dispersion maps of length 250 – 550 km with 5 – 11 amplifiers in between. The CRZ pulse shape is usually totally destroyed over the dispersion map length, recovering only at its end again. In the presence of non-negligible dispersion slope, pulses might be detectable only when channel by channel compensation for the dispersion slope is applied at the transmitter and receiver ends [51].

Figure 3-3 shows pulse evolution of a CRZ over a mostly anomalous dispersion map[1].

1. Details of the dispersion map are listed in Table 5-4, p. 87.

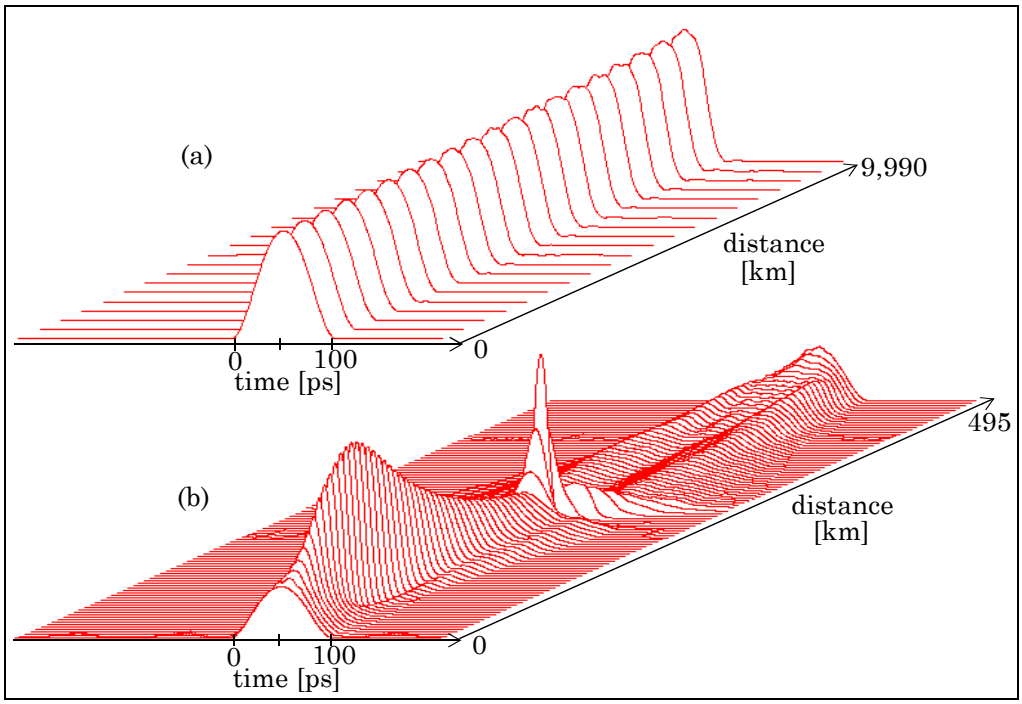

Figure 3-3. *Evolution of CRZ. (a) over 9,990 km with snap shots after each dispersion map (495 km), (b) over one dispersion map of 495 km, (no fiber attenuation). Details of the dispersion map are listed in Table 5-4, p. 87.*

The CRZ pulse is launched at about the middle of the normal dispersion fiber. An optimum pre-chirping at the fiber input is of key importance for successful propagation. In [161], several lists are derived for selecting the optimum chirp required for CRZ pulses depending on the applied dispersion map. General design goal is to produce a chirp-free pulse at the receiver, which corresponds to a pulse with minimum time-bandwidth product, and thus minimum crosstalk with other pulses in time and frequency. For the evolution diagram in Figure 3-3, a depth of the phase modulation of m_p = 0.6 was used. The upper graph in Figure 3-3 shows stable evolution over 9,990 km, where snap shots are taken after each dispersion map. The pulse shape changes with distance, however, retains a well detectable format. The lower graph shows pulse dynamics inside the map. Strong pulse dynamics inside the map lead to pulse power spreading over neighboring bits on the one hand, and development of large, sharp-edged power spikes on the other hand.

The CRZ transmitter design is quite complex, as the combined modulation of amplitude and phase requires a set of cascaded external modulators. Recently, the first integrated CRZ transmitter for 10 Gbit/s has been demonstrated, which eases application tremendously as board space and insertion losses between the components is reduced [57]. Also, an alternative way of generating CRZ pulse streams is published recently, which allows CRZ modulation with only a single MZM [100] or electro-absorption modulator [135]. However, more effort need to be put into the generation of the proper electrical drive voltage.

3.4 Convergence of DMS and CRZ schemes

There have been debates as to whether DMS or CRZ systems will be the best performing modulation format for the future. It began with the discussion of whether soliton or NRZ propagation is the optimal choice. While soliton systems evolved into DMS systems over the years, CRZ evolved from design aspects typically applied to NRZ systems. Recent suggestions for DMS systems apply ultra-short dispersion maps. They are especially designed for high-speed applications (≥ 40 Gbit/s), while maintaining narrow channel spacings [76], [151]. Other suggestions go in the direction of applying dispersion maps with high local dispersion values (SMF) resulting in large map strengths S [9]. When S is increased, interactions between pulses become larger. So pulse powers need to be reduced, which limits the average dispersion that can be balanced by fiber nonlinearities. Thus, with increased map strength S DMS propagation transits toward the quasi-linear propagation regime of CRZ systems.

Remaining differences between DMS and CRZ systems are the different dispersion map lengths and local dispersion values, as well as launch points, which determine the initial pulse shapes and chirps. While DMS are typically launched close to a chirp-free point[1] in the dispersion map, where the

1. Point in the dispersion map, where the pulse representing the optimal DMS solution is chirp-free. This point does not need to exist.

time-bandwidth product is minimum, CRZ pulses are launched at points requiring a large initial pre-chirp. In [124] a comparison was presented between a typical CRZ system experiment [20] and a recent experiment of a DMS system [63]. The dispersion maps for both systems are very different, and so is the pulse evolution. However, similar propagation behavior is observed, when the launch power and ASE noise build-up are scaled properly by the applied amplifier spacings and total transmission distances. Both systems support fiber nonlinearities and operate in a quasi-linear mode.

Modern systems will utilize RZ modulation formats, which incorporate the flexibility of DMS with respect to SPM and dispersion effects, and the robustness against nonlinear multichannel effects (XPM, FWM) of CRZ. One candidate is the modulation format carrier suppressed return-to-zero (CS-RZ). It modulates neighboring RZ pulses with an alternating relative optical phase difference of π. This alternating phase results in carrier suppression of the generated RZ format. The effect is a reduced sensitivity against intrachannel pulse distortions, but also an increased signal bandwidth.

The superior performance of CS-RZ has been demonstrated in recent high-speed transmission experiments [74]. In [94] dense WDM applications (50x20 Gbit/s) employing pure RZ, CS-RZ and SSB-RZ have been compared over long-haul distances (4,000 km). CS-RZ performed best, promising to be the ideal solution for suppressing linear and nonlinear interactions. In another long-haul experiment [25], it has been demonstrated that CS-RZ was outperformed by the CRZ modulation format. However, this was mainly achieved because of received filters were optimized for the CRZ modulation format.

Chapter 4

Modeling of timing jitter

4.1 Overview

In Chapter 3, p. 37, general conditions were presented for building nonlinearity-supporting, dispersion-managed soliton (DMS) systems operating in a stable regime over optical fiber. This chapter investigates propagation distortions of DMSs and other RZ pulse shapes.

There are actually many different sources responsible for pulse degradations. A distinction can be made between distortions causing energy fluctuations and pulse position fluctuations. While mostly negligible for NRZ systems, the impact of timing jitter on overall system performance is not negligible in WDM systems using RZ modulation formats. Initially low, timing deviations accumulate over distance from small perturbations, to eventually become of system limiting importance.

This chapter provides an overview of the main sources of timing jitter in long-haul WDM RZ transmission systems, and presents modeling techniques used to investigate them. After listing the main distortions and their typical impact on system performance, two dominating sources of timing jitter are investigated in more detail.

Firstly, ASE-noise added by optical amplifiers along the transmission line influences not only the pulse energy but also the relative frequency position of the propagated pulses. These frequency shifts are stochastic in nature as pulses experience different amounts of random ASE-noise. Secondly, pulses propagating in different WDM channels collide with each other due to their different propagation velocities. These collisions introduce residual fre-

quency shifts in the presence of non-negligible interchannel XPM efficiency. Because of the randomness of channel bit streams, each pulse accumulates an individual frequency shift. Due to fiber dispersion, random frequency shifts lead to a variation of channel velocities with time, and thus timing jitter.

For each of the two sources of timing jitter, estimation techniques are presented, which are the basis for semi-analytical algorithms. They solve numerically an analytically derived solution for the pulse central time variance considering local pulse shape information, which is gathered by solving the generalized nonlinear Schrödinger equation (GNLS) using the split-step Fourier method[1]. These algorithms allow a reduction in computational effort by orders of magnitude compared to full numerical simulations. For many long-haul WDM RZ transmission systems, these fast techniques make system parameter optimization possible, as scanning of large parameter sets becomes feasible.

4.2 Main system distortions

4.2.1 Noise from optical amplifiers

Long-haul transmission links experience performance degradations due to ASE-noise from optical amplifiers[2] along the line. In transoceanic systems, over 100 amplifiers are cascaded; each of them adds noise onto the signal stream. Besides changing the pulse energy, ASE-noise affects the pulse position in nonlinear pulse propagation as well. In fact, it turned out that ASE-noise induced timing jitter (ANTJ) is the ultimately limiting effect in single channel soliton propagation. For more linear propagation scenarios, as the case for CRZ systems, energy fluctuations especially noise accumulation at spaces has a more severe impact on system performance.

1. See Chapter 2, p. 17 for details.
2. See Chapter 2, p. 20 for details on noise generation in optical amplifiers.

Disturbing effects of ASE-noise are closely dependent on amplifier spacing, Noise Figure, and fiber dispersion. A detailed discussion will be given in Chapter 4, p. 51. Examples of system simulations will be presented in Chapter 5, p. 78.

4.2.2 Intrachannel pulse-to-pulse interactions

In order to increase the throughput in fiber-optic communication systems, it is tempting to increase the bitrate per channel while maintaining a narrow channel spacing. However, pulses in neighboring bit intervals tend to interact with each other, if they are placed too close together. When estimating the impact of intrachannel pulse-to-pulse interactions[1], it is helpful to distinguish between nonlinearity-supporting systems, like soliton or DMS systems, and quasi-linear systems.

Soliton and DMS systems

Interactions between neighboring solitons introduce timing jitter, and finally the collapse of the solitons, if the initial soliton separation in time is not wide enough[2]. To maintain a safe pulse separation, the pulse width needs to be reduced and peak powers increased, when the channel bitrate is increased. This is possible to some extent but hardly efficient for bitrates of 40 Gbit/s over NZDSF, for example. However, it has been shown that pulse separation can be halved, if neighboring pulses are launched in orthogonal polarizations [122]. The parameters of the investigated DMS system simulations in this work are selected such that pulses propagate in regions of safe pulse separation, and hence, pulse interactions are negligible.

Quasi-linear systems

In quasi-linear systems, the dispersion length L_D is much shorter than the nonlinear length L_{NL}. Thus, pulses change rapidly their power distribution in time due to dispersion-induced pulse spreading and compression over L_{NL}, which results in an averaging out of nonlinear propagation effects[3] [112]. Pulse-to-pulse interactions in quasi-linear systems can be best

1. Dependence of pulse propagation from other pulses in the same channel.
2. As outlined in Chapter 3, p. 34.
3. See also Chapter 3, p. 41.

described by time-equivalent terms of FWM and XPM, namely intrachannel four-wave mixing (I-FWM) and intrachannel cross-phase modulation (I-XPM) [40], [102]. I-FWM induces pulse echoes, which grow logarithmically with distance and decrease with the square of the pulse separation. I-XPM induces timing jitter, which can be described by the variance of the pulse central time for the case of two interacting pulses of Gaussian shape as [30]

$$\sigma_t^2 = \frac{(C\gamma P)^2}{|\beta_2|}\left(\frac{T_F}{T_b}\right)^3 \tag{4-1}$$

where T_b is the bit duration, T_F is the FWHM pulse duration,

β_2 is the GVD, γ is the nonlinear coefficient,

P is the optical pulse power,

C is a term considering pulse chirp and fiber loss versus distance.

Pulse-to-pulse interactions in quasi-linear systems become important for high bitrate (≥ 40 Gbit/s) transmission. Also, it has been shown that for a careful selection of the dispersion map, the timing jitter due to pulse-to-pulse interactions can be drastically reduced [30], [107]. Thus, it will not be regarded in the following analysis.

4.2.3 Interchannel cross-phase modulation

In WDM systems, pulses propagate with different velocities. This leads to interchannel interferences[1] caused by unbalanced collisions between pulses of different channels [164], [118]. This effect is schematically shown in Figure 4-1 for a collision between two pulses. When the faster traveling pulse approaches the slower traveling pulse, both pulses are attracted to each other, due to cross-phase modulation. As a result, their velocities modify slightly, i.e., the faster traveling pulse becomes slower and the slower traveling pulse faster. While both pulses are at the same location, no velocity modifications occur. When the faster traveling pulse finally passes the slower traveling pulse, both pulses repel each other; again under slight modification of their velocities. But this time, the correction of the velocities is in the opposite direction. Due to fiber attenuation, the temporal velocity changes

1. Dependence of pulse propagation from pulses in neighboring channels.

induced by XPM do not cancel each other out completely. Thus, the pulses shift in time.

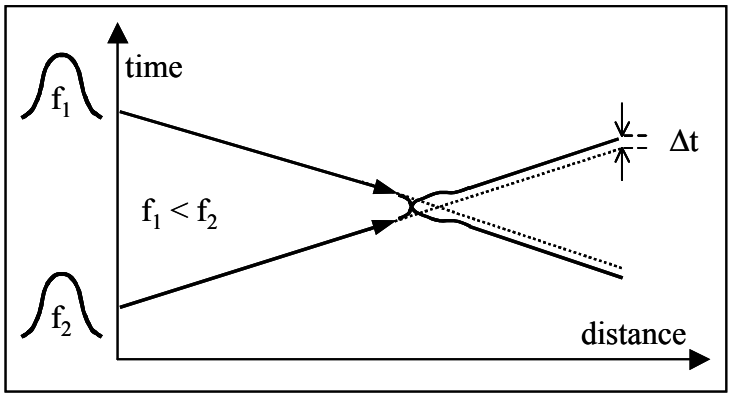

Figure 4-1. *Collision between two pulses in frequency-separated channels results in deviation from original central time (drawn for anomalous dispersion regime).*

The net timing shift of each pulse in a WDM transmission system depends on the number of collisions it experiences, and the pulse power during collision. As the propagated bit sequences are usually random, each pulse experiences a unique shift in time, which results in random pulse position deviations at the detector. This effect is called collision-induced timing jitter (CITJ), or XPM-induced timing jitter. CITJ is one of the major sources of bit errors in WDM RZ systems. The individual time shifts are strongly dependent on the relative velocity difference between the colliding pulses, and their pulse shape and power during the collision. Hence, the applied dispersion map, the number of WDM channels, and their spacing, as well as the positioning of optical amplifiers are of strongest influence for the accumulation of XPM-induced timing jitter.

In Chapter 4, p. 59, techniques for estimating CITJ are presented. In Chapter 5, p. 81, results of WDM system simulations are presented, which help to determine the accumulation behavior of CITJ in dependence on various system parameters.

4.2.4 Others

In the following, additional distortion effects are listed. They are not regarded in detail in this work, as they are of no importance and cannot be discussed in depth without broadening the scope of this work.

Polarization dependent propagation effects

The polarization dependence of optical fiber links might introduce severe system degradations in optical communication systems [45], [48]. In particular, systems employing high bitrates of 40 Gbit/s or systems covering large distances are affected. In long-haul transmission, pulses suffer mainly from the coupled effect of polarization mode dispersion (PMD) in the fiber and polarization dependent loss (PDL) in the optical repeater blocks. For details on nonlinear propagation problems in the presence of PMD, see [79].

Transmitter and receiver imperfections

Beside direct fiber propagation effects, which might translate into timing jitter of the received pulse sequence, imperfections of the optical transmitter might add to these pulse position fluctuations. The initial timing jitter of laser sources used as carriers in external modulation transmitters is usually of less importance. More important is the initial phase noise of optical carriers, which translates into pulse position fluctuations during propagation as a direct result of fiber dispersion. The induced timing jitter, defined by the variance of pulse position fluctuations, can be derived for a classical soliton to be [156]

$$\sigma_t^2(z) \approx \delta f \cdot \frac{2}{3}\pi \sqrt{\frac{|\beta_2|^3}{L_D}} z^2 \tag{4-2}$$

where δf is the carrier linewidth,

L_D is the dispersion length, as defined in Eq. (2-25),

β_2 is the group velocity dispersion,

z is the transmission distance.

Note that the timing jitter scales with distance squared. For example, the linewidth-induced timing jitter is about $\sigma_t^2 = 2.04\ \text{ps}^2$ for $\delta f = 12$ MHz, $D = 0.1$ ps/nm-km, $\lambda = 1550$ nm, $T_0 = 20$ ps, and $z = 10{,}000$ km.

Additionally to imperfection at the transmitter, the optical receiver might add to the accumulated timing jitter. At the decision circuitry in the optical receiver, the pulse sample circuit and the received pulse stream need to be synchronized. This synchronization is usually performed using a phase locked loop, which might be infected by timing fluctuations itself.

FWM and dispersive waves

Four wave mixing between WDM channels can lead to crosstalk, as discussed in Chapter 2, p. 13. For most of the scenarios discussed in this work, FWM impact is considered to be of additive character or even negligible, as the FWM efficiency is small due to the fast walk-off of channels[1].

When launching nonlinearity supporting RZ pulses into the fiber with pulse shape, power, width and chirp not exactly corresponding to a solution of the nonlinear propagation equation, pulse energy will be reduced, under emission of dispersive waves, until the transmitting pulse is transferred to a stable solution of the propagation equation[2]. Throughout this work, great care is taken to launch proper pulses into the fiber, and thus omit pulse distortions caused by energy shedding effects. However, this has not always been achieved.

Some of the discrepancies in comparing approximation techniques for timing jitter and BER with full numerical simulations, which are performed in Chapter 5 and Chapter 6, p. 112, arise from FWM and dispersive waves.

4.3 Timing jitter due to optical inline amplification (ANTJ)

4.3.1 Motivation

The ASE-noise induced timing jitter was calculated for the first time by Gordon and Haus [53]. They applied linearization approximation to the ana-

1. See Figure 2-2, p. 15 for details.
2. See also Chapter 3, p. 35.

lytically known soliton solution for the case that noise energy is much lower than signal energy. For a classical soliton system employing equally spaced, lumped amplifiers, the variance of the pulse central time due to ASE-noise induced timing jitter (ANTJ) can be written as [82]

$$\sigma_t^2 \approx \gamma\alpha S_{ASE}\frac{L_{eff}}{L_A}T_0\left[\frac{\pi^2}{12}L_D z + \frac{1}{9}\frac{1}{L_D}z^3\right] \tag{4-3}$$

where γ is nonlinear coefficient as defined in Eq. (2-19),

α is the fiber attenuation,

$S_{ASE} = P_{ASE}/\Delta f$ is the power spectral density of ASE-noise in a single polarization as defined in Eq. (2-33),

L_{eff} is the effective length as defined in Eq. (2-23),

L_D is the dispersion length as defined in Eq. (2-25),

L_A is the amplifier spacing, z is the propagation distance,

T_0 is the pulse duration (half-width 1/e-intensity).

The first term in the brackets of Eq. (4-3) denotes the effect of direct coupling of ASE-noise power onto the soliton pulse. It increases in proportion with distance and in inverse proportion with dispersion. The second term denotes the Gordon-Haus effect, e.g., the coupling of ASE-noise with the soliton spectrum, which causes a random walk of the pulse central frequency, and thus its velocity. It increases proportionally with dispersion and with the cube of distance, and is thus the dominating effect for soliton propagation[1].

Several techniques were proposed to reduce or even limit ASE-noise induced timing jitter. Weak spectral filtering can be applied to control the soliton central frequency and thus its position in time [110]. It has been shown that the growth of ANTJ with distance could be reduced from cubic to linear. As filters reduce the soliton energy, excess gain needs to be provided by the inline amplifiers, which will increase ASE-noise build-up just at the main soliton frequency range. This problem has been overcome by implementing sliding spectral filters along the link, which slide the solitons slowly

1. Note that Eq. (4-3) is derived for classical soliton systems, e.g., it tends to go to zero when the dispersion goes to zero.

into different frequency regions, leaving the ASE-noise behind as it is not moving with the filter [119].

When ANTJ should be limited, active devices need to be put on the link, which lock the soliton to a fixed position in time. One approach is to use amplitude modulators, which however, destabilize the soliton propagation. So amplitude modulation is applied together with frequency filters, which compensate this instability again [126]. Another way to reduce ANTJ in soliton systems is by using one or multiple phase modulators along the transmission line [136]. The phase modulation translates into frequency modulation, which in the presence of filters translates into amplitude modulation again.

All these techniques have been proposed for classical soliton systems. However, they are also applicable to DMS systems, eventually with less degree of effectiveness. Additionally, it has been demonstrated experimentally [146], [26] and proven theoretically [98] that ANTJ is naturally reduced in DMS systems compared to classical soliton systems, due to the required power enhancement.

4.3.2 Linearization approximation for arbitrary pulse shapes

In the following, an approach is presented, which extends the idea of the *linearization approximation* that it holds for arbitrarily shaped RZ pulses, which solve the perturbed GNLS. The derivations presented below are lent from [60].

4.3.2.1 Modeling

The approach is based on a normalized version of the GNLS, as given in Eq. (2-19), considering small perturbations due to additive ASE-noise. It can be written using the Langevin form[1] as follows.

$$j\frac{\partial q}{\partial z} + \frac{1}{2}D\frac{\partial^2 q}{\partial t^2} - C|q|^2 q = jgq + N \tag{4-4}$$

1. Based on notations first time used in [73].

where $|q(z,t)|^2$ corresponds to the photon flow, with $q(z,t) = A(z,t)/\sqrt{hf}$, with hf photon energy,

z is the transmission distance multiplied by $\beta_{2,0}$, with $\beta_{2,0}$ arbitrary scaling dispersion[1],

t is the retarded time given by $t = \tilde{t} - \beta_1 z$,

$D(z)$ is the local dispersion divided by $\beta_{2,0}$,

$C = hf\gamma/\beta_{2,0}$, with γ nonlinear coefficient,

$g(z)$ is the local fiber loss/gain normalized to $\beta_{2,0}$, given by

$$g(z)\beta_{2,0} = \begin{cases} g_0 & kL_A < z < kL_A + L_{Amp} \quad k = 1, 2, \ldots, \\ -\alpha/2 & otherwise \end{cases} \tag{4-5}$$

with α fiber attenuation, $g_0 = \ln(G)/(2L_{Amp})$, G gain per amplifier, L_{Amp} fiber length of amplifier, and L_A amplifier spacing,

$N(z,t)$ accounts for small perturbations due to ASE-noise. In the case of lumped amplifiers its autocorrelation function is given by

$$\langle N(z,t), N^*(z_1,t_1)\rangle = \psi(z)\delta(z-z_1)\delta(t-t_1) \tag{4-6}$$

with $\psi(z) = \begin{cases} 2g_0 n_{sp} & kL_A < z < kL_A + L_{Amp} \quad k = 1, 2, \ldots, \text{ and} \\ 0 & otherwise \end{cases}$

n_{sp} spontaneous emission factor.

Figure 4-2 shows the assumed pulse power profile versus distance.

1. Typically average dispersion of the dispersion map.

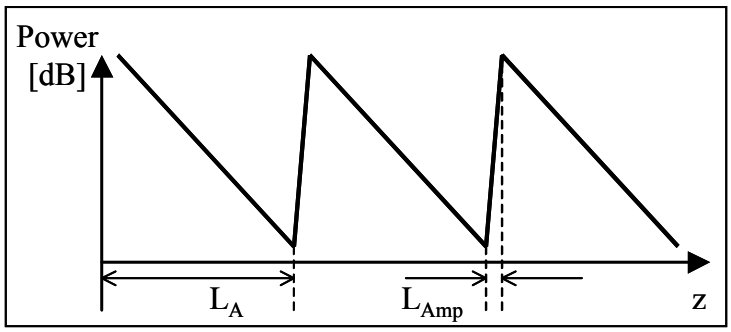

Figure 4-2. *Power profile versus distance.*

To derive statistics of pulse position fluctuations, it is helpful to define central time and frequency of q by its center of mass in time and frequency, respectively, as

$$T = \frac{1}{U}\int_{-\infty}^{\infty} t|q|^2 dt \qquad \Omega = \frac{1}{U}\int_{-\infty}^{\infty} \mathrm{Im}\left(\frac{\partial q}{\partial t}q^*\right) dt \tag{4-7}$$

where $U = \int_{-\infty}^{\infty} |q|^2 dt$ is the pulse energy.

Ignoring pulse spreading outside the bit interval, integration in Eq. (4-7) needs to be performed over a single bit only[1]. Differentiating T and Ω with respect to z and using Eq. (4-4) one obtains the following dynamic equations for central time and frequency

$$\frac{d}{dz}T = D\Omega + \frac{2}{U}\int_{-\infty}^{\infty} (t-T)\mathrm{Im}(Nq^*)dt \tag{4-8}$$

$$\frac{d}{dz}\Omega = -\frac{2}{U}\Omega\int_{-\infty}^{\infty} \mathrm{Im}(Nq^*)dt + \frac{2}{U}\int_{-\infty}^{\infty} \mathrm{Re}\left(N\frac{\partial}{\partial t}q^*\right)dt\,. \tag{4-9}$$

Eq. (4-8) can be solved directly with respect to Ω yielding two contributions to the deviations of the pulse central time as follows

$$\begin{aligned} T &= \Delta F + \Delta T \\ &= \int_0^z D\Omega(N)dz + \int_0^z \frac{2}{U}\left[\int_{-\infty}^{\infty} (t-T)\mathrm{Im}(Nq^*)dt\right]dz\,. \end{aligned} \tag{4-10}$$

1. Note that when ISI effects should be taken into account, integration needs to be performed over multiple bit durations.

As seen from Eq. (4-10), timing deviations are due to the superposition of two effects, namely noise-induced frequency shifts in the presence of fiber dispersion (ΔF), and the direct overlay of noise onto the pulse (ΔT).

Following the derivations in [60], the variance of the pulse central time can be calculated from Eq. (4-9) and Eq. (4-10) yielding three contributing terms:

$$\sigma_t^2 = \langle T^2 \rangle - \langle T \rangle^2 = \langle \Delta F^2 \rangle + 2\langle \Delta F \cdot \Delta T \rangle + \langle \Delta T^2 \rangle \tag{4-11}$$

with

$$\begin{aligned} A &= \langle \Delta F^2 \rangle = 2\int_0^z D(z_1)\left\{\int_0^{z_1} D(z_2)\left[\int_0^{z_2} \psi\left(\int_{-\infty}^{\infty} \left|\frac{\partial}{\partial t}\tilde{q}\right|^2 dt\right)/U^2 dz_3\right] dz_2\right\} dz_1 \\ B &= 2\langle \Delta F \cdot \Delta T \rangle = 2\int_0^z D(z_1)\left[\int_0^{z_1} \psi\left(\int_{-\infty}^{\infty} \mathrm{Re}\left(\tilde{q}^* \frac{\partial}{\partial t}\tilde{q}\right) dt\right)/U^2 dz_2\right] dz_1 \\ C &= \langle \Delta T^2 \rangle = \int_0^z \psi\left(\int_{-\infty}^{\infty} (t-T)^2 |\tilde{q}|^2 dt\right)/U^2 dz_1 \end{aligned} \tag{4-12}$$

where $\tilde{q} = q\exp(-j\Omega t)$ is the field description for the retarded frequency, meaning that the pulse is investigated during evolution over the fiber at its central frequency defined in Eq. (4-7),
$\psi(z)$ is defined in Eq. (4-6).

Term A denotes the contribution from frequency shift alone, and term C denotes the contribution from direct time offset alone. Term B represents the contribution caused by pulse chirp, which could be understood as interference between time and frequency shift. Consider a chirped pulse, meaning that its local frequency depends on time. An ASE-noise induced time offset would lead to a frequency shift, which would translate in additional time shift. Depending on the actual RZ system under investigation, the individual terms vary in importance.

The result in Eq. (4-12) differs from the classical theory of ANTJ derived by Gordon and Haus [53]. Firstly, term A is proportional to the pulse bandwidth squared over the pulse energy squared. Secondly, term B is totally new as initial derivations are derived for the fundamental soliton solution[1], which is not chirped.

1. See Chapter 3, p. 32 for details.

4.3.2.2 Numerical implementation

Eq. (4-11) and Eq. (4-12) completely determine the variance of the pulse central time. The numerical implementation is straightforward.

1. Calculate the propagation of the pulse shape q by numerically solving the GNLS given in Eq. (2-19) for one signal pulse per channel.
2. Substitute the calculated pulse shape per distance q in Eq. (4-12) and calculate the variance of the pulse central time σ_t^2.

The model is implemented in an iterative algorithm. Calculation of ANTJ is very sensitive to correct capturing of local propagation characteristics of signal pulses. Thus, it is important to choose the step sizes such that a certain dispersion-length product per step is not exceeded. The main advantage of the presented algorithm is that it dramatically reduces the computational effort compared to full numerical simulations, as it is not necessary to simulate the propagation of a long stream of pseudo-random bits in order to find numerical estimates of the central time variance.

4.3.2.3 Validation

The approach has been validated, both numerically and experimentally in great detail [60]. One validation case is presented below, other application examples are discussed in Chapter 5, p. 78.

A typical single channel DMS system with a bitrate of 10 Gbit/s is considered here. The initially Gaussian pulses are launched with a peak power of 2.8 mW and a FWHM duration of 16.75 ps. The dispersion map parameters are described in Table 4-1.

Table 4-1. *Parameters of dispersion map A.*

L_1	100.0	km	D_1	2.34	ps/nm-km
L_2	100.0	km	D_2	-2.19	ps/nm-km
L_{launch}	50.0	km			
L_A	50.0	km			

Figure 4-3 illustrates graphically the meaning of parameters listed in Table 4-1. The dispersion map consists of a span of anomalous DSF with dis-

persion D_1 and length L_1, and a span of normal DSF with dispersion D_2 and length L_2. Amplifiers are spaced in distance by L_A. They are placed at the midpoints and the edges of each span. Pulses are launched in each channel at L_{launch}, here, from the middle of the anomalous dispersion span.

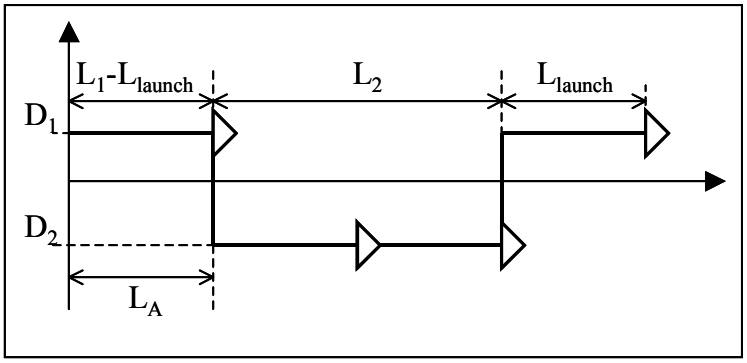

Figure 4-3. *Schematic of dispersion map A.*

Figure 4-4 shows ASE-noise induced timing jitter versus distance for NF = 6.3 dB of all inline amplifiers [132]. Timing jitter results are compared with data gathered by propagating random streams of 256 bits and estimating the variance of the pulse position from the received pulse sequence directly (full numerical simulations). Excellent agreement is observed.

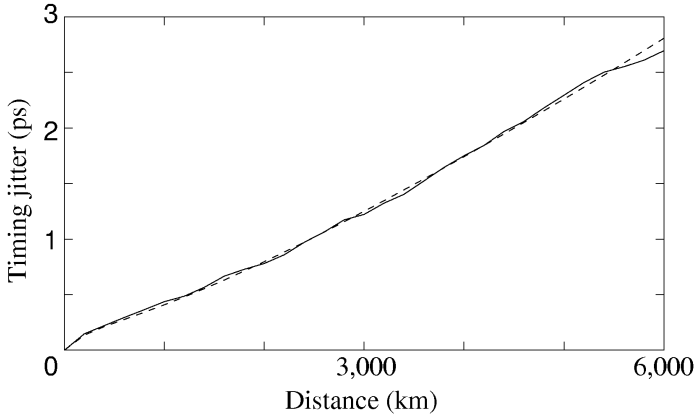

Figure 4-4. *ANTJ versus distance for a single channel system. Results of linearization approximation (dashed line) are compared with results using full numerical simulations (solid line). Dispersion map A was applied (see Table 4-1).*

4.4 Timing jitter due to interchannel cross-phase modulation (CITJ)

4.4.1 Motivation

One of the major sources of bit errors in WDM systems using RZ modulation formats is collision-induced timing jitter (CITJ). It arises from nonlinear interactions of pulses in different WDM channels due to cross-phase modulation[1]. So it is also called XPM-induced timing jitter.

This topic has been subject to extensive studies over the past years, resulting in different approximation techniques for XPM-induced timing jitter. The residual wavelength shift of a two-soliton collision can be derived to [118], [88]

$$\Delta\lambda(z) = \sum_{m=1}^{\infty} c_m \sin\left[\frac{2\pi m z}{L_A} - \tan\left(\frac{2\pi m}{\alpha L_A}\right)^{-1}\right] \tag{4-13}$$

where z is the position of collision, L_A is the amplifier spacing,

$$c_m \approx 0.2274 \frac{\lambda^2}{c T_F} \frac{L_A}{L_D} \frac{m^3 x^4}{\sinh(mx)^2}\left[1 + \left(\frac{2\pi m}{\alpha L_A}\right)^2\right]^{-0.5},$$

with T_F FWHM duration of the soliton, L_D dispersion length,

$x \approx 2.8 L_c / L_A$, L_A amplifier spacing, L_c collision length[2].

It has been found that when the collision length L_c is at least four times larger then the amplifier spacing L_A, the spectral shift resulting from a collision between two solitons can be neglected [118]. With Eq. (2-24), this implies a maximum channel spacing of approximately

$$\Delta\lambda_{12} < 0.15 \frac{T_F}{|D| L_A}. \tag{4-14}$$

1. See Chapter 2, p. 12 for details on XPM.
2. See Chapter 2, p. 19 for the definition of L_D and L_c.

Similar to Eq. (4-13), approximations of the residual frequency shift are found for Gaussian-shaped dispersion-managed solitons (DMS) [37], [143], [2], [128], [145] or the induced time shift directly [90]. It was shown that DMS suffer less from interchannel pulse collisions compared to classical solitons [75]. In [144], the dispersion map is optimized to minimize the accumulated CITJ for a DMS system.

All the methods mentioned so far have in common that they only consider two-pulse collisions. In [41] three-pulse collisions were analyzed. In [27] the solution of N coupled GNLS is derived, where each GNLS describes the propagation of an individual, frequency-shifted soliton. One important result from this work is that an approximate formula for the total collision-induced frequency shift is gained by considering the superposition of all the individual two-soliton collisions. In [88], the randomness of the propagated bit streams is taken into account. The CITJ of channel m was estimated for an amplified soliton system with N channels to

$$\langle \Delta t^2 \rangle_m \approx \sum_{\substack{k \\ k \neq m}} \left(\frac{T_b}{\Delta\lambda_{mk}} \right)^2 \left(\frac{L}{Z_{mk}} \right)^3 \frac{\langle \Delta\lambda_{mk}^2 \rangle}{6} \tag{4-15}$$

where T_b is the bit duration,

$\Delta\lambda_{mk}$ is the spacing between channel m and k,

L is the propagation distance,

Z_{mk} is the distance between collisions,

$\langle \Delta\lambda_{mk}^2 \rangle$ is the variance of wavelength shift, given by $\langle \Delta\lambda_{mk}^2 \rangle = \sum c_m^2$ with c_m defined in Eq. (4-13).

All the techniques presented above lack certain features, which limit their usability for more general applications. RZ pulse shapes applied in today's WDM systems may differ significantly from classical solitons or Gaussian-shaped DMS. Besides, the number of channels in modern WDM systems is typically larger than three. Their spacing is drastically reduced compared to the time of early soliton investigations. Thus, four and higher number pulse collisions must be considered when estimating the accumulation of timing jitter due to XPM.

Beside analytical approximations, another solution for estimating XPM-induced timing jitter would be to use full numerical simulations. However, the computational effort for such simulations is often very large, as it dramatically increases with the number of channels in the WDM system. This is due to two reasons. Firstly, the simulation bandwidth needs to be increased when adding more channels. In turn, the step size in distance[1] needs to be reduced to resolve the relatively fast sliding of channels due to their large difference in group velocity. Secondly, pseudo-random bit streams of at least the order of 100 need to be simulated per channel to reach a reasonable statistical confidence for the estimated variance of the pulse central time.

Figure 4-5 shows an example for the computational effort required to evaluate the timing jitter for a 10-channel WDM system with a transmission distance of 10,000 km using full numerical simulations. Note that the inverse of the time resolution defines the simulation bandwidth and that an *average* split-step size of 100 m is assumed. In practice, it would be set to an adaptive value depending on local peak power and dispersion.

Example:	10-Channel WDM Transmission		
bitrate	10 Gbit/s		
# of bits	256	fiber distance	10,000 km
time resolution	0.2 ps	split-step size	0.1 km
# of samples N	**131,072**	# of FFT's	**100,000**
# of flops/FFT	5 N $\log_2$(N) ≈ **11.14 x 10^6**		
total # of flops	≈ **1.11 x 10^{12}**		

Figure 4-5. *Estimation of numerical effort for calculating timing jitter using full numerical simulations based on the split-step Fourier method.*

According to benchmark tests of FFTW, a professional FFT package developed at MIT [46], approximately 90x10^6 flops per second are performed on a typical Pentium II with 300 MHz and 256 MByte RAM[2]. This leaves an

1. The differential distance step when solving the GNLS using the split-step Fourier method, see Chapter 2, p. 17 for details.

approximate run time of 2 hours and 25 minutes. The FFT accounts in average for about 70% of the calculation effort in the split-step Fourier method[1]. So all together, the time taken to estimate timing jitter for the presented scenario is of the order of three hours. Note that this time is needed for the estimation of only one point in an eventually multi-dimensional parameter space.

In summary, existing analytical or semi-analytical approximations are not applicable for general case RZ WDM systems. This leaves full numerical simulations which, however, are not at all suited for optimization tasks considering multiple system parameters. However, they serve as robust technique for gathering reference data when deriving new estimation techniques.

4.4.2 Elastic collision approximation for arbitrary pulse shapes

In this section, a semi-analytical approach is described, which results in the derivation of an efficient numerical algorithm to accurately evaluate collision-induced timing jitter in WDM systems with RZ modulation format. The key factor of this approach is to find an analytical description for the variance and the average of the pulse central time as a function of *arbitrary* pulse shape evolution with distance for each channel.

As shown in Chapter 4, p. 74 and Chapter 5, p. 86, the approach is valid for systems in which RZ signal pulses do not spread outside the bit length, and also for systems with large pulse spreading but low local pulse energies outside the bit interval.

4.4.2.1 Modeling

Details of the derivation below were published in [61].

Basic equations

The derivation starts with the normalized version of the GNLS given in Eq. (2-19) for the n-th pulse in channel m of a WDM system. When fiber loss

2. See [43] for details on the benchmark test results.
1. If no special effects, like stimulated Raman scattering are included.

is periodically amplified, and FWM is neglected, the dynamic propagation equation is given by

$$j\left[\frac{\partial}{\partial z}+\frac{1}{v_m}\frac{\partial}{\partial t}\right]q_{mn}+\frac{1}{2}D_m\frac{\partial^2}{\partial t^2}q_{mn}-\left[|q_{mn}|^2+2\sum_{\substack{k\\k\neq m}}\sum_{l}|q_{kl}|^2\right]q_{mn}=jgq_{mn} \quad (4\text{-}16)$$

where q_{mn} is the normalized field amplitude of the n-th bit in channel m given by $q_{mn}=A_{mn}\sqrt{\gamma L_D}$, with A_{mn} actual field amplitude,

γ nonlinear coefficient, L_D dispersion scale length, given by

$L_D=T_F^2/|\beta_{2,0}|$, with T_F FWHM pulse duration,

$|\beta_{2,0}|$ arbitrary scaling dispersion[1],

z is the transmission distance divided by L_D,

t is the time divided by T_F,

$v_m(z)$ is the group velocity of channel m divided by L_D/T_F,

$D_m(z)$ is the local dispersion $\beta_2(z)$ of channel m divided by $|\beta_{2,0}|$,

$g(z)$ is the net gain given by $\frac{g(z)}{L_D}=\begin{cases}G & z=kL_A\\ -(\alpha/2) & z\neq kL_A\end{cases}$ $k=1,2,\ldots,$

with α fiber attenuation and G amplifier gain.

The assumption that FWM can be neglected in Eq. (4-16) holds for cases of large wave vector mismatch, e.g., due to high local fiber dispersion values and reasonable channel separation[2].

To derive statistics for pulse position fluctuations, it is helpful to define central time and frequency of q_{mn} from its center of mass in time and frequency, respectively, as

$$T_{mn}=\frac{1}{U_{mn}}\int_{-\infty}^{\infty}t_m|q_{mn}|^2dt_m \quad (4\text{-}17)$$

1. Typically average dispersion of the dispersion map.
2. See Chapter 2, p. 13 for details.

$$\Omega_{mn} = \frac{1}{U_{mn}} \int_{-\infty}^{\infty} Im\left(\frac{\partial q_{mn}}{\partial t_m} q_{mn}^*\right) dt_m \tag{4-18}$$

where $U_{mn} = \int_{-\infty}^{\infty} |q_{mn}|^2 dt_m$ is the energy of the n-th pulse in channel m,

$t_m = t - \int_0^z v_m^{-1}(z_1) dz_1$ is the retarded time of channel m.

Ignoring pulse spreading outside the bit interval, integration of Eq. (4-17) needs to be performed over only a single bit. Differentiating T_{mn} and Ω_{mn} with respect to z and using Eq. (4-16) one obtains the following dynamic equations for central time and frequency

$$\frac{d}{dz} T_{mn} = D_m \Omega_{mn} \tag{4-19}$$

$$\frac{d}{dz} \Omega_{mn} = \frac{2}{U_{mn}} \sum_{\substack{k \\ k \neq m}} \sum_{l} \int_{-\infty}^{\infty} |q_{mn}|^2 \frac{\partial}{\partial T} |q_{kl}(z, T + \theta_{mn,kl})|^2 dT \tag{4-20}$$

where $\theta_{mn,kl} = \int_0^z [v_m^{-1}(z_1) - v_k^{-1}(z_1)] dz_1 + (T_{mn} - T_{kl})$ is the accumulated time offset between the n-th pulse in channel m and the l-th pulse in channel k at distance point z.

$T = t_m - T_{mn}$ denotes the time with respect to the center of the n-th pulse in channel m.

Interferences between adjacent pulses within each channel are neglected[1]. It is also assumed that all signal pulses within a channel have the same shape, though, the shape may differ over distance z from channel to channel. With these assumptions, one can write

$$q_{mn} = \alpha_{mn} q_m \tag{4-21}$$

where $q_m(z)$ is the average shape of signal pulses in channel m,

α_{mn} accounts for the randomness of the bit stream in channel m. It equals 1 for marks and 0 for spaces, where equal probabilities of marks and spaces are assumed.

1. Cases for which this assumption holds are outlined in Chapter 4, p. 47.

Typically, there is no significant change of pulse shape resulting from collisions in dispersion-managed WDM systems as the collision length, L_c, is much shorter than the nonlinear length, L_{NL}.[1] Thus, changes of pulse shape due to interchannel pulse collisions are neglected. This approximation is known as *elastic collision approximation* (ECA). Note, however, that pulse shape changes versus distance due to dispersion and SPM effects are considered.

Regarding the points above, formal solutions of Eq. (4-19) and Eq. (4-20) can be derived as

$$T_{mn}(z) = T_{mn}^0 + \int_0^z D_m(z_1)\Omega_{mn}(z_1)dz_1 \tag{4-22}$$

$$\Omega_{mn}(z) = 2\sum_{\substack{k \\ k\neq m}}\sum_{l}\alpha_{kl}\int_0^z \frac{\Psi_{mn,kl}(z_1)}{U_m(z_1)}dz_1 \tag{4-23}$$

where T_{mn}^0 is the initial central time of the n-th pulse in channel m,

$\Psi_{mn,kl}(z) = \int_{-\infty}^{\infty}\left|q_m(z,T)\right|^2\frac{\partial}{\partial T}\left|q_k(z,T+\theta_{mn,kl})\right|^2 dT$ describes the frequency shift due to collision between the n-th pulse in channel m with the l-th pulse in channel k per distance.

Substituting Ω_{mn} from Eq. (4-23) into Eq. (4-22) yields the deviation from the initial central time at distance point z of the n-th pulse in channel m,

$$\begin{aligned}\Delta T_{mn} &= T_{mn} - T_{mn}^0 \\ &= 2\int_0^z D_m(z_1)\int_0^{z_1}\frac{1}{U_m(z_2)}\sum_{\substack{k \\ k\neq m}}\sum_{l}\alpha_{kl}\Psi_{mn,kl}(\alpha_{kl},z_2)dz_2dz_1 .\end{aligned} \tag{4-24}$$

ΔT_{mn} is a random variable as it depends on α_{kl}, which accounts for the randomness of transmitted bit streams in neighboring channels.

Statistics of random pulse position fluctuations are typically described by their first two moments only, assuming Gaussian statistics[2]. The average

1. See Chapter 2, p. 19 for definitions.
2. A reasonable assumption, as outlined in Chapter 6, p. 109.

deviation μ_m and deviation variance $\sigma^2_{t,\,m}$ of the initial pulse central time in channel m are defined as [141]

$$\mu_{t,\,m} = \langle \Delta T_{mn} \rangle = \frac{1}{N} \sum_{n=1}^{N} \Delta T_{mn} \tag{4-25}$$

$$\sigma^2_{t,\,m} = \langle \Delta T^2_{mn} \rangle - \langle \Delta T_{mn} \rangle^2 = \frac{1}{N} \sum_{n=1}^{N} (\Delta T_{mn})^2 - \mu^2_{t,\,m} \tag{4-26}$$

where the summation is performed over a combination of a large number of pulses N.

In the following section, the average deviation $\mu_{t,\,m}$ and secondly, the variance of the pulse central time $\sigma^2_{t,\,m}$ for channel m will be derived.

Average central time

After substituting Eq. (4-24) into Eq. (4-25) and taking the average, one finds that

$$\mu_{t,\,m} = \int_0^z D_m(z_1) \left\{ \int_0^{z_1} \frac{Q_m(z_2)}{U_m(z_2)} dz_2 \right\} dz_1 \tag{4-27}$$

where

$$Q_m(z) = 2 \sum_{\substack{k \\ k \neq m}} \sum_{l} \langle \alpha_{kl} \Psi_{mn,\,kl}(\alpha_{kl}, z_2) \rangle \tag{4-28}$$

with $\langle x \rangle$ denoting the average over all n.

In the following, it is assumed that a pulse in channel m interacts at an arbitrary instance of time only with *one* pulse in channel k. That is, pulses are separable during transmission, i.e., pulse broadening due to dispersion does not introduce intersymbol interferences. This separation of collisions becomes invalid when RZ pulses expand beyond the limits of the bit duration. However, it is shown in Chapter 5, p. 86 that this restriction can be relaxed. In fact, it should be reformulated to be: Contribution to accumulated pulse central time deviations due to the collision between a pulse in channel m with the distant pulses in channel k can be neglected. Note, however, that

all possible interactions where only one pulse per channel is taking part are considered.

Fixing k in the sum of Eq. (4-28) and selecting for each n-th bit in channel m only the term $l = n + J_{mk}$ that corresponds to the nearest bit in channel k, Eq. (4-28) becomes

$$Q_m(z) = \sum_{\substack{k \\ k \neq m}} \langle \Psi_{m,\, n;k,\, n+J_{mk}}(\theta_{mk} + \Delta\theta_{m,\, n;k,\, n+J_{mk}}, z) \rangle \tag{4-29}$$

where $\langle x \rangle$ means averaging over all n for which $\alpha_{k,\, n+J_{mk}} = 1$,

$\theta_{mk} = \int_0^z [v_m^{-1}(z_1) - v_k^{-1}(z_1)]dz_1$ is the accumulated time offset between channel m and k due to dispersion,

$\Delta\theta_{m,\, n;k,\, n+J_{mk}} = (\Delta T_{m,\, n} - \mu_m) - (\Delta T_{k,\, n+J_{mk}} - \mu_k)$ is the difference of deviations from the pulse central times between the n-th pulse in channel m and its nearest pulse in channel k,

J_{mk} denotes the differential time delay between the closest bits in channel m and k, normalized to the bit duration (defined further down).

Expanding $\Psi_{m,\, n;k,\, n+J_{mk}}$ in Eq. (4-29) into a Taylor series with respect to $\Delta\theta_{m,\, n;k,\, n+J_{mk}}$ around 0, averaging, and taking into account the symmetry consideration $\langle \Delta\theta \rangle = \langle (\Delta\theta)^3 \rangle$, one obtains that up to small corrections of the order of $O(\langle \Delta\theta \rangle^4)$, $Q_m(z)$ can be written as

$$Q_m(z) = \sum_{\substack{k \\ k \neq m}} \left\{ \Psi_{mk}[\Theta_{mk}(z), z] + \frac{1}{2} \frac{\partial^2}{\partial \Theta_{mk}^2} \Psi_{mk}[\Theta_{mk}(z), z](\sigma_{t,\, m}^2 - \sigma_{t,\, k}^2) \right\} \tag{4-30}$$

$$\text{with} \qquad \Psi_{mk}[\Theta_{mk}(z), z] = \int_{-\infty}^{\infty} \left| q_m(z, T) \right|^2 \cdot \frac{\partial}{\partial T} \left| q_k[z, T + \Theta_{mk}(z)] \right|^2 dT \tag{4-31}$$

where $\Theta_{mk}(z) = \tau_{mk}(z) - J_{mk}(z) T_b$ is the relative time delay of a pulse in channel k compared to the closest pulse in channel m,

$\tau_{mk}(z) = \int_0^z [v_m^{-1}(z_1) - v_k^{-1}(z_1)]dz_1 + (T_m^0 - T_k^0) + (\mu_{t,\, m} - \mu_{t,\, k})$ is the differential time delay of channel k relative to channel m,

$J_{mk}(z) = \text{floor}\left(\frac{\tau_{mk}(z)}{T_b}\right)$ is the maximum number of completed bit durations within τ_{mk},

T_i^0 is the initial time delay in channel i.

The three contributions to τ_{mk} account for the dispersion-induced timing difference, the initial pulse position difference, and the average position deviation due to collisions. Figure 4-6 shows a schematic diagram of the functions $\tau_{mk}(z)$ and $J_{mk}(z)$ versus distance.

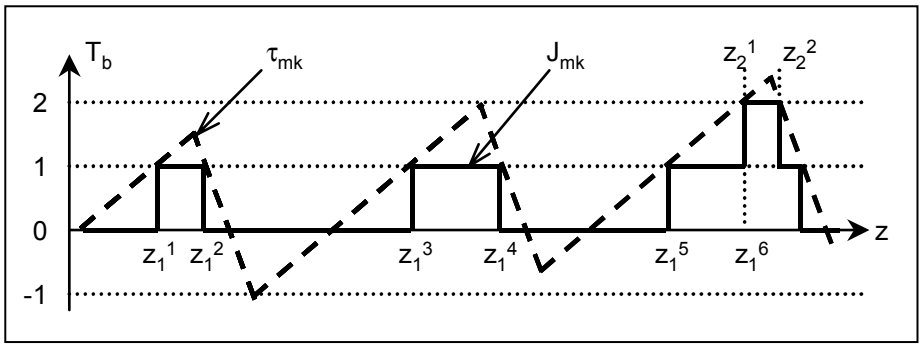

Figure 4-6. *Schematic plot of τ_{mk}, dashed line, and J_{mk}, solid line, between channel m and k in multiples of bit duration versus distance. $(z^l_{J(m,k)}, z^{l+1}_{J(m,k)})$ are distance intervals of single bit crossings.*

Note that the contribution of the second term on the right-hand side of Eq. (4-30) is typically small, as:

- For adjacent channels k, $\sigma^2_{t,m}$ is close to $\sigma^2_{t,k}$, so that $\sigma^2_{t,m} - \sigma^2_{t,k}$ is small.
- For distant channels k, $\sigma^2_{t,m} - \sigma^2_{t,k}$ is not small. However, their impact on CITJ can be assumed to be small as large walk-off due to dispersion implies short distances of pulse interactions.

Thus, the second term on the right-hand side of Eq. (4-30) can be neglected, and one obtains from Eq. (4-27) the following equation for the central time average

$$\mu_{t,\,m} = \sum_{\substack{k \\ k \neq m}} \int_0^z D_m(z_1)\left\{\int_0^{z_1} \frac{\Psi_{mk}[\Theta_{mk}(z_2), z_2]}{U_m(z_2)} dz_2\right\} dz_1 \tag{4-32}$$

where Ψ_{mk} is given by Eq. (4-31).

Eq. (4-32) can be understood as follows: Ψ_{mk} accounts for the strength of a collision between a pulse traveling in channel m with its closest pulse traveling in channel k at a distance z_2. After weighting by the local pulse energy U_m, integration over distance is performed. The accumulated frequency shift is then multiplied with the local dispersion D_m to give the local timing shift. All time shifts are accumulated over distance via integration. Finally, summation over all neighboring channels k of channel m is performed.

Central time variance

In the previous paragraph, an expression was derived for the average pulse deviation $\langle \Delta T_{mn} \rangle$. So to determine $\sigma^2_{t,\,m}$, only $\langle \Delta T^2_{mn} \rangle$ needs to be found. From Eq. (4-24) one can derive that

$$\langle \Delta T^2_{mn} \rangle = \int_0^z \int_0^z D_m(z_1) D_m(z_2) \left\{\int_0^{z_1} \int_0^{z_2} \frac{\Phi_m(z_3, z_4)}{U_m(z_3) U_m(z_4)} dz_4 dz_3\right\} dz_2 dz_1 \tag{4-33}$$

where $\Phi_m(z_1, z_2) = 4 \sum_{\substack{k \\ k \neq m}} \sum_{l} \sum_{\substack{k' \\ k' \neq m}} \sum_{l'} \langle \alpha_{kl} \alpha_{k'l'} \Psi_{mn,\,kl}(z_1) \Psi_{mn,\,k'l'}(z_2) \rangle$

with $\langle x \rangle$ denoting the average over all n.

As mentioned before, only single pulse collisions with the closest pulses in neighboring channels are considered for each distance point. Thus, it is sufficient to choose for the n-th pulse only the terms $l = n + J_{mk}$ and $l' = n + J_{mk}$. Also, using the assumption that marks and spaces in different channels are mutually independent, one can show that the term $\Phi_m(z_1, z_2)$ evaluates to [61]

$$\Phi_m(z_1, z_2) = \sum_{\substack{k \\ k \neq m}} \sum_{\substack{k' \\ k' \neq m}} \Psi_{mk}[\Theta_{mk}(z_1), z_1]\Psi_{mk'}[\Theta_{mk'}(z_2), z_2] + \delta[J_{mk}(z_1), J_{mk}(z_2)] \sum_{\substack{k \\ k \neq m}} \Psi_{mk}[\Theta_{mk}(z_1), z_1]\Psi_{mk}[\Theta_{mk}(z_2), z_2] \tag{4-34}$$

where Ψ_{mk} is defined by Eq. (4-31),

$\delta(x, y)$ is the discrete Dirac-delta function.

Substituting Eq. (4-34) into Eq. (4-33), extracting $\mu_{t,m}^2$ defined by Eq. (4-27), and integrating in Eq. (4-33) by parts one obtains

$$\sigma_{t,m}^2 = \sum_{\substack{k \\ k \neq m}} \int_0^z \int_0^z \frac{\overline{D}_m(z_1)\overline{D}_m(z_2)}{U_m(z_1)U_m(z_2)} \times \delta[J_{mk}(z_1), J_{mk}(z_2)]\Psi_{mk}[\Theta_{mk}(z_1), z_1]\Psi_{mk}[\Theta_{mk}(z_2), z_2]dz_1dz_2 \tag{4-35}$$

where $\overline{D}_m(z_i) = \int_{z_i}^{z} D_m(\tilde{z})d\tilde{z}$ is the accumulated dispersion of channel m between distance z_i and z.

In dispersion-managed fiber links, local dispersion values are typically much larger than the average dispersion over the dispersion map. Since the propagation velocity is determined by the local dispersion values, a pulse in channel m might experience multiple collisions with another pulse in channel k. It is important to collect these collisions separately for each pulse as their occurrences are correlated. This is depicted in Figure 4-7. Assuming low average time delay differences due to collisions, the distance at which these collisions occur can be determined.

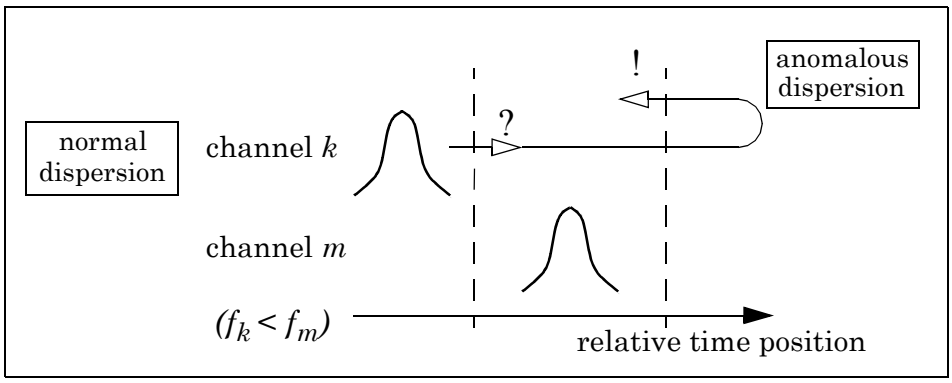

Figure 4-7. *Two pulses can collide more than once because their relative speeds depend on local dispersion.*

Thus, the whole propagation distance can be expressed as a sum of the bit crossing distance intervals where collisions between signal pulses in channels m and k occur. Collisions occurring between the same pair of pulses are grouped. So, each of the integrals in Eq. (4-35) can be represented as

$$\int_0^z dx = \sum_{J_{mk}} \left(\sum_l \int_{z^l_{J(m,k)}}^{z^{l+1}_{J(m,k)}} dx \right) \tag{4-36}$$

where $(z^l_{J(m,k)}, z^{l+1}_{J(m,k)})$, with $l = 2j+1$ and $j = 0, 1, 2, \ldots$ are the bit crossing distance intervals in which the differential time delay between channel m and k, τ_{mk}, falls within the J_{mk}-th bit (see Figure 4-6).

Substituting Eq. (4-36) into Eq. (4-35) and keeping only the terms with $J_{mk}(z_1) = J_{mk}(z_2)$ one finally obtains the following formula for the central time variance,

$$\sigma^2_{t,m} = \sum_{\substack{k \\ k \neq m}} \sum_{J_{mk}} \left\{ \sum_l \int_{z^l_{J(m,k)}}^{z^{l+1}_{J(m,k)}} \frac{\overline{D}_m(z_1)}{\overline{U}_m(z_1)} \Psi_{mk}[\Theta_{mk}(z_1), z_1] dz_1 \right\}^2 \tag{4-37}$$

where the summation with respect to l is taken over $l = 2j+1$ with $j = 0, 1, 2, \ldots$, while the summation with respect to J_{mk} is taken over $J_{mk} = 0, \pm 1, \pm 2, \pm 3, \ldots$.

Eq. (4-37) can be understood as follows. The strength of collision Ψ_{mk} between pulses in channels m and k is weighted by the local pulse energy U_m, and the accumulated dispersion $\overline{D}_m$ between position z_1 (where the collision is evaluated) and z (the final destination of pulse propagation). Integration over the bit crossing distance interval $(z^{l}_{J(m,k)}, z^{l+1}_{J(m,k)})$, gives a normalized value for the time position deviation of a single collision between channels m and k. Then, a summation of all l collisions between the same pulses is performed. After squaring, the final summation is performed over all possible distance intervals J_{mk} between channels m and k, and over all neighboring channels k of channel m.

4.4.2.2 Numerical implementation

Eq. (4-32) and Eq. (4-37) give a complete set of equations for determining the average and variance of the pulse central time. In order to calculate CITJ using Eq. (4-32) and Eq. (4-37), the following procedure needs to be followed.

1. Calculate the propagation of the pulse shape q by numerically solving the GNLS given in Eq. (2-19) for one signal pulse per channel. Considering no dependence between the influences of ASE-noise and interchannel pulse collisions, ideal lumped amplifiers are assumed along the fiber.[1]
2. Substitute the calculated pulse shape q into Eq. (4-31) and calculate the collision integral Ψ_{mk} for each m.
3. Substitute Ψ_{mk} and the local pulse energy U_m into Eq. (4-32) and calculate the average of the pulse central time $\mu_{t,m}$ for each channel by numerical integration.
4. Finally, after substituting Ψ_{mk}, U_m, and μ_m into Eq. (4-37), and applying a simple numerical algorithm for calculating the sum of integrals over the bit crossing distance intervals $(z^{l}_{J(m,k)}, z^{l+1}_{J(m,k)})$ as defined in Eq. (4-36), the variance of the pulse central time $\sigma^2_{t,m}$ is evaluated.

1. The impact of ASE-noise induced timing jitter can be estimated using linearization approximation as derived in Chapter 4, p. 51.

This model is implemented in an iterative algorithm, where steps 2., 3., and 4. of the procedure are performed after each split-step applied to solve the GNLS.

The calculation of CITJ is very sensitive to the precise capturing of local propagation characteristics of the signal pulses. Thus, it is important to choose the step-sizes such that a certain dispersion-length product per step is not exceeded. In estimating pulse width changes for the linear case, the graph shown in Figure 4-8 depicts the dependence of convergence on the minimum number of calculation steps per fiber span for various dispersion-length-products. The figure is plotted for the case that the maximum change of pulse width per step does not exceed $\Delta\tau = 0.075$ ps.

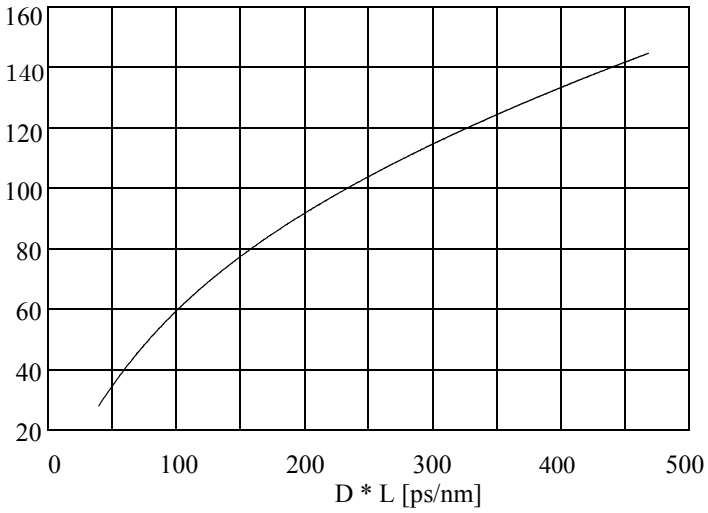

Figure 4-8. *Minimum number of split-steps per fiber span versus dispersion-length-product.*

The main advantage of the presented algorithm is that it reduces drastically the computational effort compared to full numerical simulations mainly due to two factors.

1. It is not necessary to process the frequency bandwidth of the whole WDM signal comb, but only the bandwidth of a single channel. However, the time resolution should stay reasonably large to be able to model rapid pulse shape changes.

2. It is not necessary to simulate the propagation of a long stream of pseudo-random bits in order to find numerical estimates of the central time variance. Instead, propagation of only one mark per channel is simulated.

In particular the second factor allows for reduction of computational effort by two orders of magnitude compared to a full numerical simulation.

4.4.2.3 Validation

In order to validate the elastic collision approximation (ECA) method, it is compared with full numerical simulations of several typical WDM systems. One comparison is presented here, while others are given throughout Chapter 5.

The first scenario under consideration is a 10-channel WDM system with 10 Gbit/s bitrate per channel and 100 GHz channel spacing. Table 4-2 lists the parameters of the dispersion map including amplifier positioning.

Table 4-2. *Parameters of dispersion map B.*

L_1	95.6	km	D_1	4.0	ps/nm-km
L_2	4.4	km	D_2	-85.0	ps/nm-km
L_{launch}	47.8	km			
L_A	50.0	km			

Figure 4-9 illustrates graphically the meaning of the parameters listed in Table 4-2. The dispersion map consists of a span of anomalous NZDSF with dispersion D_1 and length L_1, and a span of DCF with dispersion D_2 and length L_2.[1] The amplifier spacing is L_A; they are placed at the midpoints of each span. The pulses are launched in each channel from the middle of the anomalous dispersion span.

1. The dispersion slope parameters S1, and S2 are set, such that the slope of the chromatic dispersion vanishes. See Chapter 2, p. 9 for details.

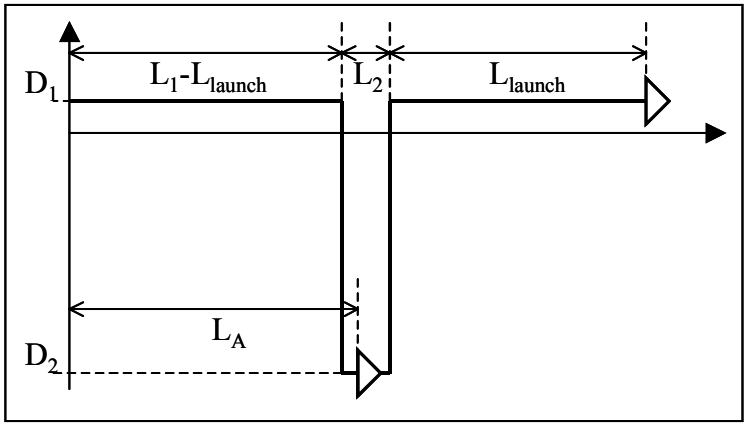

Figure 4-9. *Schematic of dispersion map B.*

Figure 4-10 presents results of comparison for an initial time shift of pulses in neighboring channels of 50 ps. The peak power of the initially Gaussian pulses is 3.13 mW, the FWHM duration is set to 16.74 ps.[1] As seen in Figure 4-10 the middle channel experiences a larger accumulation of timing jitter compared to the outer channel. This can be explained by the larger number of close neighbors the middle channel sees compared to the outer one. Thus, it experiences more collisions with slowly moving neighboring channels. The outermost channels 1 and 10 experience the same timing jitter, the values for all intermediate channels lie in between the timing jitter of channel 5 and 10. Figure 4-10 shows good agreement between the elastic collision approximation (ECA) method and full numerical simulations.

1. Pulse width and peak power are selected such that they define a pulse, which is similar in energy and width to a DMS solution for the given dispersion map.

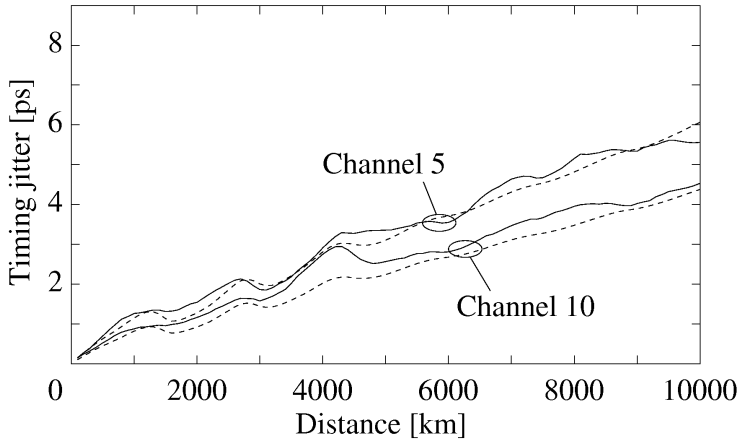

Figure 4-10. *CITJ versus distance for the middle (m = 5) and outer (m = 10) channel in a 10 channel system. Results of the ECA method (dashed line) are compared with results using full numerical simulations (solid line). Dispersion map B was applied (see Table 4-2) [61].*

In summary, a semi-analytical model has been presented that allows creation of an efficient algorithm for the accurate estimation of XPM-induced timing jitter in WDM systems applying arbitrary RZ pulse shapes. The computational effort is reduced by two orders of magnitude, as the functional dependence of CITJ on the shape of the signal pulses is derived analytically. Example results agree well with reference data gathered from full numerical simulations. Additional validations and detailed application examples evaluating the dependence of CITJ on different system parameters are presented in Chapter 5.

Chapter 5

WDM system simulations - timing jitter

5.1 Overview

Various results of system simulations are presented in this chapter. Firstly, ASE-noise induced timing jitter (ANTJ) is investigated. During the first part of this chapter, it is shown that ANTJ depends strongly on the dispersion map and the amplifier positioning. As there is already a numerous amount of literature published on this topic, their findings are briefly discussed and summarized here.

In the following part, the accumulation of XPM-induced timing jitter[1] in dispersion-managed WDM transmission systems is investigated. It will be shown that CITJ depends strongly on the average dispersion, channel spacing and number of channels interacting nonlinearly during propagation. Additionally, it is shown that initial pulse positioning in the bit interval plays a crucial role on the accumulation of XPM-induced timing jitter.

Most simulations were performed using the VPIsystems product *VPItransmissionMaker™ WDM*, and its predecessor *Photonic Transmission Design Suite™*, which are both synthesis and analysis tools to explore WDM system and link designs [153]. They apply diverse types of signal representations, which allow discrimination throughout the fiber transmission between data signals, optical noise and crosstalk signals [101]. The two semi-analyti-

1. Also noted as collision-induced timing jitter (CITJ).

cal algorithms for estimating ANTJ and CITJ[1] have been incorporated in the tools. They are part of today's standard releases, frequently undergoing rigorous validation tests. However, there exist some additional features, which are not part of the commercial release yet. Unless otherwise stated, idealized transmitter and receiver models are applied, as their distortions are of negligible influence or of no importance to the discussed subjects. Several, mainly post-processing tasks, have been performed using MATLAB®.

5.2 ANTJ in dispersion-managed systems

In this section, results of system simulations estimating ASE-noise induced timing jitter are presented.

Consider Eq. (4-12), which describes the three contributions to ASE-noise induced timing jitter. They are mainly determined by the local pulse power and shape $|q(z,t)|$, as well as the accumulated dispersion from the point where noise is added to the point of final destination. Thus, ANTJ is strongly influenced by the applied dispersion map and the amplifier positioning inside the dispersion map. These influences are investigated in this section.

Firstly, the dependence of dispersion and amplifier spacing is investigated for classical soliton systems. Figure 5-1 shows simulation results of ANTJ versus distance for six different cases of soliton systems. The upper group of curves represents a set of cases, where the dispersion is set to D = 1.0 ps/nm-km, whereas the lower group of curves represents results for D = 0.078 ps/nm-km. The three curves for each set are gathered for three different amplifier spacings, namely L_A = 1 km, 20 km and 50 km. The curve L_A = 1 km corresponds to the case of distributed amplification and serves as reference. A noise figure of 4 dB of the amplifiers is assumed for all the cases.

1. See Chapter 4, p. 51, Chapter 4, p. 59 for details.

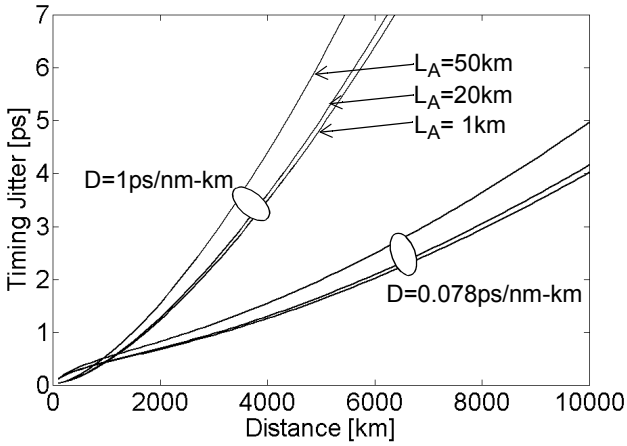

Figure 5-1. *ANTJ versus distance for two different dispersion values and three different amplifier spacings, NF = 4 dB.*

Figure 5-1 shows that ANTJ is growing with increased amplifier spacing. This is mainly due to the fact that the ratio between amplifier spacing L_A and effective fiber length L_{eff} is growing with increased amplifier spacing. Hence, the power enhancement of solitons in the average soliton regime[1] is raising.

A second study is performed on the dependence of ANTJ accumulation on the dispersion map. For this, the results of a soliton system are compared with a dispersion-managed soliton (DMS) system. It is important to select carefully the values for pulse widths and peak powers in order to be able to compare the behavior of both systems. The FWHM duration is 20 ps for the soliton, and 16.74 ps for the DMS. The durations are set such that both pulses have the same energy. The dispersion of the soliton system is D = 0.078 ps/nm-km. This corresponds to the average dispersion of the DMS system. See Table 4-1 for details on the dispersion map A, which is applied here again [132]. The amplifier spacing is set to L_A = 50 km.

Figure 5-2 shows the results of three different scenarios. Curve A refers to the results for the average soliton system with L_A = 50 km. Curves B_1 and B_2 refer to the results of the DMS system. B_1 shows ANTJ after each amplifier, whereas B_2 shows ANTJ after each dispersion map only. For comparison, curve C shows the accumulated timing jitter for the equivalent soliton sys-

1. See Chapter 3, p. 35 for details.

tem with distributed amplification[1]. Figure 5-2 (a) shows the accumulated ANTJ values for the case that amplifiers have a noise figure of 4 dB, and Figure 5-2 (b) for the case that they have a noise figure of 6 dB.

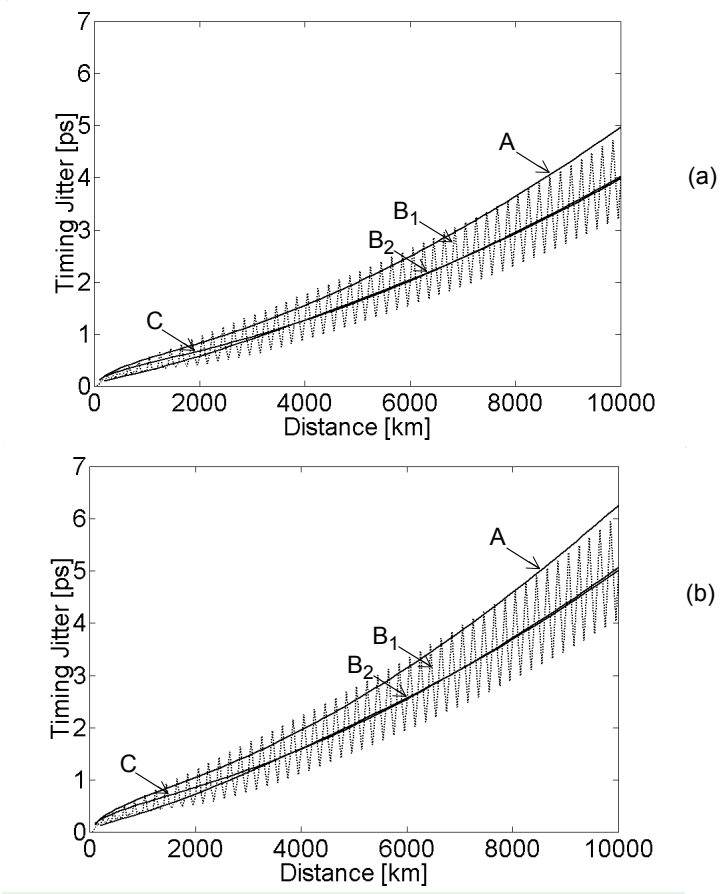

Figure 5-2. *ANTJ versus distance for different dispersion maps, A: average soliton system with L_A = 50 km, B: DMS system (see Table 4-1), snap shots after each amplifier (B_1), and after each dispersion map (B_2), C: soliton system, distributed amplification; (a) NF = 4 dB, (b) NF = 6 dB.*

As shown in Figure 5-2, the dispersion-management of the DMS system reduces the accumulated ANTJ by an amount of 20% (curve B_2 is below curve A by approximately this amount). This is mainly due to the power enhancement of the DMS system compared to the soliton system[2]. While the accumulation of ANTJ inside the dispersion map of the DMS system is rap-

1. Distributed amplification is modeled by placing an amplifier every one kilometer.
2. See Chapter 3, p. 37 for details.

idly changing (curve B_1), it is comparable in average to the soliton system with distributed amplification (curve B_2 is almost matching curve C). The increase of the noise figure from 4 dB to 6 dB yields also an 20% increase in ANTJ (compare results of Figure 5-2 (a) and (b)).

5.3 CITJ in WDM transmission systems

In this section, results of various system simulations estimating XPM-induced timing jitter are presented.

Consider Eq. (4-31), which describes the collision-integral defining the strength of the collision between a pulse in channel m with its closest pulse in channel k at a certain distance point. The collision-integral is mainly determined by the local pulse power and shape $|q_m(z, T)|$, and the local overlap of the colliding pulses, given by the relative time delay of both pulses $\Theta_{mk}(z)$. As outlined in Chapter 4, p. 66, there are three contributions to Θ_{mk} accounting for the dispersion-induced timing difference, the initial pulse position difference, and the average position deviation due to collisions. Since the third contribution is usually small, Θ_{mk} is strongly influenced by the applied dispersion map and the initial settings of the pulses inside the bit interval. The pulse power and shape are determined by the amplifier positioning inside the dispersion map. The following system design parameters are investigated:

- dispersion map
- amplifier positioning
- dispersion slope
- RZ modulation scheme
- channel spacing
- initial pulse positioning.

5.3.1 Dependence of CITJ on dispersion map and amplifier positioning

XPM-induced timing jitter varies for different WDM channels even when each channel is experiencing the same dispersion. Firstly, systems with a zero dispersion slope are investigated to evaluate this difference in timing jitter. The impact of dispersion slope on the accumulation of XPM-induced timing jitter will be investigated in Chapter 5, p. 85.

The growth of CITJ with distance is not a monotonous function as shown in Figure 4-10. There are distinctly observable humps, which are periodically spaced. For this example, these humps are clearly visible up to 6,000 km, after this they start to degrade. The analysis of several other dispersion maps later in this chapter shows that the period of these humps L_h is proportional to the bit passing distance for neighboring channels with respect to average dispersion, i.e.,

$$L_h = \frac{T_b}{D_{ave}\Delta\lambda_{mk}} \tag{5-1}$$

where T_b is the bit duration, $\Delta\lambda_{mk}$ is the spacing between channel m and k,

D_{ave} is the average dispersion of the dispersion map.

In the case of Figure 4-10, L_h is calculated to be 1,488 km. It follows from Eq. (5-1) that the period of humps will scale in inverse proportion to the average dispersion for different dispersion maps and equal channel spacing.

Eq. (5-1) is validated by using two other examples of a 10 channel x 10 Gbit/s system illustrated in Figure 5-3 and Figure 5-4. The dispersion map for both graphs in Figure 5-3 is described in Table 5-1.

Table 5-1. *Parameters of dispersion map C.*

L_1	93.0	km	D_1	3.0	ps/nm-km
L_2	7.0	km	D_2	-38.74	ps/nm-km
L_{launch}	46.5	km			
L_A	50.0	km			

The peak power of the initially Gaussian-shaped pulses was 2.9 mW. The FWHM duration was set to 16.75 ps; no additional chirp was applied. Note that the pulse width and peak power are selected such that they define a

pulse, which is similar in energy and width to a DMS solution for the given dispersion map. The initial time shift of pulses in neighboring channels was 50 ps to reduce the effects from initial pulse overlaps[1]. The channel spacing is 100 GHz (Figure 5-3 (a)) and 75 GHz (Figure 5-3 (b)). Amplifiers are located at the midpoints of the normal and anomalous spans [132].

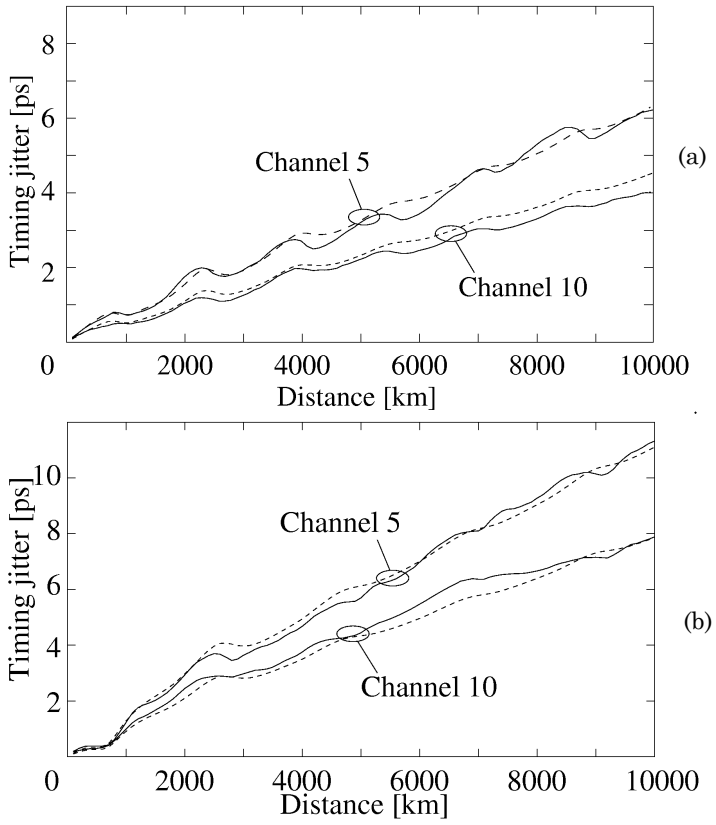

Figure 5-3. *CITJ versus distance for the middle (m = 5) and outer (m = 10) channel in a 10 channel system. Results of the ECA method (dashed line) are compared with results using full numerical simulations (solid line). Dispersion map C was applied (see Table 5-1). Channel spacing was (a) 100 GHz [59], (b) 75 GHz [61].*

Figure 5-3 shows that the accumulated timing jitter is almost twice as large for 75 GHz channel spacing than it is for 100 GHz channel spacing. Using Eq. (5-1), the period of humps is calculated to be approximately $L_h = 1{,}600$ km for 100 GHz channel spacing and approximately

1. See Chapter 5, p. 92 for details on the influence of initial pulse positioning.

L_h = 2,133 km for 75 GHz channel spacing. Both values agree well with results presented in Figure 5-3.

In Figure 5-4 results for the dispersion map A are shown, which has already been introduced in Chapter 4, p. 57. The parameters of this dispersion map are listed in Table 4-1. The channel spacing was 75 GHz as in the lower graph of Figure 5-3. The peak power of the initially Gaussian pulses was 2.8 mW, the initial time shift of pulses in the neighboring channels was 50 ps.

The calculated period of humps is L_h = 2,133 km, as in Figure 5-3 for 75 GHz channel spacing. Note that the local dispersion values of the dispersion maps B and C are very different, which results in considerably different pulse dynamics along the map. However, the average dispersion in Figure 5-3 and Figure 5-4 is the same. It is remarkable that the accumulated timing jitter values match as well, suggesting that CITJ is mainly determined by the average dispersion and channel spacing for these DMS scenarios.

Note that in all the three cases presented in Figure 5-3 and Figure 5-4 the calculated period of humps agrees well with the results using full numerical simulations up to 5000 km. For larger distances there is some discrepancy between the curves, however, the agreement remains reasonably good.

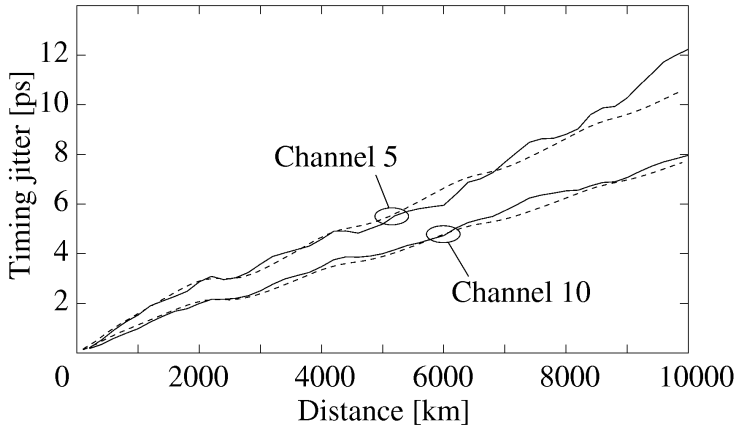

Figure 5-4. *CITJ versus distance for the middle (m = 5) and outer (m = 10) channel in a 10 channel system. Results of the ECA method (dashed line) are compared with results using full numerical simulations (solid line). Dispersion map A was applied (see Table 4-1). Channel spacing was 75 GHz [131].*

5.3.2 Dependence of CITJ on dispersion slope

Up to this point, the dispersion slope S was set such that the slope of GVD becomes zero[1]. This is a reasonable assumption for higher order dispersion management (HODM), as employed in modern long-haul transmission systems (see Table 1-1). The influence of the dispersion slope is analyzed in the next example for the case that no HODM is applied. The considered dispersion map is very similar to the dispersion map A described in Table 4-1. So the results presented in this section are comparable with the results presented in Figure 4-10 already. Only that now, a non-zero dispersion slope was considered. The dispersion map parameters are presented in Table 5-2.

Table 5-2. *Parameters of dispersion map D.*

L_1	95.66	km	D_1	4.0	ps/nm-km
			S_1	0.04	ps/nm^2-km
L_2	4.34	km	D_2	-85.0	ps/nm-km
			S_2	-0.2	ps/nm^2-km
L_{launch}	47.83	km			
L_A	50.0	km			

The channel spacing is 100 GHz. The initial time shift of neighboring channels was 50 ps. The FWHM duration of the Gaussian pulses at the input was set to 16.74 ps. Due to the non-zero slope of the GVD, channel 1 experiences an average dispersion of 0.244 ps/nm-km, while channel 10 experiences an average dispersion of only 0.03 ps/nm-km. To ensure stable pulse propagation for all the 10 channels, increased average dispersion can be compensated by an increased nonlinear phase shift, which arises for higher peak power values, as outlined in Chapter 3, p. 37. Thus, pulses are launched with different peak powers in different channels (see Table 5-3).

Table 5-3. *Peak power values of channel 1 to 10 at the input of the fiber.*

channel	1	2	3	4	5	6	7	8	9	10
P [mW]	8.0	7.2	6.4	5.6	4.8	4.0	3.3	2.5	1.7	1.0

1. With Eq. (2-6), this means that $S = -2D/\lambda$.

Figure 5-5 shows the resulting CITJ versus transmission distance. It is seen that the timing jitter in channel 1 is significantly larger than it is for channel 10. This is due to the fact that pulses in channel 1 experience a larger amount of XPM because of their enhanced peak power values. There is a good agreement of results obtained from the ECA method and from full numerical simulations for channels 1 and 10, and a reasonably good agreement for channel 6. Note that the humps are not visible in Figure 5-5 since the periodicity of bit passing distances is violated as different channels have different average dispersions.

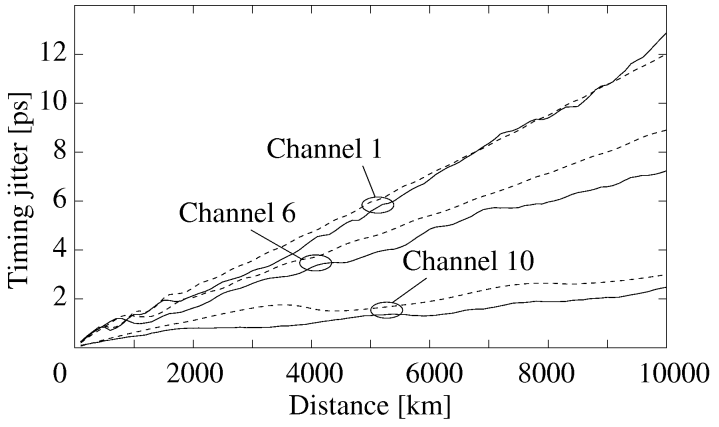

Figure 5-5. *CITJ versus distance for a system with non-zero dispersion slope. Results of the ECA method (dashed line) are compared with results using full numerical simulations (solid line). Dispersion map D was applied (see Table 5-2) [61].*

5.3.3 Dependence of CITJ on RZ modulation scheme

In all cases considered so far RZ pulses did not expand beyond their bit intervals. In the following, timing jitter in CRZ systems is investigated, where pulses spread over more than one bit duration[1]. When RZ pulses expand beyond their bit intervals, one would expect that pulse powers decrease, which reduces the effect of XPM, in turn suggesting that CITJ becomes insignificant. Hence, one can expect that the elastic collision

1. As introduced in Chapter 3, p. 41.

approximation (ECA) as presented in Chapter 4, p. 59 will still be valid for systems with large stretching factors.

In order to investigate the relevance of the ECA method for CRZ systems, CITJ is calculated for a 10-channel CRZ system with parameters similar to those in [20], [50]. The bitrate per channel was 10 Gbit/s; the FWHM pulse duration of the initially raised-cosine shaped pulses was 50 ps. The peak power was set to 0.6 mW; slight sinusoidal phase modulation of Δf_{max} = 18.5 GHz (m_p = 0.6) was applied. The dispersion map is described in Table 5-4.

Table 5-4. *Parameters of dispersion map E.*

L_1	450.0	km	D_1	-2.0	ps/nm-km
L_2	45.0	km	D_2	19.8	ps/nm-km
L_{launch}	225.0	km			
L_A	45.0	km			

Figure 5-6 shows pulse evolution over a single dispersion map length of 495 km [133]. Snap shots were taken every 45 km, right after the inline amplifiers. The pulse spreading is clearly visible. It can be seen that pulses widen over the two neighboring bit intervals at their maximum, and shrink to a fraction of their original width developing very large local peak powers of about three times the initial peak power. At the end of each span, pulses are back to their original shape. Isolated marks do not suffer significantly from intersymbol interferences. Streams of marks, however, develop large ghost pulses right at the edges of the bit interval.

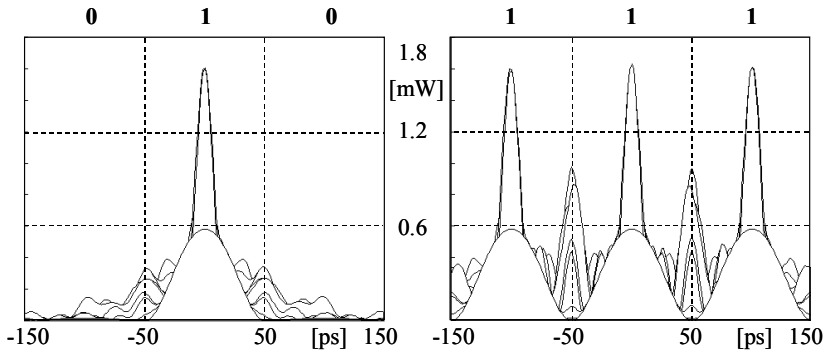

Figure 5-6. *Pulse evolution over one dispersion map length for an isolated mark (left) and a stream of marks (right), snap shots were taken after each amplifier (every 45 km).*

Figure 5-7 compares CITJ results from the ECA method with data from full numerical simulations versus distance. Timing jitter values of a middle channel are presented for 100 and 75 GHz channel spacing. For both cases, very good agreement is observed. Thus, the assumption made above holds – that when RZ pulses expand significantly, pulse peak powers decrease and XPM effects are reduced such that contributions of collisions between these pulses to accumulated CITJ is small. Consequently, the elastic collision approximation remains valid. Note that even the relatively large ghost pulses, which develop between neighboring marks during propagation, have no significant influence on accumulation of XPM-induced timing jitter.

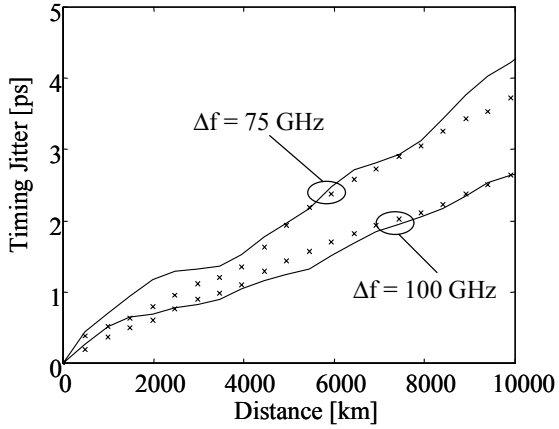

Figure 5-7. *CITJ versus distance. Results of the ECA method (solid line) are compared with results using full numerical simulations (crosses). Upper curve is for 75 GHz channel spacing, lower curve is for 100 GHz channel spacing. Dispersion map E was applied (see Table 5-4) [133].*

It is noticeable that the CRZ system is more robust against CITJ build up than the DMS systems analyzed so far. This is mainly due to the fact that in DMS systems, pulses maintain their pulse shape over the dispersion map, and thus, their relative large peak power values. In the CRZ system pulses spread drastically, and so, reduce their sensitivity to XPM effects.

5.3.4 Dependence of CITJ on channel spacing

It follows from Eq. (5-1) that the period of humps will scale in inverse proportion to channel spacing for different dispersion maps with the same average dispersion.

From soliton theory it is derived that the frequency shift of a two-soliton collision is inversely proportional to channel spacing [27]. This is intuitively clear as an increased frequency separation of the two colliding pulses reduces their nonlinear interaction length, i.e., the collision length L_c[1]. However, these results have been derived for transmission links with constant dispersion, where two pulses undergo only one collision with each other during propagation.

For DMS or other practical RZ modulation schemes employing dispersion management, two pulses undergo multiple collisions with each other. So a simple relation might not hold for them. In order to investigate the dependence of accumulated CITJ on channel spacing more closely, two previously discussed systems are investigated here again. These are the DMS system, which was studied in Chapter 5, p. 82 (dispersion map C), and the CRZ system, which was analyzed in Chapter 5, p. 87 (dispersion map E).

Figure 5-8 shows the XPM-induced timing jitter versus channel spacing at different distances for the DMS system. The CITJ is monotonically decreasing for increased channel spacing Δf with the following approximate relation

$$\sigma_t^2 \sim \frac{1}{\Delta f^3} \ . \tag{5-2}$$

The two dashed reference curves drawn in Figure 5-8 visualize this behavior.

1. For definition of L_c, see Chapter 2, p. 19.

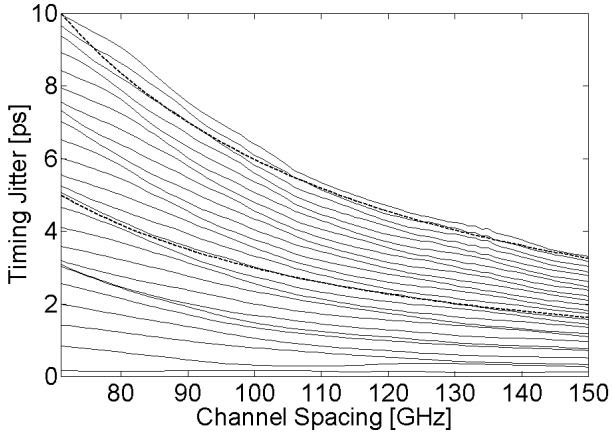

Figure 5-8. *CITJ versus channel spacing for different transmission distances, starting from the bottom curve, each curve represents an increase in distance of 400 km. Dispersion map C was applied (see Table 5-1).*

Figure 5-9 shows the XPM-induced timing jitter versus channel spacing at different distances for the CRZ system [133]. It is remarkable that CITJ is not monotonically decreasing with increased channel spacing. XPM-induced timing jitter seems to accumulate at certain channel spacings faster than at others. However, only small resonances are visible. In general, the variance of the pulse postion is approximately in inverse proportion to the third power of the channel spacing.

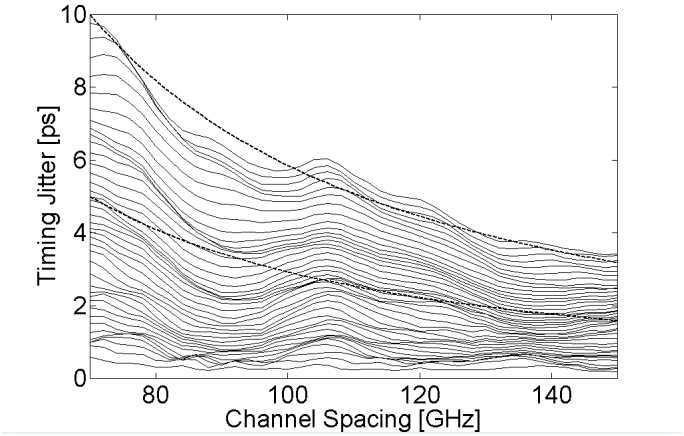

Figure 5-9. *CITJ versus channel spacing for different transmission distances, starting from the bottom curve, each curve represents an increase in distance of 495 km. Dispersion map E was applied (see Table 5-4).*

Resonances of the XPM efficiency versus channel spacing have also been observed experimentally [127]. For a two channel RZ system, the periodicity of such resonances could be related to the bit duration divided by the dispersion-length product of one amplifier span [42]:

$$\Delta\lambda_{kl} = \frac{T_b}{(LD)_{span}} \tag{5-3}$$

where $\Delta\lambda_{kl}$ is the channel spacing, T_b is the bit duration,

$(LD)_{span}$ is the dispersion-length product of the dominating span.

For channel spacings just falling on these points of resonance, XPM effects tend to add in a more coherent manner. For channel spacings just falling in the middle of these resonances, XPM effects add in a more incoherent manner.

However, the small resonances observed in Figure 5-9 can not be directly related to Eq. (5-3). The reason for this could be that in [42], separable pulse shapes are considered, whereas for the dispersion map considered here, pulses smear out rapidly over the complete bit duration.

In order to investigate the resonance behavior more closely, another dispersion map was investigated (see Table 5-5). This dispersion map applied the same initial pulse shape (CRZ) and power. However, its dispersion map incorporates more potential resonance distances.

Table 5-5. *Parameters of dispersion map F.*

L_1	243.0	km	D_1	4.1	ps/nm-km
L_2	27.0	km	D_2	-36.7	ps/nm-km
L_{launch}	108.0	km			
L_A	54.0	km			

Figure 5-10 shows the dependence of CITJ on channel spacing for different distances. It is remarkable to note that several clear resonances are observable in this case. Also, note that these resonances are dependent on the transmission distance, which is indicated by the lines in Figure 5-10. With increased distance (most upper curve corresponds to about 20,000 km) the resonances shift towards lower channel spacing, and move closer together. However, this trend is only visible after approximately 13,500 km. Before this, no real trend can be determined.

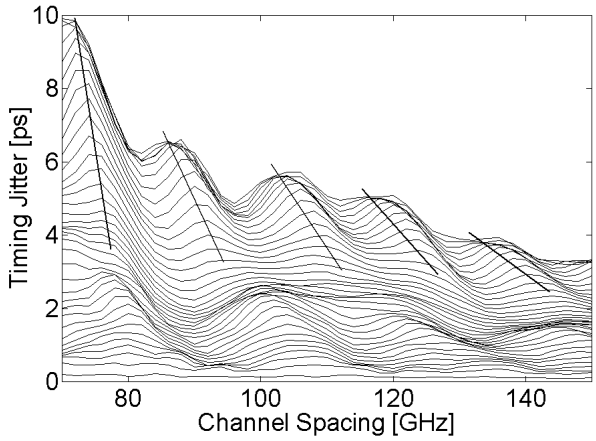

Figure 5-10. *CITJ versus channel spacing for different transmission distances, starting from the bottom curve, each curve represents an increase in distance of 540 km. Dispersion map F was applied (see Table 5-5).*

An important question to address is why is there such a big difference in CITJ dependence on channel spacing between Figure 5-9 and Figure 5-10. Both dispersion maps have approximately the same average dispersion. The main differences between both setups is the amplifier spacing (45 km versus 54 km) and the absolute value of accumulated dispersion per amplifier spacing (90 ps/nm versus 221.4 ps/nm). Additionally, dispersion map E (see Table 5-4) has the only resonance distance at L_A = 45 km, whereas dispersion map F (see Table 5-5) has several potential resonance distances: L_2 = 27 km, L_A = 54 km, L_1 = 273 km.

In summary, CITJ is in general decreasing with increased channel spacing according to Eq. (5-2). Slight to moderate resonances might be observable. The locations of these resonances depend on the periodic distances in the dispersion map, over which complete bit crossings could happen for certain channel spacings, leading to coherent addition of XPM effects.

5.3.5 Dependence of CITJ on initial pulse positioning in bit interval

It has been shown in [118] that the temporal overlap of pulses in different WDM channels at the input of the fibers causes unbalanced collisions, and thus, initial frequency shifts. Figure 5-11 shows the frequency shift due to

the collision of two solitons in a lossless fiber versus distance [118]. The channel spacing of the two sech-shaped pulses with FWHM duration of 20 ps was 100 GHz, the dispersion was D = 0.4 ps/nm-km.

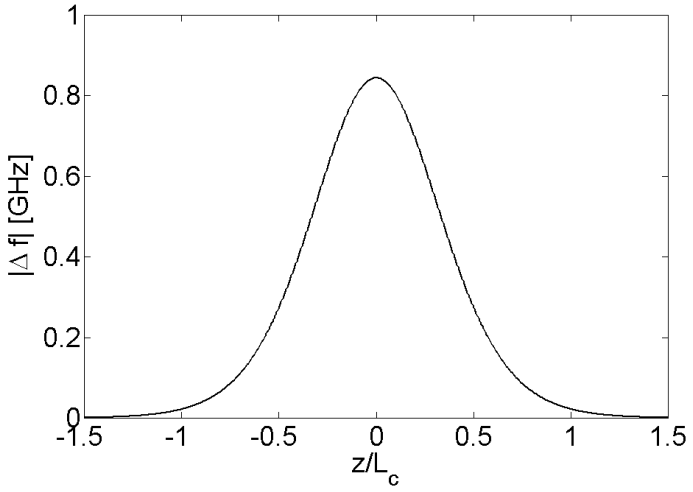

Figure 5-11. *Dependence of frequency shift due to the collision of two solitons in a lossless fiber. Channel spacing was 100 GHz, FWHM duration was 20 ps, dispersion was 0.4 ps/nm-km.*

The overlap of pulses at the input is determined by the initial pulse positioning (IPP). If pulses are initially overlapping, for instance, are placed at the same position in the bit interval, they experience an incomplete collision right at the beginning of the propagation. According to Figure 5-11, this results in a strong frequency shift.

These frequency shifts have been studied in detail for the propagation of classical solitons [13], [95] and periodically amplified soliton systems [1]. However, only single two-soliton collisions have been considered. Beside adding a large contribution to CITJ right at the transmitter, the overlap of pulses at the fiber input also impacts the balance of all the consecutive collisions in the fiber. This effect has not been addressed yet.

In real WDM systems IPP can hardly be controlled since different signal pulse sources, which are typically used for different channels, are mutually never synchronized allowing a slow relative drift in time. This drift results in a variation of the XPM-induced timing jitter. In this section, the impact of random IPP on the accumulated pulse timing jitter for an arbitrary number of collisions is determined.

The 10 x 10 Gbit/s WDM transmission system under investigation is the same as the one introduced in Chapter 4, p. 74 (dispersion map B). Only the amplifier spacing is increased to a value of 100 km (see Table 5-6 for details).

Table 5-6. *Parameters of dispersion map G.*

L_1	95.6	km	D_1	4.0	ps/nm-km
L_2	4.4	km	D_2	-85.0	ps/nm-km
L_{launch}	47.8	km			
L_A	100.0	km			

The channel spacing was varied between 100 GHz and 75 GHz. Gaussian pulses were launched at the input with FWHM duration of 16.75 ps and peak power of 5.78 mW.

The evaluation of statistical CITJ variations using full numerical simulations in a reasonable amount of time is very memory intensive, if possible at all, as one must repeat CITJ calculations very often with different settings of the IPP. However, one can explore the impact of random IPP fluctuations efficiently when using the elastic collision approximation. It is assumed that the IPP of all the channels is randomly varying, mutually independent, and uniformly distributed within the bit interval. For each simulation setup 180 runs were performed[1]. At each run, the initial pulse central times were selected randomly. As a measure of the dependence of CITJ on IPP, the average and variation (± standard deviation) of CITJ values are calculated for each setup.

Figure 5-12 shows results for a middle channel. It shows the average (center solid line) and the variation of CITJ (shaded area around the solid line between the two dashed lines). Figure 5-12 shows that for 100 GHz channel spacing the spread in CITJ after 10,000 km is about 3 ps, while the average timing jitter is 7.6 ps. This average CITJ increases by a factor of 1.5 while the spread doubles and becomes even more significant when the channel spacing is reduced to 75 GHz. Similar curves, as depicted in Figure 5-12, can be obtained for all channels.

1. Convergence of the calculated values is already reached for 100 simulation runs.

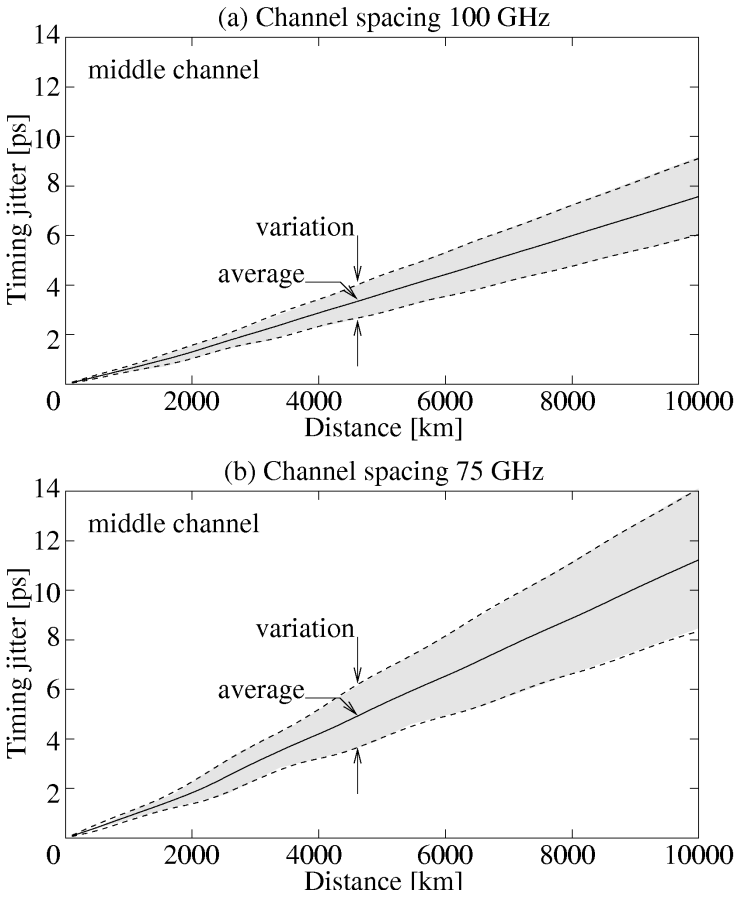

Figure 5-12. *Average and variation of CITJ of the middle channel due to IPP. Dispersion map G was applied (see Table 5-6) [61].*

Note that the humps in the evolution of CITJ for individual IPP settings as observed in Chapter 5, p. 82 have vanished. CITJ is growing almost linearly for increased distance.

Figure 5-13 shows the statistics of CITJ for all the 10 channels after 10,000 km. For each simulation setup, variations (length of bars) of the final timing jitter values are about the same for all channels, namely 3.0 ps (channel spacing 100 GHz) and 5.9 ps (channel spacing 75 GHz), respectively.

While variations are almost constant for each channel, the average timing jitter values of the two outermost channels are smaller compared to the values of the other channels. This means that for the investigated configurations here, random variations of the CITJ per channel due to random IPP

settings are mainly determined by the collisions with pulses in neighboring channels, which is due to the dispersion-induced walk-off between channels.

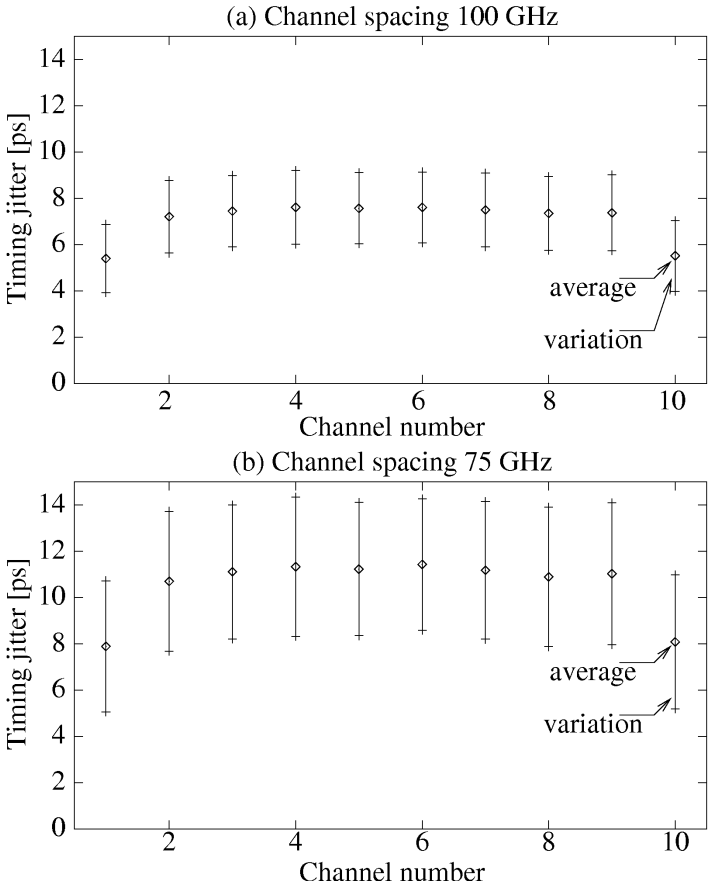

Figure 5-13. *Average and variation of CITJ due to IPP for all channels after 10,000 km.*

Figure 5-13 implies that the observed variations *inside* each channel also lead to a remarkable variation in the accumulated timing jitter values *between* the channels. Figure 5-14 presents the average and variation of the maximum timing jitter differences between the 8 middle channels against distance. The two outermost channels are not regarded in this analysis, since their smaller average timing jitter values would falsify the results. After 10,000 km, the difference of the accumulated timing jitter between the channels varies statistically between around 3.0 ps and 5.0 ps for a channel spacing of 100 GHz, and between around 5.5 ps and 9.5 ps for a channel spacing

of 75 GHz. Thus, while the phase margin is acceptable for some channels, it can be inacceptable for other channels.

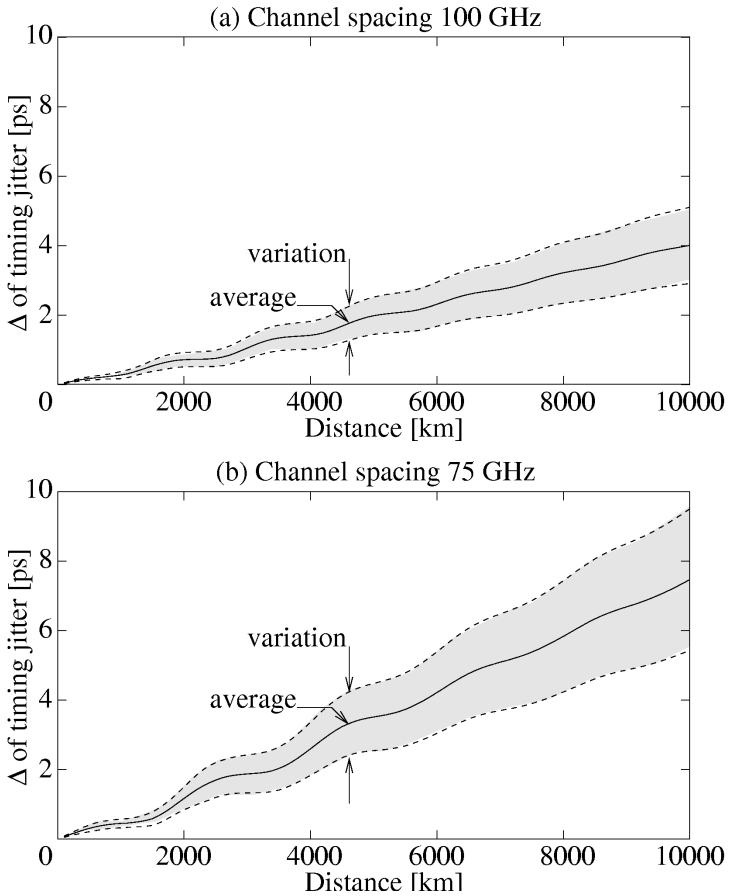

Figure 5-14. *Average and variation of maximum difference of CITJ between channels 2 to 9.*

In summary, random fluctuations of IPP may have a significant impact on the degradation of phase margins in WDM RZ systems, as they introduce large variations of timing jitter from channel to channel. Even if a setup is optimized to yield acceptable phase margins, timing jitter caused by a non-ideal laser source, or pre-propagation effects inside a complex network, can degrade the performance significantly.

Chapter 6

Estimation of system performance

6.1 Overview

In the Chapter 4 sources of distortions of pulse positions were discussed. This chapter is dedicated to the estimation of system performance.

Firstly, the main performance measures of a WDM transmission system are presented. One aspect that these measures all have in common is that timing jitter influences are rather loosely reflected.

Therefore, an estimation model is presented, which determines the influence of amplitude *and* position fluctuations on system performance.

Finally, the influence of timing jitter on the detected BER is investigated for various system examples. It is shown that, depending on the system under consideration, timing jitter might be the major reason for detection errors. It is shown that in the presence of timing jitter, BER estimation using the Gaussian approximation for amplitude fluctuations at the detector might deliver strongly misleading results.

6.2 Performance measures

6.2.1 Optical signal-to-noise ratio (OSNR)

The optical signal-to-noise ratio (OSNR) describes the ratio of optical signal power to optical noise power. For systems limited by ASE-noise from EDFAs, it gives a good estimate of the system performance. It is not suited for the performance estimation of systems where dynamic propagation effects such as dispersion and phase modulation due to the Kerr nonlinearity play an important role. With Eq. (2-33), the OSNR for a single EDFA with constant output power, P_{out}, is given by[1]

$$OSNR = \frac{P_{out}}{P_{ASE}} = \frac{P_{out}}{(NF \cdot G - 1)hf\Delta f} \tag{6-1}$$

where NF is the amplifier noise figure, G is the amplifier gain,

hf is the photon energy,

Δf is the optical measurement bandwidth.

To cover long transmission distances, amplifiers are placed along the line such that they compensate for the total loss along the link. For a periodically amplified fiber link, with N gain-controlled amplifiers compensating for the span loss, the OSNR simply becomes [89]

$$OSNR = \frac{P_{out}}{(NF \cdot G - 1)hf\Delta f \cdot N}. \tag{6-2}$$

Usually, signal and noise power values are measured directly from the optical spectrum analyzer (OSA), which displays power versus wavelength or frequency for a fixed resolution bandwidth of typically $\Delta\lambda = 0.1$ nm ($\Delta f = 12.5$ GHz).

1. ASE-noise is measured here over both polarizations.

6.2.2 Eye-opening penalty (EOP)

The OSNR is a time-averaged performance measure, only the average power of optical carriers and noise are considered. However, dynamic propagation effects such as dispersion, nonlinearities and filtering might strongly influence the pulse shape leaving the average power constant.

The eye-opening penalty (EOP) is a performance measure considering dynamic propagation effects. It is defined as the ratio between a reference eye-opening EO_{ref}, typically gathered from a back-to-back measurement, and the eye-opening after transmission EO_{dec}.

$$EOP(t) = 10\log\left[\frac{EO_{ref}(t)}{EO_{dec}(t)}\right] \tag{6-3}$$

where t is the sample time within the bit interval,

EO is the difference between the amplitudes of the lowest mark and the highest space.

The EOP is especially useful for noise-free system evaluations, as it gives a useful measure of deterministic pulse distortion effects. Note that it is dependent on the sample time, where the eye-opening is measured within the bit interval. When the detected eye shows timing jitter resulting from intra- or interchannel ISI effects, the optimum EOP might not be affected. However, the sampling width over which an EOP below a certain threshold level can be achieved will be.

If noise is present, determination of the EOP can become ambiguous as the definition of lowest mark and highest space depends on the simulated bit stream[1]. A better method of determining the eye-opening is given by [33]

$$EO = (\mu_1 - 3\sigma_1) - (\mu_0 + 3\sigma_0) \tag{6-4}$$

where $\mu_{0,1}$ are the mean values of the spaces and marks, respectively,

$\sigma_{0,1}$ are the standard deviations of the spaces and marks, respectively.

1. If an infinite number of bits could be collected to plot the eye diagram, it would be totally closed.

For Gaussian amplitude fluctuations, the value range $(\mu, \mu \pm 3\sigma)$ incorporates approximately 99.7% of all possible cases.

6.2.3 Q-factor

Another parameter that determines system performance is the Q-factor. It is defined as the difference between mean level of marks and spaces, normalized by the sum of their standard deviations [18].

$$Q = \frac{\mu_1 - \mu_0}{\sigma_1 + \sigma_0}. \tag{6-5}$$

The Q-factor can be related to the eye-opening as depicted in Figure 6-1.

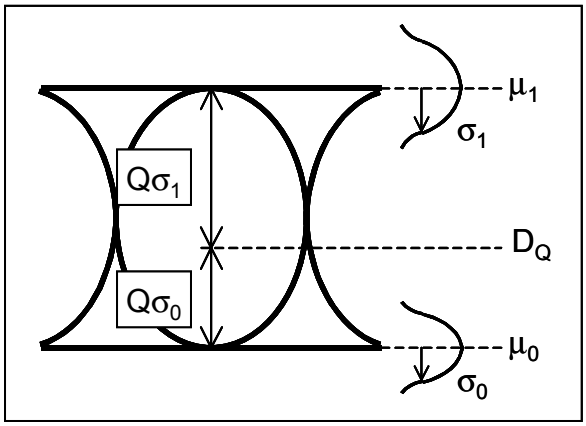

Figure 6-1. *Relationship between eye-opening and Q-factor.*

When amplitude fluctuations of the marks and spaces follow a Gaussian probability density function (PDF), given by [140]

$$f_X(x) = \frac{1}{\sqrt{2\pi}\sigma} \exp\left(-\frac{(x-\mu)^2}{2\sigma^2}\right) \tag{6-6}$$

the threshold D_Q corresponds to the value, where the arguments of the exponentials in both Gaussian PDFs are identical. It is given by

$$D_Q = \frac{\sigma_0 \mu_1 + \sigma_1 \mu_0}{\sigma_0 + \sigma_1}. \tag{6-7}$$

The OSNR can be used to derive an approximate value for the Q-factor, if the system under investigation shows no significant performance degradation from propagation effects other than noise (such as dispersion and nonlinearities), and an infinite extinction ratio is assumed. The Q-factor can be related to the OSNR at the output of the receiver for a system using an optical pre-amplifier, which ensures that the input power to the receiver is high so that thermal and shot noise are negligible. The Q-factor in dB[1] is then given by [154]

$$Q_{dB} = 20\log\left(\frac{2OSNR\sqrt{B_o/B_e}}{1+\sqrt{1+4OSNR}}\right) \tag{6-8}$$

where B_o is the bandwidth of the optical receiver,

B_e is the bandwidth of the electrical post-detection filter.

The relationship assumes that signal-ASE beat noise and ASE-ASE beat noise are the main contributions to electrical noise at the detector.

6.2.4 Bit error rate (BER)

Ultimate measure of system performance is the bit error rate (BER). It is defined as probability of faulty detected bits, e.g, marks detected as spaces and vice versa.

6.2.4.1 Monte Carlo (MC) experiment

The direct way of measuring BER is to calculate the ratio of corrupt detected bits to total number of transmitted bits over a statistically significant time period in so-called Monte Carlo (MC) experiments. No assumptions about the probability distributions need to be applied. The BER found in MC experiments is the system performance measure, which is most closely related to realistic system conditions.

However, for fiber-optic communication systems BER values of interest are usually very small (10^{-9} – 10^{-12}). This makes it difficult to measure the BER directly as error counting needs to be performed over very long, some-

1. Logarithmic Q is related to linear Q by $Q_{dB} = 20\log(Q)$.

times impossibly long time intervals. It is even more difficult to estimate the BER via MC experiments from computer simulations. The variance of the estimated BER in a MC experiment is given by [157]

$$\sigma_{MC}^2 = \frac{P_e(1-P_e)}{N} \tag{6-9}$$

where P_e is the probability of error,

N is the number of test samples in the MC experiment.

So to estimate a BER of 10^{-9}, errors over at least 10^{11} bits need to be counted to achieve an estimation accuracy[1] of about 10%. This is barely possible in laboratory experiments, however, totally unfeasible in computer simulations.

Therefore, techniques for approximating the BER are usually applied in computer simulations. All these techniques make certain assumptions about the PDF of amplitude fluctuations of marks and spaces at the detector (statistical techniques) or about the considered class of systems (analytical or semi-analytical techniques).

6.2.4.2 Gaussian approximation (GA)

One statistical approach commonly applied is the so-called Gaussian approximation (GA) technique. It is based on the assumption that amplitude fluctuations of marks and spaces are Gaussian distributed. Under this assumption, the BER is derived as

$$\begin{aligned} BER &= \frac{1}{N_0+N_1}[N_1 P(0|1) + N_0 P(1|0)] \\ &= \frac{1}{N_0+N_1}\left[\frac{N_1}{2}\operatorname{erfc}\left(\frac{|\mu_1 - D|}{\sqrt{2}\sigma_1}\right) + \frac{N_0}{2}\operatorname{erfc}\left(\frac{|\mu_0 - D|}{\sqrt{2}\sigma_0}\right)\right] \end{aligned} \tag{6-10}$$

where $P(a|b)$ is the probability that a is received while b was sent,

$N_{1,0}$ denotes the number of marks and spaces, respectively,

$\operatorname{erfc}(x) = \frac{2}{\sqrt{\pi}}\int_x^\infty e^{-t^2}dt$ denotes the complementary error function,

D is the decision threshold.

1. Measured as the width of the standard deviation.

The optimum decision threshold D_{opt}, i.e., the amplitude value for which the detected BER becomes minimum, is given at the point where the Gaussian PDFs for marks and spaces cross each other, namely where

$$\frac{1}{\sigma_0}\exp\left(-\frac{(D_{opt}-\mu_0)^2}{2\sigma_0^2}\right) = \frac{1}{\sigma_1}\exp\left(-\frac{(\mu_1-D_{opt})^2}{2\sigma_1^2}\right). \tag{6-11}$$

D_{opt} can be derived to

$$D_{opt} = \begin{cases} \dfrac{\mu_1-\mu_0}{2} & \text{for } \sigma_0 = \sigma_1 \\ \dfrac{\sigma_0^2\mu_1-\sigma_1^2\mu_0-\sigma_1\sigma_0\sqrt{(\mu_1-\mu_0)^2+(\sigma_0^2-\sigma_1^2)\ln(\sigma_0^2/\sigma_1^2)}}{\sigma_0^2-\sigma_1^2} & \text{for } \sigma_0 \neq \sigma_1 \end{cases}. \tag{6-12}$$

Under certain presumptions, the BER can be estimated indirectly by calculating the Q-factor. Both measures can be exactly related, for the case that the decision threshold is set as given in Eq. (6-7) and that the number of transmitted marks equals the number of transmitted spaces.

$$BER = \frac{1}{2}\operatorname{erfc}\left(\frac{Q}{\sqrt{2}}\right) \approx \frac{1}{Q\sqrt{2\pi}}\exp\left(-\frac{Q^2}{2}\right) \tag{6-13}$$

The approximate solution in Eq. (6-13) is derived from an upper bound approximation of the integration by parts of the erfc-function [99]. Figure 6-2 plots BER versus Q-factor highlighting several reference values.

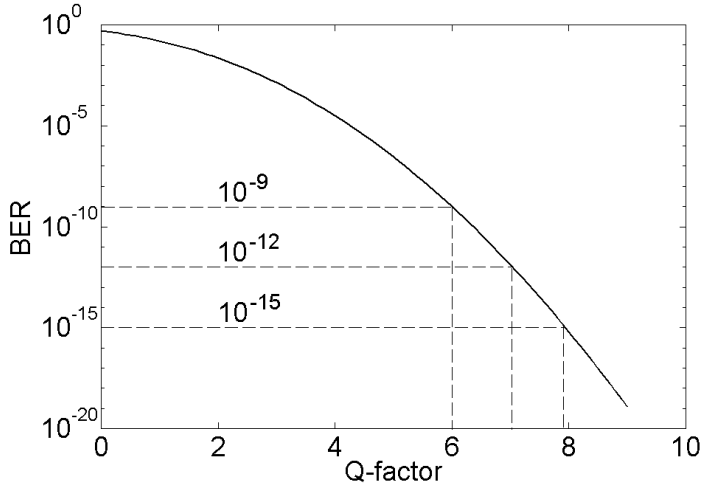

Figure 6-2. *BER versus Q-factor according to Eq. (6-13).*

Note that the optimum decision threshold, e.g., the amplitude where the PDFs for amplitude fluctuations of marks and spaces cross each other, is not the same as applied in Eq. (6-13). To visualize the difference, Figure 6-3 plots both decision thresholds for different ratios of the variances for marks and spaces, σ_0^2/σ_1^2. The mean of marks and spaces are set to one and zero, respectively.

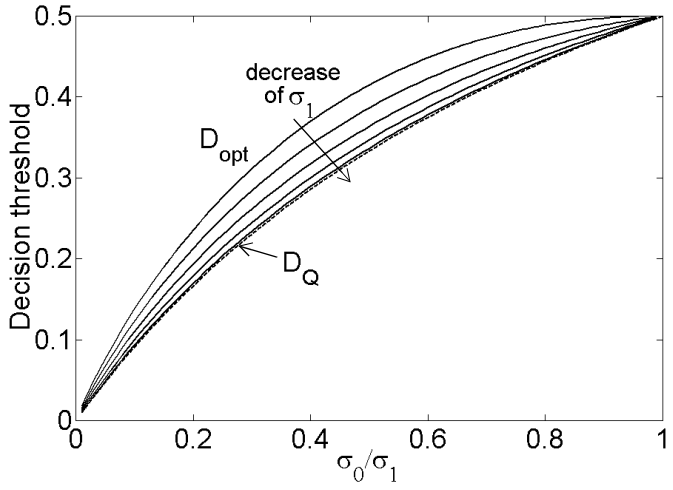

Figure 6-3. *Decision thresholds for different ratios of* σ_0^2/σ_1^2*, with* $\mu_0 = 0$ *and* $\mu_1 = 1$*. Solid lines: Decision threshold according to Eq. (6-12), with* $\sigma_1/\mu_1 = 0.5, 0.4, 0.3, 0.2, 0.1$*. Dashed line: Decision threshold according to Eq. (6-7).*

Figure 6-3 clearly shows the difference between both decision thresholds for large numbers of σ_1^2, and thus the misinterpretation of the estimated BER. Note, however, that for realistic applications in fiber-optic communications, where BER estimates of about 10^{-9} to 10^{-15} are of interest, the difference becomes marginal, and the approximate formula for the decision threshold as given in Eq. (6-7) is good enough[1].

Although the GA allows BER estimation to be feasible in computer simulations, it still requires a large number of test bits to estimate the mean and variance of the amplitude fluctuations with a good degree of numerical confidence. For example, 800 bits need to be simulated to achieve 95% estimation accuracy for the linear Q-factor. However, as the BER is related via the complementary error function with the estimated standard deviation, and not linearly like the Q-factor, the same number of bits will lead to a fluctuation of 1.5 orders of magnitude for BER estimation around 10^{-9}. An example scenario is presented in Chapter 6, p. 112.

Beside numerical uncertainties, the validity of the GA needs to be investigated very carefully. Even though disturbances tend to be Gaussian for a reasonably large number of sources (central limit theorem [142]), and thus would imply the validity of the GA, it fails for several practical cases. One reason is that initially Gaussian disturbances are passed through nonlinear elements (fiber, receiver) altering the statistics. Also intra- and interchannel interferences might result in degrading effects, which could not be approximated by additive Gaussian disturbances, mainly because the critical number of interacting sources is not obtained.

Gaussian approximation including intersymbol interferences (GA-ISI)

An alternate approach is based on the GA technique, but considers intrachannel intersymbol interferences (ISI) from neighboring bits [11]. Instead of relating the Gaussian PDF of amplitude fluctuations to marks and spaces only, all three-bit patterns are considered separately. That is, four patterns are associated for each mark (010, 110, 011, 111) and for each space (101, 001, 100, 000). The BER is given as the superposition of the BER calculated

1. For cases, where Forward-Error Correction (FEC) schemes are used, BER values of up to 10^{-3} are of interest, and thus a proper selection of the decision threshold is important.

for the center bit of all eight patterns, weighted with respect to the number of occurrences each pattern is propagated in the bit sequence,

$$BER = \frac{1}{8N}\sum_{k=1}^{8} N_k \mathrm{erfc}\left(\frac{|\mu_k - D|}{\sqrt{2}\sigma_k}\right) \tag{6-14}$$

where N_k is the number of occurrences of the pattern k, and $N = \sum_{k=1}^{8} N_k$.

Note that the price for obtaining higher precision when including ISI effects is that this technique requires a sample set of bits approximately four times larger than the GA technique in order to reach the same numerical accuracy as the GA technique.

6.2.4.3 Deterministic noise approximation (DNA)

If phase interactions between the noise from optical amplifiers and the WDM signal comb can be neglected, noise can be modeled deterministically at the optical receiver. This is possible, for instance, when the noise and signal streams are modeled to propagate separately from each other over the transmission link using multiple signal representations [101]. The optical signal can be represented by its full time dynamics. It is passed to the receiver as a noise-free signal, however, taking deterministic impairments, such as dispersion, crosstalk due to FWM and due to non-ideal filtering along the optical path into account. Noise is described by wavelength-sensitive values of its power spectral density (PSD) directly. It is passed along the optical path to obtain a deterministic measure of accumulated noise PSD versus wavelength at the receiver input.

The variance of amplitude fluctuations for each bit is determined from the noise accumulated along the optical path and the noise from the receiver. The variance of the pulse amplitude can be written as

$$\sigma_a^2 = \sigma_{signal,ASE}^2 + \sigma_{ASE,ASE}^2 + \sigma_{sh}^2 + \sigma_{th}^2 \tag{6-15}$$

where $\sigma^2_{signal,ASE}$ is the Signal-ASE beat noise, as defined in Eq. (2-38),

$\sigma^2_{ASE,ASE}$ is the ASE-ASE beat noise, as defined in Eq. (2-39),

σ^2_{sh} is the shot noise of the receiver unit, as defined in Eq. (2-36),

σ^2_{th} is the thermal noise of the receiver unit including the electrical preamplifier, as defined in Eq. (2-37).

The main advantage of the DNA technique over the GA technique lies in the fact that the demand for simulations of long bit streams is drastically reduced, as there is no numerical uncertainty in determining the amplitude variances. An example comparison with the GA technique is presented in Chapter 6, p. 112.

However, the DNA technique still suffers from assumptions made about the underlying PDFs of fluctuations for marks and spaces. It has, for instance, been derived theoretically [105], and shown experimentally [28] that the PDF of ASE-ASE beat noise is not Gaussian. Systems which are limited by ASE-noise contributions are better modeled by a chi-squared PDF for the marks and spaces [104], [3]. Other modeling techniques are based on finding the moment generating function[1] for marks and spaces at the detector considering the influence of the nonlinear receiver characteristic and the filtering on Gaussian noise sources [86], [87].

6.3 Impact of pulse timing jitter on BER

6.3.1 Motivation

To detect pulses correctly, the minimum amplitude as well as phase margins need to be considered. The reduction of the phase margin might be induced by timing jitter, e.g., statistical fluctuations of the pulse positions. Timing jitter manifests itself at the decision circuitry in fluctuations of the

1. Which is the Laplace-transform of the PDF.

detected amplitude. Even though the received pulse position might be regarded as following a Gaussian distribution [77], [108], the resulting amplitude fluctuations at the decision circuitry are not. They are strongly dependent on the received pulse shape, which might be affected by fiber propagation effects as well as the optical and electrical filter transfer functions at the receiver. As with noise contributions, a large number of bits would be required to be propagated over the WDM system link in order to investigate the timing jitter by calculating mean and variance of pulse positions directly and derive from them the phase margin[1].

System performance in the presence of timing jitter has been discussed in some detail in [81] and others. The derived solutions, however, are either of general nature without applicable solutions, or are very specific, making severe assumptions about the pulse shape, e.g, are only valid for NRZ transmission, or rectangular-shaped RZ pulses. In [108], joint measurement of timing jitter and Q-factor was used to predict the performance for a single channel soliton system. It has been shown that when the decision variable is not Gaussian, the Q-factor is not sufficient to describe the system performance.

In the following section, a technique is presented that considers fluctuations of pulse amplitudes and positions for arbitrary pulse shapes, without the need to simulate extensively long bit sequences. The BER is estimated from the superposition of both effects.

6.3.2 Modeling

In Chapter 6, p. 108, the deterministic noise approximation technique was introduced that allowed a fast and efficient estimation of the statistical amplitude fluctuations due to noise and crosstalk sources. The total PDF of amplitude fluctuations was assumed to be Gaussian with variance defined in Eq. (6-15).

In Chapter 4, efficient techniques were developed for estimating the accumulation of pulse timing jitter due to the main sources of phase margin degradations in long-haul transmission systems, namely XPM and ASE-noise. These techniques are restricted to finding estimates of the pulse position

1. See Chapter 4, p. 59 for a more detailed discussion.

average and variance only, as it has been widely accepted that pulse position deviations due to these random processes are sufficiently described by a Gaussian distribution [77], [108].

At the detector, the effects of all stochastic disturbances are summarized. In order to investigate the impact of the different sources of timing jitter on the total BER, their influence needs to be translated through the optical receiver onto the electrical pulse shape seen by the decision circuitry. After the optical receiver, the pulse shape is changed, depending on the response of the photodiode and the electrical filter. However, it is assumed that the relative phase information of individual bits is not changed, such that individual pulse positions after the receiver are assumed to still follow a Gaussian distribution.

The translation of pulse position statistics to pulse amplitude statistics is strongly dependent on the pulse shape at the detector. To illustrate this, the inverse of the average pulse shape $g^{-1}(p) = t$ is approximated using a Taylor series expansion at an arbitrary power level p_0

$$g^{-1}(p_0) = t_0 = a_0 + a_1 p_0 + a_2 p_0^2 + O(\langle p_0 \rangle^3) \tag{6-16}$$

where a_0, a_1 and a_2 are the bias, slope and curvature, respectively, of the inverse of the pulse shape at p_0.

For pure timing jitter disturbances, the PDF of the pulse amplitude p can then be written for an arbitrary sample time t as [134]

$$f_t(p) = B(t)\exp\left[-\frac{1}{2\tilde{\sigma}_t^2}\left(p_0 - \frac{t-a_0}{a_1}\right)\right]\delta(p-p_0)\times \exp\left\{-\frac{p_0}{2\tilde{\sigma}_t^2}\left[\left(\frac{a_2}{a_1}p_0\right)^2 + 2\frac{a_2}{a_1}\left(p_0 - \frac{t-a_0}{a_1}\right)\right]\right\} \tag{6-17}$$

where $B(t)$ denotes a pulse shape related correction factor,
$\delta(x-y)$ is the continuos Dirac-delta function,
$\tilde{\sigma}_t^2 = \sigma_t / a_1$ is the normalized variance of the timing jitter.

Eq. (6-17) suggests that if the curvature could be neglected $(a_2 \approx 0)$, Gaussian distributed pulse position fluctuations would result in Gaussian distributed amplitude deviations with scaled variance. However, for many RZ transmission systems, this cannot be assumed. So depending on the received pulse shape, pulse timing jitter might lead to strongly non-Gaussian amplitude fluctuations. Comparisons of the technique presented here with the GA technique are presented in the following chapter.

The total PDF, which determines the BER, is given by the weighted sum of all individual PDFs gathered from the pulse energy and position fluctuations with respect to amplitude p (see Figure 6-4).

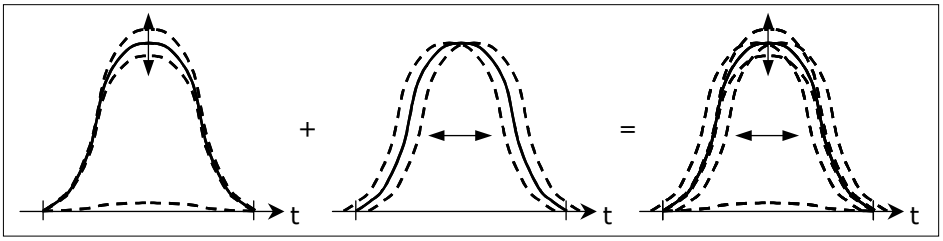

Figure 6-4. *Total PDF as superposition of PDFs from amplitude and timing fluctuations.*

Note that this technique considers deterministic pattern effects due to amplitude fluctuations, but ignores ISI effects resulting from timing jitter. However, this might be important for soliton systems where close temporal placement of pulses invokes soliton interactions[1], which influence the position of neighboring pulses [130].

6.4 WDM system simulations - BER

Diverse system scenarios are investigated in this section to illustrate the effectiveness of the different BER estimation techniques proposed in the previous sections. Results have been published in [134].

1. See Chapter 3, p. 34 for details.

6.4.1 RZ system over dispersion-managed link with mainly SSMF

In the first example, a single-channel transmission system is investigated, where timing jitter effects are negligible. Pulses are propagated with a bitrate of 40 Gbit/s. The transmission link consists mainly of SSMF with a nominal dispersion of 16 ps/nm-km. DCF spans with D = -90 ps/nm-km are inserted to provide 100% dispersion compensation. The RZ pulses are launched with 25% rise time and FWHM duration of 12.5 ps. No extra phase modulation is applied. The receiver consists of a PIN photodiode and a 3rd order Bessel filter with a 3-dB bandwidth of 32 GHz.

Firstly, the BER calculation method based on the deterministic noise description (DNA method)[1] is compared with the standard method of estimating the mean and variance of pulse amplitude fluctuations due to noise contributions directly (GA method)[2]. For this, a single RZ signal stream is transmitted over 2,000 km, applying optical inline amplifiers with a noise figure of 6.0 dB and a periodic spacing of about 94 km.

The modeled system example is limited by pulse energy fluctuations due to signal-ASE and ASE-ASE beat noise; timing jitter effects can be neglected. Figure 6-5 shows the calculated BER values versus distance. Lines with crosses correspond to the DNA method using a signal stream of 128 bits, whereas lines with squares correspond to the GA method based on 128 bits in the upper graph and 1024 bits in the lower graph.

1. See Chapter 6, p. 108 for details.
2. See Chapter 6, p. 104 for details.

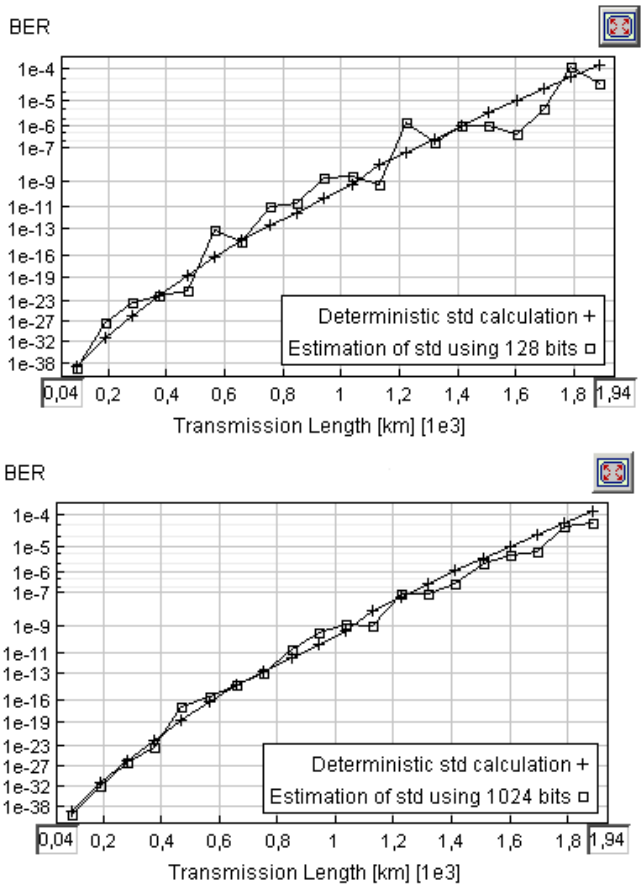

Figure 6-5. *BER versus distance for the DNA technique (crosses) and the GA technique (squares) using 128 bits (upper) and 1024 bits (lower) [134].*

The upper graph shows strong fluctuation of BER values calculated with the GA technique because of poor numerical estimation accuracy. It is clearly visible that 128 bits are not sufficient to give a reasonably good BER estimation. The smooth, straight increase with distance of BER values calculated with the DNA technique suggests that all important stochastic effects had been sufficiently modeled using the separable noise representation [101].

The lower graph suggests that results from both techniques converge if the uncertainty of moment estimation is eliminated by increasing the bit stream length sufficiently. This also implies that timing jitter effects are, indeed, not of system limiting importance for the modeled setup. The advantage of the DNA technique is obvious in this case as it allows an increase of simulation speed by about one order of magnitude.

6.4.2 Dispersion-managed soliton system

In the next example a WDM transmission system is considered using dispersion-managed solitons. Ten channels are transmitted with a bitrate of 10 Gbit/s per channel and a channel spacing of 100 GHz. The dispersion map is the same as described in Table 4-1 (dispersion map A). The optical inline amplifiers have a noise figure of 4.0 dB and are spaced by 50 km. Gaussian pulses were launched with a FWHM width of 16.75 ps and a peak power of 2.8 mW. Pulses in neighboring channels were misplaced by half a bit interval to avoid initial interchannel pulse collisions. The receiver unit consists of a PIN photodiode, and a 3^{rd} order Bessel filter with a 3-dB bandwidth of 7.5 GHz.

After 5,000 km the BER is estimated using the estimation technique described in Chapter 6, p. 109, which considers energy fluctuations and timing jitter statistics. The accumulated timing jitter is approximately 4 ps (4% of bit duration), where ASE-noise induced timing jitter (ANTJ) is approximately 1.75 ps, and collision-induced timing jitter (CITJ) is approximately 3.59 ps. The amplitude fluctuations due to the direct overlay of ASE-noise and pulse-to-pulse interactions could be estimated at the detector to be approximately 4% for the marks and 1% for the spaces with respect to the average peak power value.

Figure 6-6 shows an eye-mask with surface lines denoting constant BER values. The outermost line corresponds to the average pulse shape after the electrical post-detection filter, the innermost one corresponds to a BER of 10^{-9}. The figure clearly shows that the BER is limited by timing jitter, which in this case, is mainly caused by interchannel XPM effects.

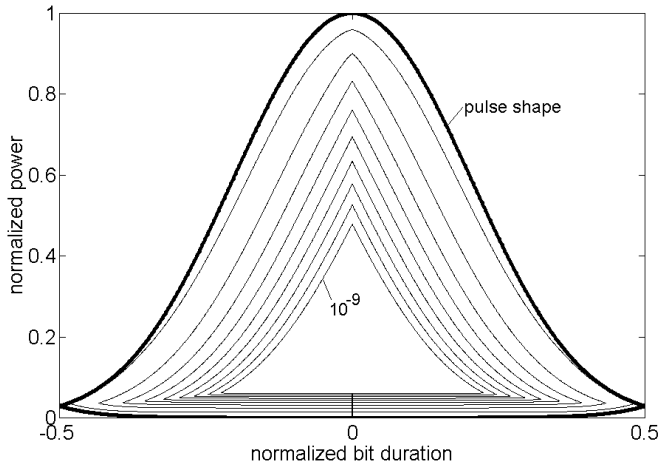

Figure 6-6. *BER eye-mask after 5,000 km WDM transmission using DMSs considering timing jitter and amplitude noise [134].*

Figure 6-7 shows the BER versus decision threshold for two different sample points, namely in the middle and 10% off the middle of the bit interval. The solid curves refer to the approach of considering the statistics of amplitude fluctuations due to timing jitter. The dashed lines are drawn for the assumption that amplitude fluctuations are Gaussian in distribution (GA technique). The graph shows clearly that the BER would have been underestimated by orders of magnitude without considering the timing jitter properly.

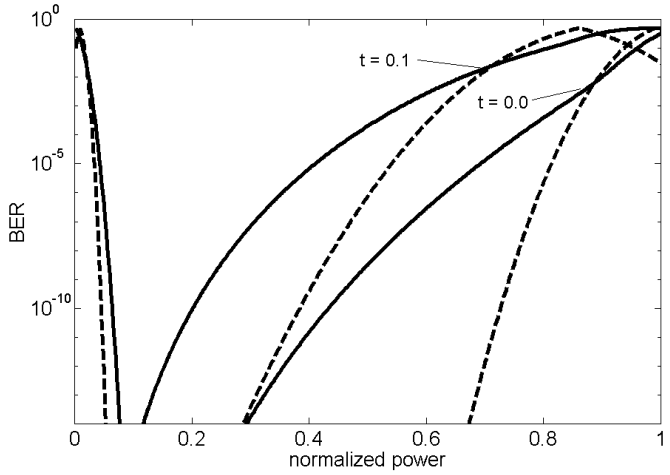

Figure 6-7. *BER versus decision threshold after 5,000 km WDM transmission using DMSs considering timing jitter and amplitude noise at two different sample points: t = 0.0 (middle of the bit interval) and t = 0.1 (10% from the middle of the bit interval); pure Gaussian amplitude approximation (dashed), inclusion of timing jitter statistics (solid) [134].*

6.4.3 Chirped RZ system

In the final example, the BER was calculated for a 10-channel WDM transmission system using chirped RZ pulses. The pulses launched initially were raised-cosine shaped with a peak power of 0.6 mW. Sinusoidal phase modulation was applied to each pulse with an initial phase offset of –90° and an index of approximately 108° (m_p = 0.6). The extinction ratio at the transmitter was 15 dB. The dispersion map is described in Table 5-4 (dispersion map E). The inline amplifiers have a nominal noise figure of 4.0 dB and were placed every 45 km. The same receiver unit is used as described in Chapter 6, p. 115.

The BER was calculated after 5,000 km right at the output of the 10th dispersion map. The accumulated timing jitter was estimated to be approximately 5.2 ps. The major contribution was due to ASE-noise with approximately 5.0 ps, whereas XPM effects contribute to only 1.2 ps. Timing jitter accumulation due to ASE-noise and interchannel XPM effects differ between the presented DMS and CRZ system scenarios because of the different dispersion maps. For the DMS transmission scenario, pulses do not

broaden significantly outside a bit interval, whereas for the CRZ transmission, pulses broaden over more than two bit durations experiencing strong pulse shaping effects over the dispersion map. The standard deviation of amplitude fluctuations is also increased: for marks to approximately 7% of the average peak power value, and for spaces to 2%.

Figure 6-8 shows the eye-mask with surface lines denoting constant BER values. Figure 6-9 shows BER versus decision threshold for two different sample points. Both figures show clearly that system performance is limited by timing jitter due to interactions between signal and ASE-noise. Even though amplitude fluctuations are also increased they are not of system limiting importance. Figure 6-9 shows that overly confident BER values would be calculated without considering the statistics of timing jitter properly.

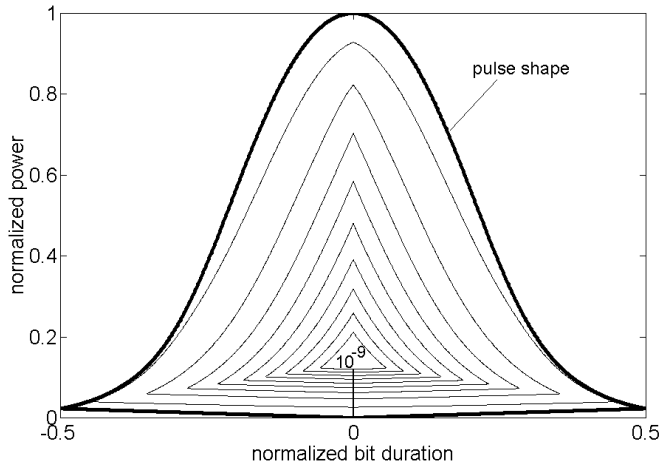

Figure 6-8. *BER eye-mask after 5,000 km WDM transmission using CRZs considering timing jitter and amplitude noise [134].*

Investigating the eye-masks of the DMS and CRZ cases, the BER is strongly dependent on the detected pulse shape. This is of significant importance for RZ modulation formats with narrow pulse peak plateaus, as was for the cases discussed here.

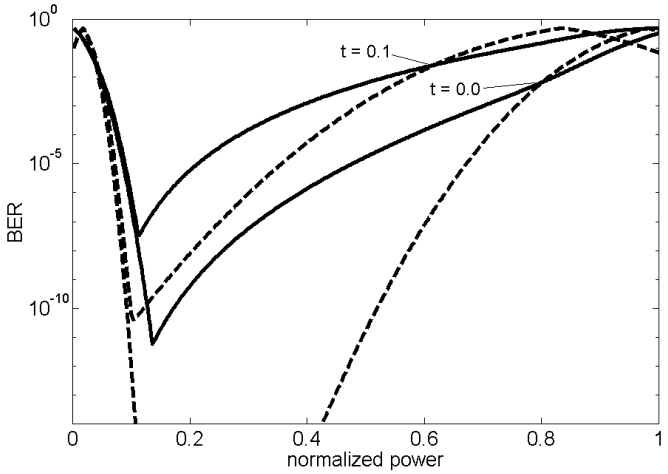

Figure 6-9. *BER versus decision threshold after 5,000 km WDM transmission using CRZs considering timing jitter and amplitude noise at two different sample points: t = 0.0 (middle of the bit interval) and t = 0.1 (10% from the middle of the bit interval); pure Gaussian amplitude approximation (dashed), inclusion of timing jitter statistics (solid) [134].*

In summary, BER has been estimated for diverse system examples using fast and memory efficient techniques. The aspect these techniques all have in common is that they increase estimation speed and accuracy by orders of magnitude. However, special care needs to be applied when using these techniques as they are not universally applicable.

Chapter 7

Summary

The presented work summarizes a contribution to the investigation of timing jitter in long-haul WDM transmission systems applying return-to-zero (RZ) modulation formats. Efficient modeling techniques for calculating timing jitter due to optical amplifier noise and interchannel cross-phase modulation were presented and validated. The influence of various system parameters on timing jitter accumulation was analyzed.

This work was started with a presentation of recent trends in the design of long-haul WDM systems. Design considerations of the optical transmitter, the optical fiber propagation including optical amplifiers and the optical receiver were discussed. Different RZ modulation formats were presented, which are of great interest for long-haul propagation. The time and frequency dynamics of dispersion-managed soliton (DMS) and chirped return-to-zero (CRZ) pulses were discussed in detail. Trends of convergence between DMS- and CRZ-based transmission systems and other new modulation formats were presented as well.

After a brief overview of the main distortions that occur in long-haul WDM transmission, investigations were concentrated on the two main sources of pulse timing jitter in long-haul fiber-optic transmission systems. These jitter sources are noise generated from optical amplifiers, and interchannel cross-phase modulation. A recently reported approach for the calculation of ASE-noise induced timing jitter (ANTJ) was presented and implemented in a semi-analytical algorithm. As one of the main achievements of this work, a new semi-analytical algorithm was developed for calculating collision-induced timing jitter (CITJ) considering RZ pulses of arbitrary shapes. Both algorithms solve an analytically derived solution for the variance of the pulse central time considering local pulse shape informa-

tion, which is obtained as numerical solution of the generalized nonlinear Schrödinger equation (GNLS).

The main advantage of the newly developed algorithms is that they do not make any assumption about the propagated pulse shapes, and that they reduce the computational effort for calculating timing jitter by orders of magnitude compared to full numerical simulations. This allows a systematic optimization of parameters for many long-haul WDM RZ transmission systems. This is not possible, if only full numerical simulations would be available. The algorithms were implemented in an commercially available software package from VPIsystems for modeling and analyzing WDM transmission systems [153]. The applicability of the algorithms was validated for various system conditions.

Another main achievement of this work is the in-depth analysis of timing jitter accumulation in typical long-haul WDM system scenarios employing the most common modulation formats, namely DMS and CRZ. It was shown that timing jitter accumulation depends strongly on the dispersion map, and amplifier positioning. Together with the channel spacing, these parameters determine the number of pulses interacting nonlinearly during propagation. It was found that the variance of the pulse central time is proportional to the inverse of the cube of the channel spacing, and that initial pulse positioning inside the bit interval plays a crucial role on the accumulation of CITJ. Finally, the influence of timing jitter on the detected BER was investigated for various system examples employing RZ modulation formats. It was shown that timing jitter might be the limiting factor in long-haul propagations, and that an BER estimation technique using the approximation that amplitude fluctuations at the detector are Gaussian distributed when timing jitter is present, might deliver strongly misleading results.

As outlook, schemes for reducing or even suppressing the effect of XPM-induced timing jitter could be investigated. It should be worth applying solutions derived for NRZ systems, such as [17], to RZ systems. Also, it would be of great interest to find a closed description for the impact of XPM on system performance, which combines the gathered knowledge for RZ systems, where XPM results mainly in timing jitter, and NRZ systems, where XPM results mainly in amplitude jitter. Finally, the accumulation of CITJ in the presence of PMD, and the accumulation of ANTJ and CITJ in systems employing distributed amplification could be investigated.

References

[1] T. Aakjer, J. H. Povlsen, and K. Rottwitt, *Effects of initial overlap in a wavelength-division-multiplexed soliton transmission system*, Opt. Letters, vol. 18, pp. 1908-1910, 1993.

[2] M. J. Ablowitz, G. Biondini, S. Chakravarty, and R. L. Horne, *On timing jitter in wavelength-division-multiplexed soliton systems*, Opt. Commun., vol. 150, pp. 305-318, 1998.

[3] F. Abramovich, and P. Bayvel, *Some statistical remarks on the derivation of BER in amplified optical communication systems*, IEEE Trans. Commun. vol. 45, pp. 1032-1034, 1997.

[4] G. P. Agrawal, *Nonlinear fiber optics*, 2nd edition, Academic Press, London, pp. 7–12, 1995.

[5] G. P. Agrawal, *Nonlinear fiber optics*, 2nd edition, Academic Press, London, pp. 19–20, 1995.

[6] G. P. Agrawal, *Nonlinear fiber optics*, 2nd edition, Academic Press, London, Chapter 2, 1995.

[7] G. P. Agrawal, *Fiber optic communication systems*, 2nd edition, John Wiley & Sons, New York, pp. 163–165, 1997.

[8] G. P. Agrawal, *Fiber optic communication systems*, 2nd edition, John Wiley & Sons, New York, pp. 172, 1997.

[9] S. B. Alleston, P. Harper, I. S. Penketh, I. Bennion, N. J. Doran, and A. D. Ellis, *1220 km propagation of 40 Gbit/s single channel RZ data over dispersion managed standard (non-dispersion shifted) fibre*, Opt. Fiber Commun. Conf., San Diego, CA, paper PD3, 1999.

[10] D. Anderson, *Variational approach to nonlinear pulse propagation in optical fibers*, Physic. Review A, vol. 27, pp. 3135–3145, 1983.

[11] C.J. Anderson, and J.A. Lyle, *Technique for evaluating system performance using Q in numerical simulations exhibiting intersymbol interference*, Electron. Letters, vol. 30, pp. 71–72, 1994.

[12] B. A. Andrekson et al., *Soliton collision interaction force dependence on wavelength separation in fiber amplifier based systems*, Electron. Letters, vol. 26, pp. 1499-1501, 1990.

[13] P. A. Andrekson, N. A. Olson, J. R. Simpson, T. Tanbun-Ek, R. A. Logan, P. C. Beaker, and K. W. Wecht, *Observation of multi-wavelength soliton collisions in optical systems with fibre amplifiers*, Appl. Physics. Letters, vol. 57, pp. 1715-1719, 1990.

[14] W. C. Barnett, et al., *The TPC-5 cable network*, IEEE Commun. Magazin, February 1996.

[15] P. C Becker, N. A. Olsson, and J. R. Simpson, *Erbium-doped fiber amplifiers, fundamentals and technology*, Academic Press, 1999.

[16] P.-A. Belanger, and C. Pare, *Second-order moment analysis of dispersion managed solitons*, J. Lightwave Technol., vol. 17, pp. 445-451, 1999.

[17] G. Bellotti, and S. Bigo, *Cross-phase modulation suppressor for multispan dispersion-managed WDM transmissions*, IEEE Photon. Technol. Letters, vol. 12, pp. 726-728, 2000.

[18] N. S. Bergano, F. W. Kerfoot and C. R. Davidson, *Margin measurements in optical amplifier systems*, IEEE Photon. Technol. Letters., vol. 5, pp. 304–306, 1993.

[19] N. S. Bergano, C. R. Davidson, M. Ma, A. Pilipetskii, S. G. Evangelides, H. D. Kidorf, J. M. Darcie, E. Golovchenko, K. Rottwitt, P. C. Corbett, R. Menges, M. A. Mills, B. Pedersen, D. Peckham, A. A. Abramov, and A. M. Vengsarkar, *320 Gb/s WDM transmission (64x5 Gb/s) over 7200 km using large mode fiber spans and chirped return-to-zero*, Opt. Fiber Commun. Conf., San Jose, CA, paper PD12, 1998.

[20] N. S. Bergano, C. R. Davidson, C. J. Chen, B. Pederson, M. A. Mills, N. Ramanujam, H. D. Kidorf, A. B. Puc, M. D. Levonas, and H. Abdelkader, *640 Gb/s transmission of sixty-four 10 Gb/s WDM channels over 7200 km with 0.33 (bits/s)/Hz spectral efficiency*, Opt. Fiber Commun. Conf., San Diego, CA, paper PD2, 1999.

[21] A. Berntson, N. J. Doran, W. Forysiak, and J. H. B. Nihjof, *Power dependence of dispersion-managed solitons for anomalous, zero and normal dispersion*, Opt. Letters, vol. 23, pp. 900-902, 1998.

[22] G. Bosco, A. Carena, V. Curri, R. Gaudino. P. Poggiolini, and S. Benedetto, *Suppression of spurious tones induced by the split-step method in fiber systems simulation*, IEEE Photon. Technol. Letters, vol. 12, pp. 489-491, 2000.

[23] D. Breuer, *Untersuchungen zu optischen Übertragungssystemen bei 10 Gbit/s und 40 Gbit/s im verlegten Glasfasernetz*, Ph.D. Thesis, Technische Universität Berlin, Germany, 1999.

[24] J.-X. Cai, M. I. Hayee, M. Nissov, M. A. Mills, A. N. Pilipetskii, S. G. Evangelides, N. Ramanujam, C. R. Davidson, R. Menges, P. C. Corbett, D. Sutton, G. Lenner, C. Rivers, and N. S. Bergano, *1.12 Tb/s transmission over trans-atlantic distance (6,200 km) using fifty six 20 Gb/s channels*, European Conf. Opt. Commun., Munich, Germany, paper PD1.6, 2000.

[25] J.-X. Cai, M. Nissov, A. N. Pilipetskii, A. J. Lucero, C. R. Davidson, D. Foursa, H. Kidorf, M. A. Mills, R. Menges, P. C. Corbett, D. Sutton, and N. S. Bergano, *2.4 Tb/s (120x20 Gb/s) transmission over transoceanic distance using optimum FEC overhead and 48% spectral efficiency*, Opt. Fiber Commun. Conf., Anaheim, CA, paper PD20, 2001.

[26] G. M. Carter, J. M. Jacob, C. R. Menyuk, E. A. Golovchenko and A. N. Pilipetskii, *Timing-jitter reduction for a dispersion-managed soliton system: experimental evidence*, Opt. Letters, vol. 22, pp. 513-515, 1997.

[27] S. Chakravarty, M. J. Ablowitz, J. R. Sauer, and R. B. Jenkins, *Multisoliton interactions and wavelength-division multiplexing*, Opt. Letters, vol. 20, pp. 136-138, 1995.

[28] B. Chan, and J. Conradi, *On the non-Gaussian noise in Erbium-doped fiber amplifiers*, J. Lightwave Technol., vol. 15, pp. 680-687, 1997.

[29] A. Chraplyvy, *Limitations on lightwave communications imposed by optical-fiber nonlinearities*, J. Lightwave Technol., vol. 8, pp. 1548-1557, 1990.

[30] C. B. Clausen, A. Mecozzi, and M. Shtaif, *Nonlinear intra-channel effects: system impairments and their remedy*, European Conf. Opt. Commun., Munich, Germany, vol. 3, pp. 33-34, 2000.

[31] R. E. Collin, *Foundations for microwave engineering*, 2nd edition, McGraw-Hill, New York, pp. 770-772, 1992.

[32] C. R. Davidson, C. J. Chen, M. Nissov, A. Pilipetskii, N. Ramanujam, H. D. Kidorf, B. Pederson, M. A. Mills, C. Lin, M. I. Hayee, J. X. Cai, A. B. Puc, P. C. Corbett, R. Menges, H. Li, A. Elyamani, C. Rivers, and N. S. Bergano, *1800 Gb/s transmission of one hundred and eighty 10 Gb/s WDM channels over 7000 km using the full EDFA C-band*, Opt. Fiber Commun. Conf., Baltimore, MD, paper PD25, 2000.

[33] D. Derrickson, *Fiber optic test and measurement*, Prentice Hall, Upper Saddle River, p. 313, 1998.

[34] D. Derrickson, *Fiber optic test and measurement*, Prentice Hall, Upper Saddle River, pp. 542-546, 1998.

[35] E. Desurvire, *Erbium-doped fiber amplifiers, principles and applications*, John-Wiley & Sons, New York, 1994.

[36] E. Desurvire, *Erbium-doped fiber amplifiers, principles and applications*, John-Wiley & Sons, New York, pp. 10-22, 1994.

[37] J. F. L. Devaney, W. Forysiak, A. M. Niculae, and N. J. Doran, *Soliton collisions in dispersion-managed wavelength-division-multiplexed systems*, Opt. Letters, vol. 22, pp. 1695-1697, 1997.

[38] N. J. Doran, *Dispersion managed soliton systems*, European Conf. Opt. Commun., Madrid, Spain, pp. 97-99, 1998.

[39] G. Einarsson, and M. Sundelin, *Performance analysis of optical receivers by Gaussian approximation*, J. Opt. Commun., vol. 16, pp. 227-232, 1995.

[40] R. J. Essiambre, B. Mikkelsen, and G. Raybon, *Intra-channel cross-phase modulation and four-wave mixing in high-speed TDM systems*, Electron. Letters, vol. 35, pp. 1576-1578, 1999.

[41] S. G. Evangelides, and J. P. Gordon, *Energy transfer and frequency shifts from three soliton collisions in a multiplexed transmission line with periodic amplification*, J. Lightwave Technol., vol. 14, pp. 1639-1643, 1996.

[42] S. G. Evangelides, *Cross phase modulation resonances in WDM systems*, Opt. Fiber Commun. Conf., San Diego, CA, paper ThQ1, 1999.

[43] See website http://www.fftw.org.

[44] See for instance websites http://www.corningfiber.com, http://www.lucent.com, http://www.furukawa.jp

[45] D. J. Foshini, and C. D. Poole, *Statistical theory of polarization dispersion in single-mode fibers*, J. Lightwave Technol., vol. 9, pp.1439-1456, 1991.

[46] M. Frigo, and S. G. Johnson, *FFTW: an adaptive software architecture for the FFT*, ICASSP vol. 3, pp. 1381-1384, 1998.

[47] K. Fukuchi, M. Kakui, A. Sasaki, T. Ito, Y. Inada, T. Tsusaki, T. Shitomi, K. Fujii, S. Shikii, H. Sugahara, and A. Hasegawa, *1.1-Tb/s (55x20-Gb/s) dense WDM soliton transmission over 3,020-km widely-dispersion-managed transmission line employing 1.55/1.58-μm hybrid repeaters*, European Conf. Opt. Commun., Nice, France, paper PD2-1, 1999.

[48] N. Gisin, J.P. Von der Weid, and J.P. Pellaux, *Polarization mode dispersion of short and long single-mode fibers*, J. Lightwave Technol., vol. 9, pp. 821-827, 1991.

[49] A. H. Gnauck, S. K. Korotky, J. Veselka, J. Nagal, C. T. Kemmener, W. J. Mindford, and D. T. Moser, *Dispersion penalty reduction using an optical modulator with adjustable chirp*, IEEE Photon. Technol. Letters, vol. 3, pp. 916–918, 1991.

[50] E. A. Golovchenko, N. S. Bergano, C. R. Davidson, and A. N. Pilipetskii, *Modeling versus experiments of 16x10Gbit/s WDM chirped RZ pulse transmission over 7,500 km*, Opt. Fiber Commun. Conf., San Diego, CA, paper ThQ3, 1999.

[51] E. A. Golovchenko, A. N. Pilipetskii, and N. S. Bergano, *Transmission properties of chirped return-to-zero pulses and nonlinear intersymbol interference in 10 Gb/s WDM transmission*, Opt. Fiber Commun. Conf., Baltimore, MD, paper FC3, 2000.

[52] J. P. Gordon, *Interaction forces among solitons in optical fibers*, Opt. Letters, vol. 8, pp. 596-598, 1983.

[53] J. P. Gordon, and H. A. Haus, *Random walk of coherently amplified solitons in optical fiber transmission*, Opt. Letters, vol. 11, pp. 665–667, 1986.

[54] J. Gowar, *Optical communication systems*, Prentice Hall, New York, pp. 71-80, 1984.

[55] J. Gowar, *Optical communication systems*, Prentice Hall, New York, pp. 353-402, 1984.

[56] J. Gowar, *Optical communication systems*, Prentice Hall, New York, pp. 404-406, 1984.

[57] R. A. Griffin, R. G. Walker, R. I. Johnstone, R. Harris, N. M. B. Perney, and N. D. Whitbread, *Integrated 10 Gb/s chirped return-to-zero transmitter using GaAs/AlGaAs modulators*, Opt. Fiber Commun. Conf., Anaheim, CA, paper PD15, 2001.

[58] V. S. Grigoryan, T. Yu, E. A. Golovchenko, C. R. Menyuk, and A. N. Pilipetskii, *Dispersion-managed soliton dynamics*, Opt. Letters, vol. 22, pp. 1609-1611, 1997.

[59] V. S. Grigoryan, and A. Richter, *Reduced model for simulation of collision-induced timing jitter in massive RZ WDM systems*, OSA Annual Meeting, Baltimore, MD, 1998.

[60] V. S. Grigoryan, C. R. Menyuk, and R.-M. Mu, *Calculation of timing and amplitude jitter in dispersion-managed optical fiber communications using linearization*, J. Lightwave Technol., vol. 17, pp. 1347-1356, 1999.

[61] V. S. Grigoryan, and A. Richter, *Efficient approach for modeling collision-induced timing jitter in WDM return-to-zero dispersion-managed systems*, J. Lightwave Technol., vol. 18, pp. 1148-1154, 2000.

[62] V. S. Grigoryan, G. M. Carter, and C. R. Menyuk, *Tolerance of dispersion-managed soliton transmission to the shape of the input pulses*, IEEE Photon. Technol. Letters, vol. 12, pp 1165-1167, 2000.

[63] D. Le Guen, S. Del Burgo, M. L. Moulinard, D. Grot, M. Henry, F. Favre, and T. Georges, *Narrow band 1.02 Tbit/s (51x20 Gbit/s) soliton DWDM transmission over 1000 km of standard fiber with 100 km amplifier spans*, Opt. Fiber Commun. Conf., San Diego, CA, paper PD4, 1999.

[64] A. Hasegawa, and F. Tapper, *Transmission of stationary nonlinear optical pulses in dispersive dielectric fibers. I. anomalous dispersion*, Applied Physics Letters, vol. 23, pp. 142-144, 1973.

[65] A. Hasegawa, and Y. Kodama, *Guiding-center soliton in optical fibers*, Opt. Letters, vol. 15, pp. 1443-1445, 1990.

[66] A. Hasegawa, and Y. Kodama, *Guiding-center soliton in fibers with periodically varying dispersion*, Opt. Letters, vol. 16, pp. 1385-1387, 1991.

[67] A. Hasegawa, and Y. Kodama, *Guiding-center soliton*, Phys. Rev. Letters, vol. 66, pp. 161-164, 1991.

[68] A. Hasegawa, and Y. Kodama, *Solitons in optical communications*, Clarendon Press, Oxford, p. 39, 1995.

[69] A. Hasegawa, and Y. Kodama, *Solitons in optical communications*, Clarendon Press, Oxford, pp. 45-66, 1995.

[70] A. Hasegawa, and Y. Kodama, *Solitons in optical communications*, Clarendon Press, Oxford, pp. 67-90, 1995.

[71] A. Hasegawa, and Y. Kodama, *Solitons in optical communications*, Clarendon Press, Oxford, pp. 151-164, 1995.

[72] J. I. Hashimoto, Y. Nakano, and K. Tada, *Influence of facet reflection on the performance of a DFB laser integrated with an optical amplifier/modulator*, J. Quantum Electron., vol. 28, pp. 594–603, 1992.

[73] H. A. Haus, *Quantum noise in solitonlike repeater systems*, J. Opt. Soc. Am. B, vol. 8, pp. 1122-1126, 1991.

[74] A. Hirano, Y. Miyamoto, K. Yonenaga, A. Sano, and H. Toba, *40 Gbit/s L-band transmission experiment using SPM-tolerant carrier-suppressed RZ format*, Electron. Letter, vol. 35, pp. 2213-2215, 1999.

[75] T. Hirooka and A. Hasegawa, *Chirped soliton interaction in strongly dispersion-managed wavelength-division-multiplexing system*, Opt. Lett., vol. 23, pp. 768-770, 1998.

[76] T. Hirooka, T. Nakada, and A. Hasegawa, *Feasibility of densely dispersion managed soliton transmission at 160 Gb/s*, IEEE Transact. Photon. Technol. Letters, vol. 12, pp. 633-635, 2000.

[77] R. Holzlöhner, C. R. Menyuk, V. S. Grigoryan, and W. L. Kath, *Accurate calculation of eye diagrams and error rates in long-haul transmission systems*, Opt. Fiber Commun. Conf., Anaheim, CA, paper MF3, 2001.

[78] M. Horiguchi, and H. Osanai, *Spectral losses of low-OH-content optical fibers*, Electron. Letters vol. 12, pp. 310-312, 1976.

[79] E. Iannone, F. Matera, A. Mecozzi, and M. Settembre, *Nonlinear optical communication networks*, John Wiley & Sons, New York, pp. 56-63, pp. 331-345, 1998.

[80] E. Iannone, F. Matera, A. Mecozzi, and M. Settembre, *Nonlinear optical communication networks*, John Wiley & Sons, New York, pp. 72-73, 1998.

[81] E. Iannone, F. Matera, A. Mecozzi, and M. Settembre, *Nonlinear optical communication networks*, John Wiley & Sons, New York, pp. 114-118, 1998.

[82] E. Iannone, F. Matera, A. Mecozzi, and M. Settembre, *Nonlinear optical communication networks*, John Wiley & Sons, New York, pp. 155-159, 1998.

[83] E. Iannone, F. Matera, A. Mecozzi, and M. Settembre, *Nonlinear optical communication networks*, John Wiley & Sons, New York, pp. 428–430, 1998.

[84] K. Inoue, *Four-wave mixing in an optical fiber in the zero-dispersion wavelength region*, J. Lightwave Technol., vol. 10, pp. 1553-1561, 1992.

[85] T. Inoue, H. Sugahara, A. Maruta, and Y. Kodama, *Interactions between dispersion managed solitons in optical-time-division-multiplexed system*, IEEE Photon. Technol. Letters, vol. 12, pp 299-301, 2000.

[86] G. Jacobsen, K. Bertilson, and Z. Xiaopin, *WDM transmission system performance: influence of non-Gaussian detected ASE noise and periodic DEMUX characteristic*, J. Lightwave Technol., vol. 16, pp. 1804-1812, 1998.

[87] G. Jacobsen, and P. Wildhagen, *A general and rigorous WDM Rx model targeting 10-40 Gbit/s channel bit-rates*, J. Lightwave Technol., vol. 19, 2001.

[88] R. B. Jenkins, J. R. Sauer, S. Chakravarty, and M. J. Ablowitz, *Data-dependent timing jitter in wavelength-division-multiplexing soliton systems*, Opt. Letters, vol. 20, pp. 1964-1966, 1995.

[89] I.P. Kaminow and T. L. Koch (ed.), *Optical Fiber Telecommunications, Volume IIIB*, Academic Press, San Diego, p. 89, 1997.

[90] D. J. Kaup, B. A. Malomed, and J. Yang, *Interchannel pulse collision in a wavelength-division-multiplexed system with strong dispersion management*, Opt. Letters, vol. 23, pp. 1600-1602, 1998.

[91] G. Keiser, *Optical fiber communications*, 3rd edition, McGraw-Hill, Boston, Chapter 3.1, 2000.

[92] G. Keiser, *Optical fiber communications*, 3rd edition, McGraw-Hill, Boston, pp. 108-113, 2000.

[93] G. Keiser, *Optical fiber communications*, 3rd edition, McGraw-Hill, Boston, pp. 437-440, 2000.

[94] Y. Kobayashi, K. Kinjo, K. Ishida, T. Sugihara, S. Kajiya, N. Suzuki, and K. Shimizu, *A comparison among pure-RZ, CS-RZ and SSB-RZ format, in 1 Tbit/s (50x20 Gbit/s, 0.4 nm spacing) WDM transmission over 4,000 km*, European Conf. Opt. Commun., Munich, Germany, paper PD1.7, 2000.

[95] Y. Kodama, and A. Hasegawa, *Effects of initial overlap on the propagation of optical solitons at different wavelengths*, Opt. Letters, vol. 16, pp. 208-209, 1991.

[96] F. Koyama, K. Iga, *Frequency chirping in external modulators*, J. Lightwave Technol, vol.6, no. 1, 1988.

[97] H. Kubota, and M. Nakazawa, J. Quantum Electron., vol. 26, p. 692, 1990.

[98] J. N. Kutz, and P. K. A. Wai, *Gordon-Haus timing jitter reduction in dispersion-managed soliton communications*, IEEE Photon. Technol. Letters, vol. 10, pp. 702-704, 1998.

[99] E. A. Lee, D. G. Messerschmitt, *Digital communications*, 2nd edition, Kluwer Academic Publisher, Boston, pp. 53-55, 1994.

[100] F. Liu, C. Peucheret, X. Theng, R. J. S. Pedersen, and P. Jeppesen, *A novel chirped return-to-zero transmitter and transmission experiments*, European Conf. Opt. Commun., Munich, Germany, vol. 3, pp. 113-114, 2000.

[101] A. Lowery, O. Lenzmann, I. Koltchanov, R. Moosburger, R. Freund, A. Richter, S. Georgi, D. Breuer, and H. Hamster, *Multiple signal representation simulation of photonic devices, systems, and networks*, J. Selected Topics Quantum Electron., vol. 6, pp. 282-296, 2000.

[102] P. V. Mamyshev, and N. A. Mamysheva, *Pulse-overlapped dispersion-managed data transmission and intrachannel four-wave mixing*, Opt. Letters, vol. 24, pp. 1454-1456, 1999.

[103] D. Marcuse, *Theory of dielectric optical waveguides*, 2nd edition, Academic Press, London, pp. 336-341, 1991.

[104] D. Marcuse, *Derivation of analytical expressions for the bit-error probability in lightwave systems with optical amplifiers*, J. Lightwave Technol., vol. 8, pp. 1816-1823, 1990.

[105] D. Marcuse, *Calculation of bit-error probability for a lightwave system with optical amplifiers*, J. Lightwave Technol., vol. 9, pp. 505-513, 1991.

[106] D. Marcuse, and C. R. Menyuk, *Simulation of single-channel optical systems at 100 Gb/s*, J. Lightwave Technol., vol. 17, pp. 564-569, 1999.

[107] J. Martensson, M. Westlund, and A. Berntson, *Intra-channel pulse interactions in 40 Gbit/s dispersion-managed RZ transmission*, Electron. Letters, vol. 36, pp. 244-246, 2000.

[108] F. Matera, and M. Settembre, *Role of Q-factor and of timing jitter in the performance evaluation of optically amplified transmission systems*, J. Selected Topics in Quantum Electron., vol. 6, pp. 308-316, 2000.

[109] R. J. Mears, L. Reekie, I. M. Jauncey, and D. N. Payne, *Low noise Erbium doped fiber amplifier operating at 1.54*μ*m*, Electron. Letters, vol. 23, pp. 1026-1028, 1987.

[110] A. Mecozzi, J. D. Moores, H. A. Haus, and Y. Lai, *Generation of asymptotically stable optical solitons and suppression of the Gordon-Haus effect*, Opt. Letters, vol. 16, pp. 1841-1843, 1991.

[111] A. Mecozzi, *Timing jitter in wavelength-division-multiplexed filtered soliton transmission*, J. Opt. Soc. Am. B, vol. 15, pp. 152-161, 1998.

[112] A. Mecozzi, C. B. Clausen, and M. Shtaif, *Analysis of intrachannel nonlinear effects in highly dispersed optical pulse transmission*, IEEE Photon. Technol. Letters, vol. 12, pp 392-394, 2000.

[113] G. Mohs, C. Fürst, H. Geiger, and G. Fischer, *Advantages of nonlinear RZ over NRZ on 10 Gb/s single-span links*, Opt. Fiber Commun. Conf., Baltimore, MD, paper FC2, 2000.

[114] L. F. Mollenauer, R. H. Stolen, and J. P. Gordon, *Experimental observation of picosecond pulse narrowing and solitons in optical fibers*, Phys. Rev. Letters, vol. 45, pp. 1095-1098, 1980.

[115] L. F. Mollenauer, and K. Smith, *Demonstration of soliton transmission over more than 4,000 km in fiber with loss periodically compensated by Raman gain*, Opt. Letters, vol. 13, pp. 675-677, 1988.

[116] L. F. Mollenauer, M. J. Neubelt, S. G. Evangelides, J. P. Gordon, J. R. Simpson, and L. G. Cohen, *Experimental study of soliton transmission over more than 10,000 km in dispersion shifted fiber*, Opt. Letters, vol. 15, pp. 1203-1205, 1990.

[117] L. F. Mollenauer, S. G. Evangelides, and H. A. Haus*, Long-distance soliton propagation using lumped amplifiers and dispersion shifted fibers,* J. Lightwave Technol., vol. 9, pp. 194-196, 1991.

[118] L. F. Mollenauer, S. G. Evangelides, and J. P. Gordon, *Wavelength division multiplexing with solitons in ultra-long distance transmission using lumped amplifiers*, J. Lightwave Technol., vol. 9, pp. 362-367, 1991.

[119] L. F. Mollenauer, E. Lichtman, M. J. Neubelt, and G. T. Harvey, *Demonstration, using sliding-frequency guiding filters, of error-free soliton transmission over more than 20 Mm 10 Gbit/s, single channel, and over more than 13 Mm at 20 Gbit/s in a two-channel WDM*, Electron. Letters, vol. 29, pp. 910-912, 1993.

[120] L. F. Mollenauer, P. V. Mamyshev, and M. J. Neubelt, *Demonstration of soliton WDM transmission at 6 and 7x10 Gbit/s, error free over transoceanic distances*, Electron. Letters, vol. 32, pp. 471-473, 1996.

[121] M. Moniere, and L. Jeunhomme, *Polarization mode coupling in long single-mode fibers*, Opt. and Quantum Electron., vol. 12, pp. 449-461, 1980.

[122] I. Morita, K. Tanaka, N. Edagawa, and M. Suzuki, *40 Gb/s single-channel soliton transmission over transoceanic distances by reducing Gordon-Haus timing jitter and soliton-soliton interaction*, J. Lightwave Technol., vol. 18, pp. 2506-2511, 1999.

[123] M. Murakami, T. Matsuda, and T. Imai, *Quarter terabit (25x10 Gb/s) over 9288 km WDM transmission experiment using nonlinear supported RZ pulse in higher order fiber dispersion managed line*, European Conf. Opt. Commun., Madrid, Spain, PDL session, pp. 79-81, 1998.

[124] R.-M. Mu, T. Yu, V. S. Grigoryan, and C. R. Menyuk, *Convergence of the CRZ and DMS formats in WDM systems using dispersion management*, Opt. Fiber Commun. Conf., Baltimore, MD, paper FC1, 2000.

[125] M. Nakazawa, Y. Kimura, and K. Suzuki, *Soliton amplification and transmission with Er3+-doped fiber repeater pumped by GaInAsP laser diode*, Electron. Letters, vol. 25, pp. 199-200, 1989.

[126] M. Nakazawa, K. Yamada, H. Kubota, and E. Suzuki, *10 Gbit/s soliton data transmission over one million of kilometers*, Electron. Letters, vol. 27, pp. 1270-1272, 1991.

[127] L. E. Nelson, A. H. Gnauck, R. M. Jopson, and A. R. Chraplyvy, *Cross phase modulation resonances in wavelength division multiplexed lightwave transmission*, European Conf. Opt. Commun., Madrid, Spain, vol. 1, pp. 309-310,1998.

[128] A. M. Niculae, W. Forysiak, A. J. Gloag, J. H. B. Nijhof, and N. J. Doran, *Soliton collisions with wavelength-division multiplexed systems with strong dispersion management*, Opt. Lett., vol. 23, pp. 1354-1356, 1998.

[129] A. V. Oppenheim, R. W. Schafer, *Discrete-time signal processing*, Prentice Hall, Englewood Cliffs, pp. 587-622, 1989.

[130] A. N. Pinto, G. P. Agrawal, and J. F. Da Rocha, *Effect of soliton interaction on timing jitter in communication systems*, J. Lightwave Technol., vol. 16, pp. 515-519, 1998.

[131] A. Richter, and V. S. Grigoryan, *Efficient approach to estimate collision-induced timing jitter in dispersion-managed WDM RZ systems*, Opt. Fiber Commun. Conf., San Diego, CA, paper WM33, 1999.

[132] A. Richter, *Efficient modeling of pulse timing jitter in repeated WDM RZ systems*, Workshop der ITG Fachgruppe 5.3.1, Munich, Germany, 1999.

[133] A. Richter, and V. S. Grigoryan, *Efficient modeling of timing jitter due to cross phase modulation in massive WDM systems with chirped RZ modulation format*, Conf. Lasers Electro-Optics, San Francisco, CA, paper CTuG3, 2000.

[134] A. Richter, A. Lowery, and P. Wildhagen, *Estimation of BER in the presence of timing jitter in WDM transmission systems using RZ modulation formats*, Nat. Fiber Optic Engineers Conf., Baltimore, MD, paper C5-2, 2001.

[135] A. Sano, Y. Miyamoto, K. Yonenaga, and H. Toba, *20 Gbit/s chirped return-to-zero transmitter with simplified configuration using electro-absorption modulator*, Electron. Letters, vol. 36, pp. 1858-1860, 2000.

[136] N. J. Smith, N. J. Doran, K. J. Blow, and W. J. Firth, *Gordon-Haus jitter suppression using a single phase modulator*, Electron. Letters, vol. 30, pp. 987-988, 1994.

[137] N. J. Smith, F. M. Knox, N. J. Doran, K. J. Blow, and I. Bennion, *Enhanced power solitons in optical fibres with periodic dispersion management*, Electron. Letters, vol. 32, pp. 54-55, 1996.

[138] N. J. Smith, N. J. Doran, F. M. Knox, and W. Forysiak, *Energy-scaling characteristics of solitons in strongly dispersion-managed fiber*, Opt. Letters, vol. 21, pp. 1981-1983, 1996.

[139] N. J. Smith, N. J. Doran, W. Forysiak, and F. M. Knox, *Soliton transmission using periodic dispersion compensation*, J. Lightwave Technol., vol. 15, pp. 1808-1822, 1997.

[140] H. Stark, and J. W. Woods, *Probability, random processes, and estimation theory for engineers*, 2nd edition, Prentice Hall, pp. 60-61, 1994.

[141] H. Stark, and J. W. Woods, *Probability, random processes, and estimation theory for engineers*, 2nd edition, Prentice Hall, Englewood Cliffs, pp. 160-161, 1994.

[142] H. Stark, and J. W. Woods, *Probability, random processes, and estimation theory for engineers*, 2nd edition, Prentice Hall, Englewood Cliffs, pp. 213-218, 1994.

[143] H. Sugahara, H. Kato, and Y. Kodama, *Maximum reductions of collision induced frequency shift in soliton-WDM systems with dispersion compensation*, Electron. Lett., vol. 33, pp. 1065-1066, 1997.

[144] H. Sugahara, H. Kato, T. Inoue, A. Maruta, and Y. Kodama, *Optimal dispersion management for a wavelength-division-multiplexed optical soliton transmission system*, J. Lightwave Technol., vol. 17, pp. 1547-1559, 1999.

[145] H. Sugahara, A. Maruta, and J. Kodama, *Optimal allocation of amplifiers in a dispersion-managed line for a wavelength-division-multiplexed soliton transmission system*, Opt. Lett., vol. 24, pp. 145-147, 1999.

[146] M. Suzuki, I Morita, N. Edawaga, S. Yamamoto, H. Taga, and S. Akiba, *Reduction of Gordon-Haus timing jitter reduction by periodic dispersion compensation in soliton transmission*, Electron. Letters, vol. 31, pp. 2027-2029, 1995.

[147] T. Tanaka, D. Shimojoh, T. Naito, H. Nakamoto, I. Yokota, T. Ueki, A. Sugiyama, and M. Suyama, *2.1-Tbit/s WDM transmission over 7,221 km with 80-km repeater spacing*, European Conf. Opt. Commun., Munich, Germany, paper PD1.8, 2000.

[148] P. R. Trischitta, et al., *The TAT-12/13 cable network*, IEEE Commun. Magazin, February 1996.

[149] T. Tsuritani, N. Takeda, K. Imai, K. Tanaka, A. Agata, I. Morita, Y. Yamauchi, N. Edagawa, and M. Suzuki, *1 Tbit/s (100x10.7 -Gbit/s) transoceanic transmission using 30nm-wide broadband optical repeaters with Aeff-enlarged positive dispersion fiber and slope-compensating DCF*, European Conf. Opt. Commun., Nice, France, paper PD2-8, 1999.

[150] S. K. Turitsyn, V. K. Mezentsev, and E. G. Shapiro, *Dispersion-managed solitons and optimization of the dispersion management*, Optic. Fiber Technol., vol. 4, pp. 384-452, 1998.

[151] S. K. Turitsyn, M. P. Fedoruk, N. J. Doran, and W. Forysiak, *Optical soliton transmission in fiber lines with short-scale dispersion management*, European Conf. Opt. Commun., Nice, France, pp. I-382-383, 1999.

[152] S. K. Turitsyn, M. F. Fedoruk, E. G. Shapiro, V. K. Mezentsev, and E. G. Turitsyna, *Novel approaches to numerical modeling of periodic dispersion-managed fiber communication systems*, J. Selected Topics in Quantum Electron., vol. 6, pp. 263-275, 2000.

[153] See website http://www.vpisystems.com.

[154] VPIsystems, *VPIcomponentMaker Fiber Amplifier User's Manual*, pp. 24-30, 2001.

[155] VPIsystems, *Photonic Modules Reference Manual*, 2001.

[156] Y. J. Wen, J. Chen, and X. L. Yang, *The effects of carrier phase noise on long-distance soliton transmission system*, IEEE Photon. Technol. Letters, vol. 10, pp. 1277-1279, 1998.

[157] P. T. Wildhagen, *Implementation and evaluation of numerical techniques for BER estimation in direct detection fiber optical communication systems*, Diplomarbeit, Technische Universität Berlin, Germany, 1999.

[158] M. Yamada, A. Mori, K. Kobayashi, H. Ono, T. Kanamori, K. Oikawa, Y. Nishida, and Y. Ohishi, *Gain-flattened Tellurite-based EDFA with flat amplification bandwidth of 76 nm*, Opt. Fiber Commun. Conf., San Jose, CA, paper PD7, 1998.

[159] T. S. Yang, and W. L. Kath, *Analysis of enhanced-power solitons in dispersion-managed optical fibers*, Opt. Letters, vol. 22, pp. 985-987, 1997.

[160] T. S. Yang, W. L. Kath, and S. K. Turitsyn, *Optimal dispersion maps for wavelength-division multiplexed soliton transmission*, Opt. Letters, vol. 23, pp. 597-599, 1998.

[161] T. S. Yang, W. L. Kath, and S. G. Evangelides, *Optimal prechirping for dispersion-managed transmission of return-to-zero pulses*, Opt. Fiber Commun. Conf., San Diego, CA, paper ThQ4, 1999.

[162] T. Yu, E. A. Golovchenko, A.N. Pilipetskii, and C. R. Menyuk, *Dispersion-managed soliton interactions in optical fibers*, Opt. Letters, vol. 22, pp. 793-795, 1997.

[163] T. Yu, R.-M. Mu, V. S. Grigoryan, and C. R. Menyuk, *Energy enhancement of dispersion-managed solitons in optical fiber transmission systems with lumped amplifiers*, IEEE Photon. Technol. Letters, vol. 11, pp. 75-77, 1999.

[164] V. E. Zahkarov, and A. B. Shabat, *Exact theory of two-dimensional self-focusing and one-dimensional self modulation of waves in nonlinear media*, Sov. Phys. JETP, vol. 34, pp 62-69, 1972.

Appendix A

List of Acronyms

ACF	AutoCorrelation Function
ANTJ	ASE-Noise induced Timing Jitter
ASE	Amplified Spontaneous Emission
BER	Bit Error Rate
CITJ	Collision-Induced Timing Jitter
CRZ	Chirped Return-to-Zero
DCF	Dispersion Compensating Fiber
DD	Direct Detection
DMS	Dispersion-Managed Soliton
DNA	Deterministic Noise Approximation
DSF	Dispersion Shifted Fiber
EAM	Electro-Absorption Modulator
ECA	Elastic Collision Approximation
EDFA	Erbium Doped Fiber Amplifier
EOP	Eye Opening Penalty
FEC	Forward Error Correction
FFT	Fast Fourier Transform
FWHM	Full Width Half Maximum
FWM	Four Wave Mixing
GA	Gaussian Approximation
GNLS	Generalized Nonlinear Schrödinger Equation

GVD	Group Velocity Dispersion
HODM	Higher Order Dispersion Management
I-FWM	Intrachannel Four-Wave Mixing
IM	Intensity Modulation
IPP	Initial Pulse Positioning
ISI	InterSymbol Interferences
I-XPM	Intrachannel Cross-Phase Modulation
LCF	Large Core Fiber
MC	Monte Carlo
MZM	Mach-Zehnder Modulator
NF	Noise Figure
NRZ	Non Return-to-Zero
NZDSF	Non-Zero Dispersion Shifted Fiber
OSNR	Optical Signal-to-Noise Ratio
PDF	Probability Density Function
PSD	Power Spectral Density
RZ	Return-to-Zero
SPM	Self-Phase Modulation
SSMF	Standard Single Mode Fiber
WDM	Wavelength Division Multiplexing
XPM	Cross-Phase Modulation

Appendix B

List of Symbols

$A(z, t)$	complex field envelope, slowly varying field amplitude
A_{eff}	effective core area
B	bandwidth
B_o	optical bandwidth
B_e	electrical bandwidth
c	speed of light, in a vacuum $c_0 = 2.99792458 \times 10^8 [m/s]$
D	dispersion coefficient
$\vec{E}$	electric field vector
$F(x, y)$	transversal field distribution
f_t, f_a	probability density function with respect to time, amplitude
$g(z)$	A: net gain, combines fiber loss and amplifier gain B: gain per distance inside an EDFA
G	total amplifier gain
h	Planck's constant, $h = 6,62607 \times 10^{-34} [Ws^2]$
$I(t)$	field intensity
k_B	Boltzmann's constant, $k_B = 1.38054 \times 10^{-23} [J/K]$
L_A	spacing between two lumped amplifiers
L_{Amp}	doped fiber length in optical amplifier
L_c	collision length of two colliding pulses

$L_{Collapse}$	collapse length of two interacting solitons
L_D	dispersion length
L_{eff}	effective fiber length
L_{NL}	nonlinear length
L_S	soliton period for initial shape recovery
L_w	walk-off length
N	A: number of samples B: number of trials
$N(z, t)$	random noise process
$n(\omega)$	refractive index
n_0	linear refractive index
n_2	nonlinear refractive index
N_s	soliton order
n_{sp}	spontaneous emission factor, population inversion factor
$\vec{P}$	electric polarization vector
P_0	initial, peak power
P_{ASE}	ASE-noise power
q	electron charge, $q = 1.60218 \times 10^{-19}[C]$
$q(z, t)$	normalized field amplitude
S	slope of dispersion coefficient D
t, T	time, eventually normalized, retarded; central time of pulse
T_0	pulse duration: half-width at the 1/e-intensity
T_F	pulse duration: full-width at half the max intensity (FWHM)
U	pulse energy
v_g	group velocity
z, Z	coordinate in propagation direction, could be normalized
α	fiber attenuation
$\beta(\omega)$	mode propagation constant

β_1	inverse of group velocity v_g
β_2	group velocity dispersion (GVD), chromatic dispersion
β_3	slope of GVD, 2nd order GVD
γ	nonlinear coefficient
η	FWM efficiency
λ	wavelength
ρ_m	effective mode radius of the fiber
σ_a^2	variance of pulse energy
σ_t^2	variance of pulse position
μ	permeability, in a vacuum $\mu_0 = 4\pi \times 10^{-7} [N/A^2]$
ϕ_0	initial phase
$\Delta\phi$	phase increment
ω	circular frequency
Ω	central frequency of pulse
ΔT	A: pulse broadening B: pulse separation
Δz	step size in split-step Fourier method
$\Delta\beta$	phase mismatch

Acknowledgements

I would like to take this opportunity to thank several people for the support that they provided me during the last four years in getting this work done.

I am especially grateful to Dr. Vladimir Grigoryan, as he introduced me to the foundations of pulse dynamics in nonlinear fiber propagation. This work was inspired and greatly influenced by Dr. Vladimir Grigoryan. He derived the mathematical foundations for the developed semi-analytical algorithms, which calculate timing jitter due to optical amplifier noise and interchannel cross-phase modulation. I regard Dr. Vladimir Grigoryan as both, a good teacher and valuable friend. I am also very grateful to Prof. Curtis Menyuk, who invited me to stay with his research group at the University of Maryland, Baltimore County for three months in 1998. During this time, I had many fruitful discussions with members of his team. I would especially like to mention here Dr. Edem Ibragimov and Dr. Tao Yu, whom I learned to appreciate as friends as well.

I am also very grateful to my fellow colleagues at VPIsystems, who allowed me the support and necessary freedom to achieve this work. Dr. Kay Iversen and Dr. Rudolf Moosburger provided me with creative freedom and also gave me their support as supervising colleagues. I am also grateful for the knowledge and understanding regarding physics and modeling techniques of fiber-optic communication systems that I gained in discussions with Dr. Arthur Lowery, Dr. Igor Koltchanov, Dr. Rudolf Moosburger, Ronald Freund, and Dr. Dirk Breuer.

I am grateful to Prof. Klaus Petermann from the Technische Universität Berlin for supporting me and allowing me to write this thesis as an external student of his research team.

I would also like to thank Marcia Bascombe, for introducing to me the deep secrets of Adobe® FrameMaker®, and giving me valuable comments and ideas regarding the layout. I thank her and Dr. Peter Moar for proof-reading the text.

Finally, I would like to thank my wife, Synke and my sons Tim and Jan for their patience and tender support.

André Richter
Berlin, 10. 10. 2001